Joana Tavares Macedo

Licenciatura em Bioquímica

Functional and structural studies of a mini-ferritin protein

Dissertação para obtenção do Grau de Mestre em Bioquímica

Orientador: Prof. Doutor Pedro Tavares,
Professor Auxiliar, FCT-UNL
Co-orientador: Prof. Doutora Alice Pereira,
Professora Auxiliar, FCT-UNL
Co-orientador: Prof. Doutora Susana Andrade,
Professora Auxiliar, Universität Freiburg

Júri:

Presidente: Prof. Doutor José Ricardo Ramos Franco Tavares
Arguente: Prof. Doutora Teresa Sacadura Santos Silva
Vogal: Prof. Doutor Pedro António de Brito Tavares

FACULDADE DE CIÊNCIAS E TECNOLOGIA
UNIVERSIDADE NOVA DE LISBOA

Setembro de 2014

“Copyright”

Functional and structural studies of a mini-ferritin protein

Joana Tavares Macedo

Faculdade de Ciências e Tecnologia/Universidade Nova de Lisboa

Universidade Nova de Lisboa

Agradecimentos

Porque o conhecimento não se constrói individualmente e a vida não é só feita de ajudas e pedidos, gostaria de agradecer a todas as pessoas que me acompanharam ao longo deste percurso e que contribuíram para o seu sucesso!

Em primeiro lugar, gostaria de agradecer à Faculdade de Ciências e Tecnologia da Universidade Nova de Lisboa que proporcionou o espaço e as condições para que a minha aprendizagem fosse possível, bem como a todos os Professores que contribuíram para a mesma.

Quero agradecer aos meus orientadores, Doutor Professor Pedro Tavares, Doutora Professora Alice Pereira e Doutora Professora Susana Andrade pela excelente oportunidade que me deram. Obrigada por me terem recebido nos vossos laboratórios, pela partilha de conhecimento e por me terem proporcionado uma nova experiência que sem dúvida mudou a minha vida.

Um agradecimento muito especial ao Doutor Filipe Folgosa! Obrigada por tudo o que fizeste por mim, tanto em Portugal como na Alemanha. Obrigada por todos os conselhos, todas as gargalhadas e todas as chamadas de atenção. Sem dúvida que tinhas razão!

Um agradecimento muito especial também ao Tobias Pflüger em múltiplos aspectos Obrigada por todo o apoio dentro e fora do laboratório. Obrigada por todas as extraordinárias horas de ajuda e todos os conselhos. Mais do que tudo, obrigada por teres estado sempre presente quando precisei, pelos bons momentos e por teres contribuído para o meu gosto pela Alemanha.

Agradeço à Daniela Silva bem como à Nídia Almeida por todo a ajuda e disponibilidade demonstradas, tal como também pelos bons momentos passados no laboratório. Também quero agradecer à Doutora Cristina Cordas e a Doutora Cristina Timóteo por todos os conselhos e pelos convívios e boa disposição

Quero ainda agradecer ao Professor Doutor Oliver Einsle bem como ao seu grupo e ao grupo da Professora Doutora Susana Andrade, por me terem recebido tão bem nos seus laboratórios e por se mostrarem sempre disponíveis. Sem dúvida que tornaram esta experiência ainda mais gratificante! Julian Seidel e Anton Brausemann obrigada pela ajuda com o Coot e o Pymol. Tobias Wacker obrigada por toda a partilha de conhecimentos, conselhos e boa disposição. Professor Doutor Thorsten Friedrich obrigada pela a disponibilidade para a utilização da câmara de luvas. Dankeschön!

Um enorme agradecimento a todos os meus amigos que sempre me apoiaram e incentivaram quando foi necessário. Obrigada por estarem lá nos bons e nos maus momentos, obrigada pelos conselhos, pela paciência e por todas as alegrias. A nossa amizade não acaba aqui!

Por ultimo, resta-me um enorme e especial agradecimento à minha família, sobretudo aos meus pais e ao meu irmão. Obrigada do fundo do coração por sempre terem estado ao

meu lado e terem acredito em mim. Sem vocês nada disto teria sido possível, obrigada por tudo! E por mais que esteja geograficamente longe, nunca me vou esquecer de vocês nem do que fizeram por mim.

Abstract

DNA-binding protein from starved cells (Dps) are mini-ferritins mainly expressed in bacteria during severe environmental stress. These proteins with a highly conserved structure provide wide protection to cells and function as iron-storage proteins. Some Dps can also bind DNA and the N-terminus has been suggested to be involved in this interaction, due to its positively charged residues.

This thesis focused on the functional and structural features of recombinant Dps protein from *Pseudomonas nautica* 617 (*P. nautica*).

To investigate the iron incorporation mechanism, iron uptake assays using H_2O_2 and O_2 as co-substrate for iron oxidation were performed with Dps WT and F46G variant, using UV-Visible spectroscopy. The results showed that Phe46, located close to the ferroxidase center (FOC), does not influence the amount of iron stored. Nevertheless, this residue affectes the iron core formation when O_2 was used as co-substrate.

Structural characterization of the incorporation of Fe(II) and Cu(II) was performed with X-ray crystallography. High resolution crystal structures of Apo-Dps, Dps incubated with 12 Fe(II)/Dps (12Fe-Dps) and Dps incubated with 12 Cu(II)/Dps (12Cu-Dps) were obtained. It was possible to observe the binding of the metals to the FOCs with different coordination geometry as well as geometrically different FOCs. Additionally Fe(II) and Cu(II) atoms were assigned in a position where hydrophilic pores can be created and serve as entry routes for the metals.

For the characterization of the Dps-DNA interaction, electrophoretic mobility shift assays (EMSAs) were carried out with Dps WT and Q14E variant. The results showed that this protein can bind DNA, but the affinity for DNA significantly decreases in the presence of the negative charge in the N-terminus. In this sense, mutations in the N-terminus that may increase the affinity for DNA binding were produced by site-directed mutagenesis.

Keywords: Dps, X-ray crystallography, iron storage, DNA binding, ferroxidase center, copper binding

Resumo

DNA-binding protein from starved cells (Dps) são mini-ferritinas maioritamente expressas em bactérias sob extremas condições de stress. Estas proteínas com uma estrutura altamente conservada, fornecem protecção às células e têm a capacidade de armazenar ferro. Algumas Dps podem ainda ligar DNA, sendo que foi sugerido que o N-terminal se encontra envolvido nesta interação, devido a resíduos positivamente carregados.

Esta tese focou-se assim nas características funcionais e estruturais da Dps recombinante de *Pseudomonas nautica* 617 (*P. nautica*).

De forma a investigar o mecanismo de incorporação de ferro recorreu-se à espectroscopia de UV-Visível. Ensaios de incorporação de ferro foram efectuados com Dps WT e F46G, usando H_2O_2 e O_2 como co-substratos para a oxidação de ferro. Os resultados adquiridos mostraram que a fenilalanina 46, situada próximo do centro ferroxidático (FOC), não influencia a quantidade de ferro armazenado. No entanto, este resíduo afecta a formação do núcleo de ferro quando O_2 é usado como co-substrato.

Por outro lado, a cristalografia de raios-X foi utilizada para a caracterização estrutural da incorporação de Fe(II) e Cu(II). Estruturas cristalográficas da Apo-Dps, Dps incubada com 12 Fe(II)/Dps e Dps incubada com 12 Cu(II)/Dps foram obtidas com elevada resolução. Com estas estruturas foi possível observar, a ligação dos metais aos FOCs com diferentes geometrias de coordenação, bem como, FOCs geometricamente diferentes. Para além disso, adicionais átomos de Fe(II) e Cu(II) foram identificados numa posição onde poros hidrofílicos podem ser criados e servir como canais de entrada para os iões metálicos.

Por último, para a caracterização da interação Dps-DNA, ensaios de mobilidade eletroforética foram realizados com Dps WT e Q14E, demonstrando que esta proteína tem a capacidade de ligar DNA, mas a afinidade de ligação é significativemente reduzida com a presença de uma carga negativa no N-terminal. Assim sendo, foram produzidas mutações no N-terminal que podem aumentar a afinidade de ligação do DNA, através de mutagénese dirigida.

Palavras-chave: Dps, Cristalografia de Raios-X, armazenamento de ferro, ligação de DNA, centro de ferroxidase, ligação de cobre

Table of Contents

Figures Index

8 Appendices

Tables Index

Abbreviations, Symbols and Constants

Apo-Dps	Apoprotein Dps
APS	Ammonium persulfate
A. tumefaciens	*Agrobacterium tumefaciens*
a.u.	Asymmetric unit
bp	Base pairs
BSA	Bovine serum albumine
Bfr	Bacterioferritin
B. anthracis	*Bacillus anthracis*
B. brevis	*Bacillus brevis*
CCP4	Collaborative Computational Project Number 4
$CC_{1/2}$	Correlation coefficient between random half datasets
DIC	Differential Interference Contrast
DNA	Deoxyribonucleic acid
DMSO	Dimethyl sulfoxide
dNTPs	deoxyribonucleotides
Dps	DNA-binding protein from starved cells
D. radiodurans	*Deinococcus radiodurans*
E. coli	*Escherichia coli*
EMSA	Electrophoretic Mobility Shift Assay
EPR	Electron Paramagnetic Resonance
ESRF	European Synchrotron Radiation Facility
EXAF	Extended X-ray Absorption Fine Structure
FF	Forward
FOC	Ferroxidase center
Ftn	Ferritin
HEPES	4-(2-hydroxyethyl)-1-piperazineethanesulfonic acid
HPLC	High Performance Liquid Chromatography
H. pylori	*Helicobacter pylori*
ICP-AES	Inductively Coupled Plasma Atomic Emission Spectroscopy
IPTG	Isopropyl-β-D-thiogalactopyranosid
ITC	Isothermal Titration Calorimetry
I/σ(I)	Signal-to-noise ratio
LB	Luria broth
LB/Agar	Luria broth containing Agar
LMW	Low molecular weight
L. innocua	*Listeria innocua*
MAD	Multiple-wavelength anomalous dispersion

MES	4-Morpholineethanesulfonic acid
MID	Multiple isomorphous replacement
MOPS	3-(N-Morpholino)propanesulfonic acid
MR	Molecular replacement
MWCO	Molecular weight cut-off
M. arborescens	*Microbacterium arborescens*
M. smegmatis	*Mycobacterium smegmatis*
N	Image Number
NCS	Non-crystallographic symmetry
NPs	Nanoparticles
PEG	Polyethylene glycol
PCR	Polymerase chain reaction
PDB	Protein data bank
P. nautica	*Pseudomonas nautica* 617
OD_{600}	Optical density at 600 nm
RFQ	Rapid Freeze-Quench
rmsd	Root-mean-square deviation
ROS	Reactive oxygen species
RV	Reverse
SAD	Single-wavelength anomalous dispersion
SID	Single isomorphous replacement
SDS	Sodium dodecyl sulfate
SDS-PAGE	Sodium dodecyl sulfate polyacrylamide gel electrophoresis
SF	Stopped-Flow
SLS	Swiss Light Source
S. suis	*Streptococcus suis*
UV	Ultraviolet
UV-Vis	Ultraviolet-Visible
Tris	Tris(hydroxymethyl)methylamine
TEMED	N, N, N', N'-tetramethylenediamine
WT	Wild-type
12Fe-Dps	Dps incubated with 12 Fe(II)/Dps
12Cu-Dps	Dps incubated with 12 Cu(II)/Dps

1 Introduction

1.1 Iron – an essential element

Iron, the fourth most abundant element on Earth, is an essential and versatile transition metal for living organisms. [1,2]

At physiological conditions, free iron exists primarily in one of two readily inter-convertible oxidation states, the relatively soluble ferrous state, Fe(II), and the very insoluble ferric state, Fe(III). [3] This important nutrient for growth and development of most organisms can also adopt different spin states and redox potentials in both redox forms, depending on its ligand environment. [4]

Considering its chemical versatility and its abundance, iron is present in the active sites of many enzymes and oxygen carrier proteins, playing a crucial role in diverse cellular processes such as oxygen transport, nitrogen fixation, electron transfer reactions, respiration, DNA synthesis and gene regulation. [1,5]

Although the abundance of iron in the environment is high, under physiological, aerobic conditions and in the absence of anions to increase its solubility, the most stable oxidation state of iron is Fe(III), which mainly exists as an insoluble iron hydroxide. [6–8]

Consequently, iron bioavailability is extremely poor and often a limiting factor for bacterial growth. [9] Further, under aerobic conditions free iron is potentially toxic for cells due to its ability to catalyze the formation of reactive oxygen species (ROS). [10]

The reaction of Fe(II) ions with molecular oxygen (O_2) triggers the formation of reactive oxygen species, such as superoxide radical ($O_2^{\bullet-}$) or hydrogen peroxide (H_2O_2) according to the reactions (1.1) and (1.2). [3,5,7]

$$\mathrm{Fe(II)} + \mathrm{O_2} \rightarrow \mathrm{Fe(III)} + \mathrm{O_2^{\cdot -}} \tag{1.1}$$

$$2\mathrm{O_2^{\cdot -}} + 2\mathrm{H^+} \rightarrow \mathrm{H_2O_2} + \mathrm{O_2} \tag{1.2}$$

On the other hand, Fe(III) can be reduced back to Fe(II) by cytoplasmic reductants (1.3) resulting in a destructive catalytic cycle known as Haber-Weiss reaction. The presence of the free ferrous ions in cells can lead to the generation of toxic hydroxyl radicals via Fenton (1.4) and Haber-Weiss (1.5) reactions. [6,7,11]

$$\mathrm{Fe(III)} + \mathrm{O_2^{\cdot -}} \rightarrow \mathrm{Fe(II)} + \mathrm{O_2} \tag{1.3}$$

$$\mathrm{Fe(II)} + \mathrm{H_2O_2} \rightarrow \mathrm{Fe(III)} + \mathrm{OH^-} + \mathrm{OH^{\cdot}} \tag{1.4}$$

$$H_2O_2 + O_2^{\cdot -} \rightarrow OH^- + OH^{\cdot} + O_2 \quad (1.5)$$

The deleterious hydroxyl radicals, one of the most reactive species encountered in biological systems, are capable of damaging several cellular components, such as proteins, nucleic acids and membrane lipids, leading to abnormal function or inactivation. [5,7]

To overcome the poor availability and toxicity of iron and protect cells, organisms have developed mechanisms to both acquire and maintain iron in a non-toxic and soluble form, which is mainly achieved by a ubiquitous family of iron-storage proteins, the ferritins. [2,10]

1.2 Ferritin family

Ferritins, a family of iron storage proteins, is widely distributed across all three domains of life and have a critical role in the maintenance of iron homeostasis in most living organisms throughout evolution. [12,13]

Although DNA and amino acids sequences vary considerable (up to 80 %), the structural architecture of ferritin proteins is highly conserved. Ferritins are thus examples of proteins that possess an overall three-dimensional shape that is essential to their function. [13,14]

The ferritin superfamily is organized in evolutionary distinct subfamilies that have many structural and functional similarities: the classical ferritins (Ftn), the bacterioferritins (Bfr) and the DNA-binding proteins from starved cells (Dps). These subfamilies share the same characteristic four α-helix bundle fold, though the number of subunits that comprises them is different, originating two groups, maxi-ferritins (Ftn and Bfr proteins) and mini-ferritins (Dps). [4,13]

These protein cages composed by similar subunits folded into a four α-helix bundle have a three-dimensional structure similar to spherical shells, which provides the capacity to accommodate large amounts of iron in a non-toxic, soluble and bioavailable form. Nevertheless, the existence of structural differences leads to a mechanistic diversity. [11,15,16]

Protein cage assembly occurs spontaneously from 12 or 24 monomers, which build up a central hollow cavity that accounts for 30 % of the volume of ferritins. [17]

The maxi-ferritins consist of 24 subunits assembled into a protein cage with octahedral (432) symmetry, while the mini-ferritins are composed by 12 subunits with tetrahedral (32) symmetry (Figure 1.1). [18]

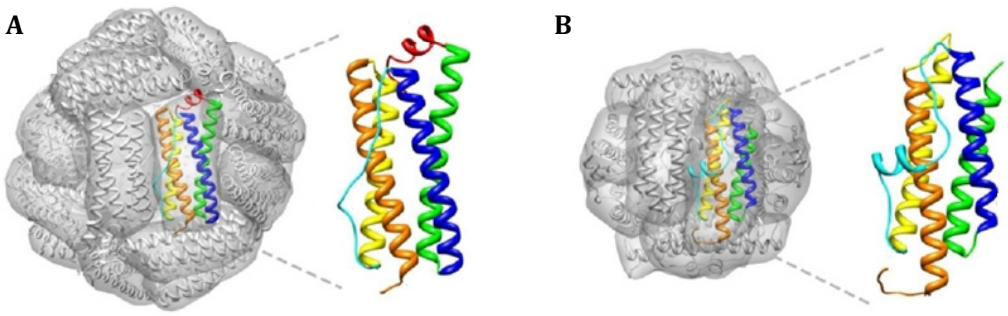

Figure 1.1 - Structures of the proteins cage from ferritin family. The four α-helix bundle monomers are showed as ribbons and a monomer is colored according to its secondary structure. A) Structure of a maxi-ferritin (PDB code: 1BFR). B) Structure of a mini-ferritin (PDB code: 1DPS). Adapted from [14]

These proteins, that form a hollow shell with an outside diameter of 12 or 9 nm and an inner diameter of 8 or 5 nm for maxi- and mini-ferritins, respectively, possess the dual function of iron detoxification and iron cellular reserve (Figure 1.2). [18,19]

Through a ferroxidation step catalyzed in the ferroxidase center (FOC) located within the protein shell (Figure 1.4), ferritins have the ability to store up to ~ 4500 or ~ 500 Fe atoms (maxi- and mini-ferritins, respectively). Iron stored in the form of a hydrous ferric oxide mineral core can have a variable amount of phosphate, which is related to variations in cytoplasmic phosphate (ratios of Fe:P~1:1 in plants and bacteria and ratios of Fe:P~1:8 in animals). [12,17]

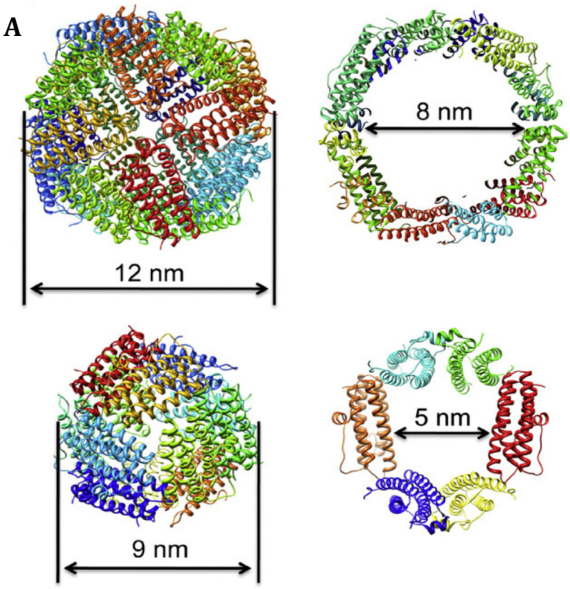

Figure 1.2 - Sizes and ribbon diagrams of exterior surface (left) and interior cavity (right) of a maxi and a mini-ferritin proteins. A) Maxi-ferritin (Human heavy-chain ferritin). B) Mini-ferritin (*Listeria innocua* Dps). [19]

Thus, the variability of the iron core crystallinity is influenced by the local concentration of phosphate during mineral formation. The high phosphate content leads to amorphous iron minerals in ferritin, whereas the ferritin mineral disorder is related to a low phosphate amount. Nevertheless, the iron core does not affect the electrophoretic or chromatographic properties of the ferritin. [13,17,20]

The ferritin protein cages without mineral are commonly defined as apoferritin and they can be isolated from recombinant growth or after reducing the mineral and chelating the iron under physiological conditions. The apoferritin shell is extremely stable due to the large numbers of intra- and inter-subunit salt bridges and hydrogen bonds. [12,18]

The classical ferritins are the archetypical members of the Ferritin family and are found in all three kingdoms of life. [16]

Contrary to ferritins from other organisms, Animal Ftns structures are constituted by tissue-specific combinations of different H (heavy, predominant in heart) and L (light, predominant in liver) subunits. Although these two types of subunits are closely related in terms of primary sequence and structure, their function is very different. The H-type is associated with the presence of FOCs, which catalyze the oxidation of Fe(II) ions, while L-type is thought to be involved in the nucleation of the iron core. [7,16]

Ftn and Bfr proteins exhibit many similarities and have the same biological purpose, the iron storage. However, Bfr proteins are restricted to bacterial and archaeal domains of life and contain twelve haems groups per molecule, non-covalently bound at the interface between two-fold related subunits. The role of the haem group (in most cases of the b-type) within the protein shell remains unclear. However, Weeratunga S. K., *et al.* demonstrated that it may be involved in Fe(III) mineral reduction and its release from the storage cavity. [4,6,13,21]

Despite both types of maxi-ferritins have the ability to sequester and incorporate ferrous iron, the function and regulation of these proteins is substantially variable depending on the different bacterial species. [22] For example, whereas the Ftn from *Escherichia coli* (*E. coli*) and the Bfr from *Salmonella enterica* sv. Typhimurium act as the principal iron storage proteins, the Ftn from *Helicobacter pylori* (*H. pylori*) is essential for host colonization and the Bfr from *Desulfovibrio vulgaris* has a Dps-like function. In some cases these proteins can also have dual roles as in *Bacteroides fragillis* and *Campylobacter jejuni*, where they are involved in both iron storage and redox stress response. [6,11]

On the other hand, Dps proteins, predominantly expressed in bacteria, are more distinct and generally function in iron detoxification as opposed to storage. These mini-ferritin proteins recognized as ferritin-like proteins due to its ferroxidase activity also have the ability to bind and protect DNA from oxidative damage. [12,23]

1.3 Dps protein

The Dps family (DNA-binding proteins from starved cells) is largely distributed and conserved through the bacterial kingdom. To date, over a thousand of Dps-like proteins have

been identified and approximately 97 % were found in bacteria, while the remaining 3 % were found in archaea. [24,25]

Typically bacterial genomes encode for only one Dps protein, while others encode for two or for three of these proteins (e.g.: *Bacillus anthracis* (*B. anthracis*) and *Streptomyces coelicolor*, respectively). [25,26]

The first Dps protein was discovered in *E. coli* in 1992 by Almirón *et al.* as a result of the analysis of proteins synthesized in 3-day-old cultures of *E. coli*. This protein described as a starvation-inducible DNA-binding protein with regulatory and protective roles in *E. coli* was found to protect cells from hydrogen peroxide and to bind DNA without apparent sequence specificity. [27]

Thus, the fundamental difference between Dps proteins and the maxi-ferritins (Ftn and Bfr proteins) is their ability to bind DNA and provide protection to cells during exposing to severe types of environmental assaults, such as nutritional deprivation and oxidative stress. [23,28]

The DNA binding ability is not shared by all members of Dps family (e.g. Dps from *Listeria innocua (L. innocua)*), though all of Dps proteins have the capacity to protect DNA from oxidative damage by sequestering iron and preventing the Fenton reaction. [24,29]

Regulation of Dps expression in *E. coli* cells is complex and partly dependent on the physiological state of the cell. It was found that ~ 6000 Dps molecules are present per cell in the exponential growth phase, reaching a maximum of ~180000 Dps molecules per cell at the late stationary phase, where Dps is the most abundant cellular protein. [23,30]

Furthermore, it has been proposed that Dps plays a role in gene regulation during starvation periods, since cells lacking Dps alter their protein expression pattern during starvation and fail to develop starvation-induced resistance to H_2O_2, an agent that cause oxidative damage to DNA. The synthesis of this protein increases dramatically in the stationary phase and continues after several days of starvation, depending on σ^s, a transcription factor that controls the expression of many starvation-induced genes. Therefore, this protein has the ability to make cells more resistant to cytotoxic assaults by controlling the expression of genes necessary for (or deleterious) to stress resistance. [23,27]

During stationary phase, Dps protects the cell not only against oxidative stress, but also from high pressure, UV and gamma radiation, acid and base shock iron and copper toxicity and thermal stress. [28]

The ability of Dps protein to provide wide protection against the stresses is based on its four intrinsic properties: DNA binding, metal binding and sequestration, ferroxidase activity and ability to affect gene regulation. [23,28]

The Dps fold and assembly were primarily described for *E. coli* by Grant *et al.* who demonstrated the similar structural features with those from ferritins. [31]

Despite the fold conservation, Dps-like proteins exhibit a variety of regulatory mechanisms and functions in addition to protection from oxidative stress and DNA-binding. Members of Dps family can have different regulatory properties according to the needs of each organism. Further, these proteins can act as important virulence factors conferring cell

protection against multiple stresses and can be useful in applications in bio and nanotechnology. [24]

Dps monomers with a molecular weight of ~18 kDa and four helix-bundle fold, differ from ferritins because they have a loop located between two helices that form a short helix exposed on the outside of the protein cage. [14,27]

These proteins are characterized by a central core that contains several conserved amino acids near to FOC and by N- and C-terminal regions with variable length and number of positive charges. [25]

Once assembled, Dps structure is very compact and stable with a highly flexible N-terminus that usually protrudes out of the dodecamer. The N-terminal region has been suggested to be important for the DNA-binding ability of Dps proteins and to stabilize the formation of the dodecamer. Further, the C-terminal has been proposed to be involved in the interaction with DNA as well. [31–33]

The surface as well as the internal cavity of the Dps dodecamers are mainly negatively charged, providing an ideal microenvironment for iron mineralization. [24,31,34]

The 23 symmetry of the Dps dodecamers creates pores at the junction of the threefold symmetry related subunits that connect the exterior of the dodecamer to the internal cavity. One pore is created by the N-terminus ends of the subunits and was named “ferritin-like” since it is lined by negatively charged residues similar to the pores formed at the 3-fold symmetry axes in ferritins. This pore is highly hydrophilic and it has a negative electrostatic potential created by the negatively charged residues lining the pores, which may attract iron entry into the protein and guide it toward the FOC. The other type of pore is formed by the C-terminal ends of the subunits and is unique to Dps proteins. This pore called “Dps-type” is mainly hydrophobic and its function is still unknown, possibly because it displays more sequence variability among Dps proteins than the N-terminal pores. [25,29,35,36]

1.3.1 Ferroxidase activity

Despite the structural conservation within the Ferritin family, the FOC represents the most distinct structural feature of the Dps proteins relative to maxi-ferritins. [37]

Within the Dps dodecamer, twelve FOCs exist and they are located at the interface between 2-fold symmetry-related monomers rather than within the four-helix bundle of a single subunit as in all maxi-ferritins (Figure 1.3). Therefore, at the interface there are two FOCs and the metal binding site is composed of conserved histidine and carboxylate residues provided by the two monomers symmetry-related. [23,24,36]

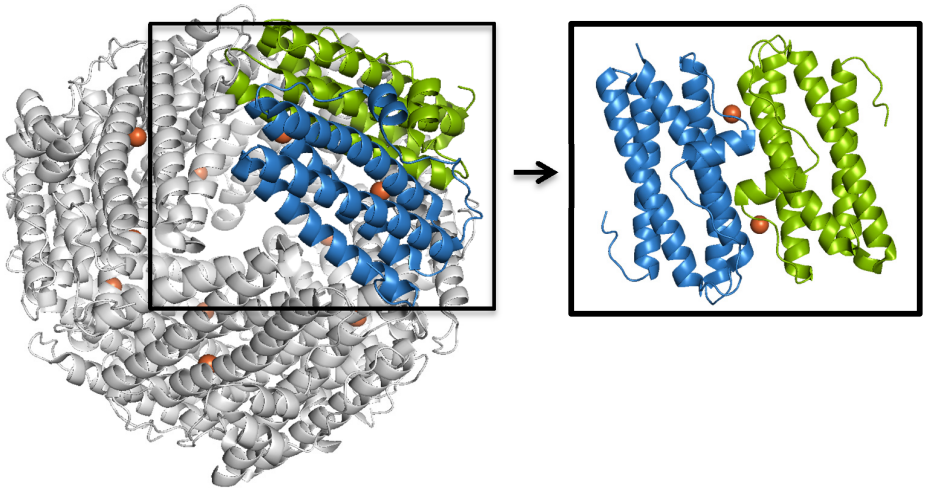

Figure 1.3 - Overall structure of the *Streptococcus suis* (*S. suis*) Dpr complexed with iron atoms. Two monomers are highlighted in a different color and consist of two subunits symmetry-related with two FOCs where the iron is bound. Iron atoms are showed as orange spheres. The subunit–subunit interface is evidenced in the black box. (PDB code: 2CF7) Adapted from [38]

Despite the high conservation of the metal coordinating residues, the occupancy of the metal binding sites with iron varies significantly in the known crystal structures. [25]

FOCs catalyze the reaction that converts soluble Fe(II) ions to a Fe(III)-ferrihydrite mineral core, where iron remains tightly bound until its release becomes necessary for biological processes. [22,23]

Typically FOCs of Ferritin family located within each monomer are bimetallic, with two iron atoms located at a maximum distance of 3 Å and connected by an oxo-bridge. The so called A with high affinity site uses a histidine and carboxylate residues as iron coordinating ligands, whereas the so called B site with low affinity used only carboxylate residues for the iron coordination. However, for most of the Dps proteins studied so far a mono-iron ferroxidase site was observed instead of a di-iron site (Figure 1.4). [25,39]

For some Dps-like proteins a conserved water molecule was modeled instead of iron in the B site, which is the case of *L. innocua* Dps, where the FOC contains one iron atom and one water molecule with a distance of about 3 Å. On the other hand, the FOC of Dps from *H. pylori*, *Deinococcus radiodurans* (*D. radiodurans*) and *Agrobacterium tumefaciens* (*A. tumefaciens*) contains only one iron atom bound at the A site, whereas the FOC of *E. coli* Dps is occupied by two water molecules. [29,31,34,35,40]

Thus, this variability in iron occupancy indicates that the residues forming the second metal coordination site influence the affinity of the FOC for iron. [25]

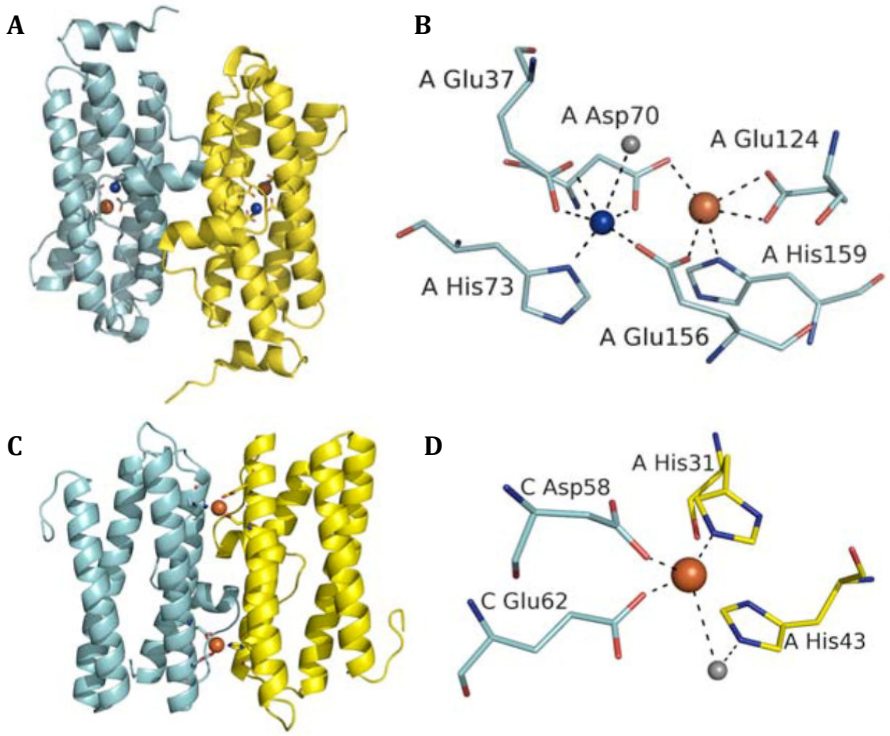

Figure 1.4 - FOCs of maxi and mini-ferritins proteins. A) The dimer interface of bacterioferritin-like protein from *S. solfataricus* showing one FOC per monomer. B) The FOC of bacterioferritins-like proteins, contains a mixture of metals at both the A- and B-sites. C) The dimer interface of Dps-like protein from *L. innocua* Dps showing two FOCs between two monomers. D) The FOC of Dps-like proteins. Adapted from [24]

Despite the overall conservation of the Ferritin family, the ferroxidase activity of Dps proteins has distinctive features and the iron coordinating residues located in the FOCs are different. [25,41]

In contrast to maxi-ferritins that generally use O_2 as iron oxidant, Dps proteins utilize preferentially H_2O_2. For Dps proteins, iron oxidation with hydrogen peroxide occurs at much higher rate and is about 100-fold more efficient than with O_2. This disparity may be due to the difference of the amino acids that constitute the FOCs of maxi- and mini-ferritins. [28,36,42]

Considering the binding of two ferrous ions to each FOC of Dps proteins, two ferrous ions are oxidized for every molecule of H_2O_2 and the ferric iron is mineralized at the core of the dodecamer as insoluble hydrous ferric oxide (FeOOH), according to the following reaction (1.6). [23,36]

$$2\mathrm{Fe(II)} + \mathrm{H_2O_2} + 2\mathrm{H_2O} \rightarrow 2\mathrm{FeOOH} - \mathrm{P} + 4\mathrm{H^+} \qquad (1.6)$$

Therefore, the pairwise oxidation of Fe(II) by H_2O_2 within Dps greatly attenuates hydroxyl radical formation through Fenton reaction and cells are protected against oxidative stress. [25,42]

Dioxygen can also be used in the ferroxidase reaction, though it is less efficient than hydrogen peroxide. In this case, the following reaction (1.7) takes place during iron oxidation and mineralization. [24,28]

$$4\mathrm{Fe(II)} + \mathrm{O_2} + 6\mathrm{H_2O} \rightarrow 4\mathrm{FeOOH} - \mathrm{P} + 8\mathrm{H^+} \quad (1.7)$$

The iron oxidized and mineralized is stored within the protein cavity until being released for intracellular use. So far, very little is known about how the dissolution of the Fe core occurs *in vivo*. Even though, *in vitro* experiments showed that Fe mobilization can occur in the presence of Fe(III) chelators or reductants, it is not clear if the chelators and reductants have the capacity to penetrate the protein shell and reduce the iron core. [22,43]

1.3.2 DNA binding ability

The DNA-binding ability of Dps protein was discovered for *E. coli* Dps when Dps-DNA complexes were formed, *in vitro*, by the addition of purified Dps to supercoiled plasmid and linear DNA. [27]

Binding assays *in vitro* evidenced the formation of extremely stable Dps-DNA complexes that do not dissociate even after treatment with detergents or solvents and when incubated up to 100°C. An additional property observed is that DNA bound to Dps does not reveal a clear footprint after DNase I digestion. [27] This binding property is similar to other histone-like proteins, such as the heterodimeric protein HU associated with the *E. coli* nucleoid and the heat-stable nucleoid-structuring protein H-NS, despite Dps does not share amino acid sequence of structural similarities with these proteins. [23,44]

Therefore, this binding characteristic of *E. coli* Dps demonstrates its ability to bind DNA without apparent sequence specificity. [27]

However, DNA is unable to bind directly to the surface of Dps protein because the surface of Dps does not display DNA-binding motifs and is mainly negatively charged (Figure 1.5). [31]

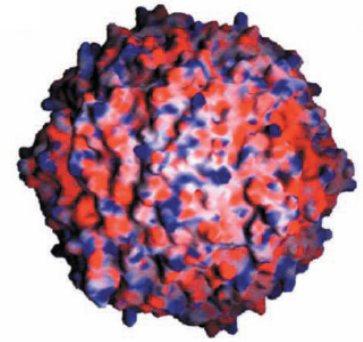

Figure 1.5 - Electrostatic surface potential of the *E.coli* Dps dodecamer. The positive charges of the molecular surface are colored in blue, whereas the negative charges are colored in red. [31]

Based on the X-ray crystal structure of *E. coli* Dps and its electrostatic surface potential, it has been suggested that DNA binding involves interactions with three positively charged residues (lysines) of the N-terminus. This highly mobile region that protrudes out from the surface of the dodecamer was disordered and thus it was not observed in the electron density maps of the structure. [31]

On the other hand, it has been recently proposed that the interaction is mediated by Mg^{2+} ions that form multiple ion bridges between Dps and DNA. These ion bridges can only be formed upon a specific concentration of Mg^{2+}, because otherwise the surfaces of both molecules become similarly charged and consequently repel each other. [45]

The inhibition of DNA binding by *Lactococcus lactis* Dps in the presence of EDTA supports the suggestion that divalent cations are required for the formation of the Dps-DNA complexes. [33]

Even though the lysine residues of N-terminal region as well as the divalent cations have been found to be important for DNA binding, the exact binding mechanism is still not completely understood. [24]

The binding of Dps proteins to DNA results in the formation of Dps-DNA biocrystals. Despite the crystalline state is considered to be incompatible with life, co-crystallization of DNA and Dps in cells in living systems may provide an efficient means of protection against severe environmental assaults. [23,24]

Electron microscopy studies of Dps and Dps-DNA complexes, conducted on *E. coli* cells showed that Dps form a layered crystalline structure characterized by a pseudo-hexagonal packing. Moreover, the addition of DNA accelerates this crystallization process and the interaction between purified Dps and DNA results in the formation of an extremely stable crystal without disturbing the layer packing. This highly organized co-crystallization process is obtained with supercoiled plasmids, linear double-stranded DNA, as well as single-stranded RNA molecules without a significant difference in the resultant crystalline structure. [46,47]

DNA-Dps co-crystallization in a well-ordered multi-layered structure has been detected in the cytoplasm of starved bacterial cells and was proposed to represent a general binding mode that provides protection of DNA by physical sequestration. [48]

This hypothesis was supported by results of differential interference contrast (DIC) and fluorescent microscopy studies, which suggested that DNA is incorporated within the Dps

crystalline structure and by the fact that members of the Dps family without a positively charged N-terminus (Dps from *L. innocua*, *B. anthracis* and *H. pylori*) do not appear to bind DNA. [26,29,46]

Therefore, based on the crystal structures of Dps proteins and on electron microscopy studies for *E. coli* Dps, two hypothetical models for DNA binding have been proposed (Figure 1.7).

The first model proposed from the crystal structure of *E. coli* Dps by Grant, R. A. *et al*, suggests that the DNA helices could be inserted and bind DNA in the holes created between three adjacent dodecamers (Figure 1.6, A). These holes are occupied by disordered N-terminus residues that are not present in the model, so the positively charged lysine residues could interact with DNA molecules. If Dps dodecamers could adjust their position, all of the interactions between adjacent dodecamers would be identical and a perfect hexagonal two-dimensional lattice would be created in which all the holes would be similar and sufficiently large to accommodate DNA molecules. [24,31]

On the other hand, the second model (Figure 1.6, B) is more recent and proposes that the addition of DNA to Dps does not disturb the hexagonal packing and DNA molecules could be packed between the layers of Dps dodecamers in the structure. This model was further supported by the X-ray crystal structure of *Bacillus brevis* (*B. brevis*) Dps, which showed that the multi-layered structure of Dps forms grooves that lead to channels. These could accommodate DNA molecules alternatively displayed in spaces between the multi-layers of Dps dodecamers. [47]

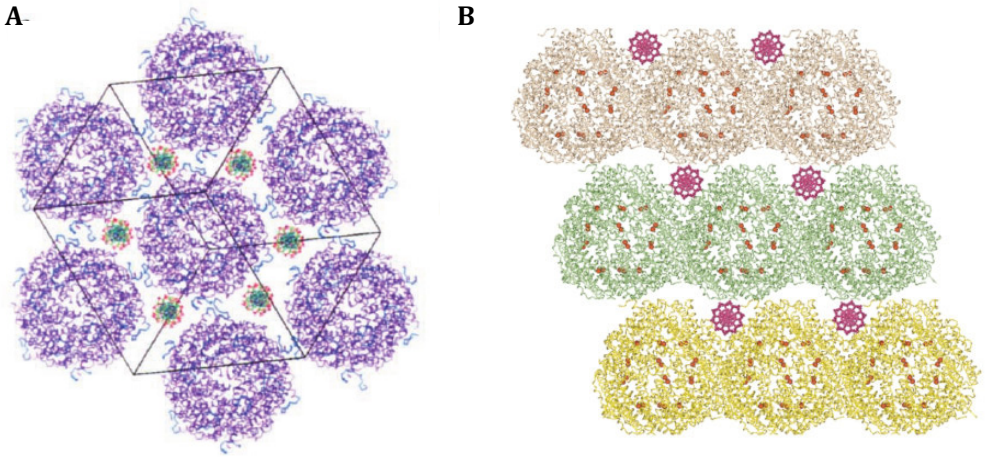

Figure 1.6 – Representations of the proposed DNA binding models. A) Model for DNA binding where the DNA molecules could be inserted in apertures between neighboring dodecamers. The Dps dodecamer is colored in purple and the N-terminal stretches are showed in blue. The DNA helices presented were modeled in green with phosphates colored in red. The outline of the unit cell is showed in black. [31] B) Model for DNA binding where the DNA molecules could be accommodate in the spaces between alternated layers of Dps dodecamers. [47]

Hence, Dps can provide a bimodal protection to chromosomal DNA within the cells during starvation conditions. This can be achieved directly through physical sequestration of

DNA molecules and indirectly with the oxidation of ferrous atoms by hydrogen peroxide that reduces the production of toxic hydroxyl radicals via Fenton reaction. [23,24]

1.3.3 Applications

Several applications in the field of biotechnology and nanotechnology have been exploited using Dps proteins.[24] The protein assembly provides a size and shape constrained reaction environment for the synthesis of nanomaterials, such as magnetic nanoparticles (NPs) and catalytic materials with different compositions, sizes and properties. The chemical nature of these proteins cages can be altered, which significantly changes their synthetic utility.[49,50]

Iron oxide NPs synthesized within the Dps protein cage can be used to catalyze the formation of carbon nanotubes with a narrow diameter distribution. [51] Besides that, these proteins can also be loaded with cobalt, producing cobalt oxide NPs, as an alternative catalyst source for the production of carbon nanotubes. The benefit of using protein cages as nanocontainer is that the cores can be selectively loaded to control the size of the particles. [52,53] For example, Dps protein from *L. innocua* has been used for the synthesis of magnetic NPs to explore the fine-tuning size-dependent magnetic properties. [54]

2 Objectives

In the past years, maxi-ferritins have been extensively studied and are now very well characterized. Even though maxi-ferritins are structurally similar to mini-ferritins, the knowledge about mini-ferritins is still limited.

So far, it is known that Dps proteins are able to capture and store iron in its inner cavity. Besides, it has been demonstrated that some of these proteins also have the ability to bind and protect DNA. However, the mechanism of iron incorporation and release is not fully clear and very little is known about the interaction of the DNA with Dps. A lysine-rich N-terminal region of the protein has been suggested to be required the DNA binding, but the exact mechanism of binding is still not completely understood.

Based on what was stated above, the focus of this thesis was the study of the functional and structural features of a recombinant Dps from *Pseudomonas nautica* 617 (*P. nautica*), where the main goals are described below.

The first goal consisted on the investigation of the mechanisms of iron incorporation by Dps protein. Previous work has demonstrated the ferroxidase activity of Dps wild-type (WT), but the exact molecular mechanism is still under debate. Therefore, a Dps variant where a phenylalanine, suggested to be important for the iron incorporation, is replaced by a glycine was studied, aiming to elucidate about the role of this amino acid in the iron incorporation or iron oxidation in the FOC.

The second goal was the structural characterization of the metals incorporation into the protein, such as iron and copper, using X-ray crystallography. As described in the literature, Dps proteins can be used to produce metallic NPs with a narrow size. Previous studies showed the ability of this protein to bind copper as well as the formation of heterometallic cores. However, it is still not clear if the FOC is mononuclear or binuclear and is unknown where the copper binding takes place in this Dps protein and how the core formation is accomplished. Cu(II) is a stable metal and a good paramagnetic probe. Therefore, Dps could be used to metabolize copper and increase the resistance of cells to the copper toxicity as well as a structural probe for the mechanism of iron binding and for the production of metallic NPs.

The third goal was the characterization of the Dps-DNA interaction. Previous studies have shown the DNA binding ability of this Dps and the involvement of the N-terminus in the interaction. Thus, Dps variants were studied to obtain more insights about how such interaction is established. Electrophoretic mobility shift assays (EMSAs) were performed with a Dps variant where a glutamine is replaced by a glutamate. Further, point mutations were done in the N-terminal region of this protein to increase the strength of the interaction, which could help in the co-crystallization of Dps with DNA.

3 Material and Methods

3.1 Materials

3.1.1 Chemicals

The chemicals and reagents used to prepare buffers and solutions were of analytical purity grade (p.a.) and obtained from the following companies: Sigma-Aldrich, Panreac, Fluka, Merck, AppliChem, NZYTech, VWR Prolabo and LabChem.

3.1.2 Bacterial strains

E. coli strain NZY5α (NZYTech) was used for plasmid amplification and DNA isolation, whereas *E. coli* strain NZYStar (NZYTech) was utilized for amplification and isolation of the plasmid originated in the site-directed mutagenesis protocol. For gene expression the *E. coli* strain BL21(DE3) (NYZTech) was used.

3.1.3 Plasmids

The pET-21c(+) plasmid (Novagen), showed in Figure 3.1, was used as expression vector for the recombinant Dps WT and variant proteins in *E. coli*. This ampicillin-resistant expression vector pET21c-PnDps containing the coding gene for the Dps WT from *P. nautica*, was previously prepared by Márcia Guilherme. [55]

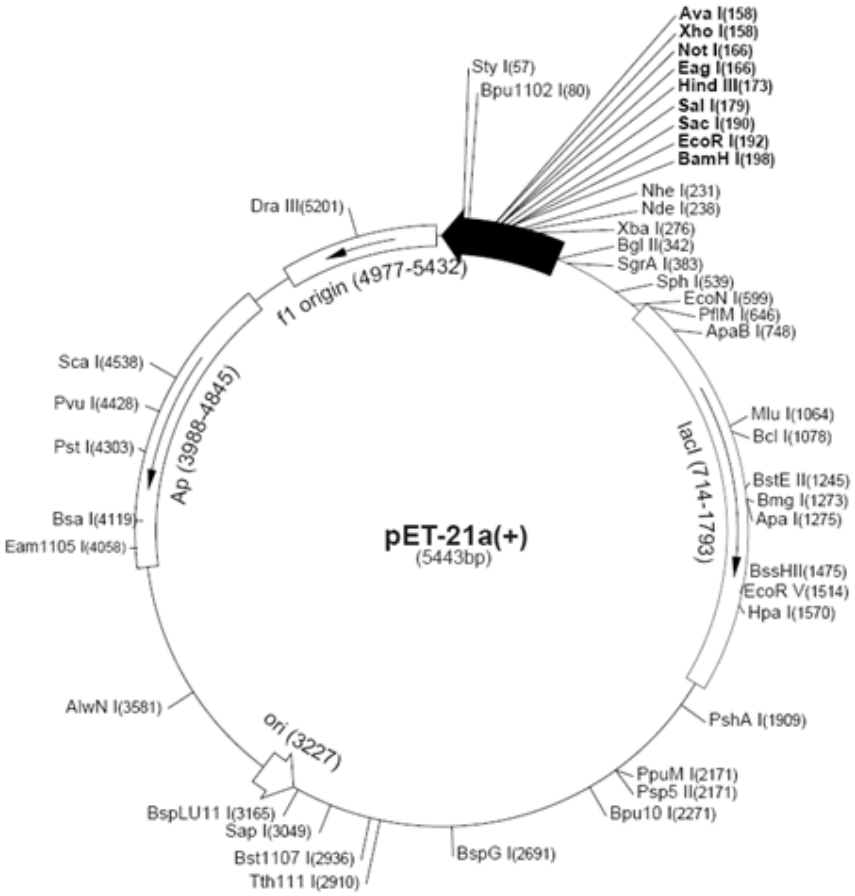

Figure 3.1 – Map of pET-21a-d(+) plasmid (Novagen). Overview of the restriction sites of the vector showed as a circle map. [56]

The pUC19 plasmid with 2686 bp and 1772.76 kDa, showed in Figure 3.2, was used for the DNA binding assays.

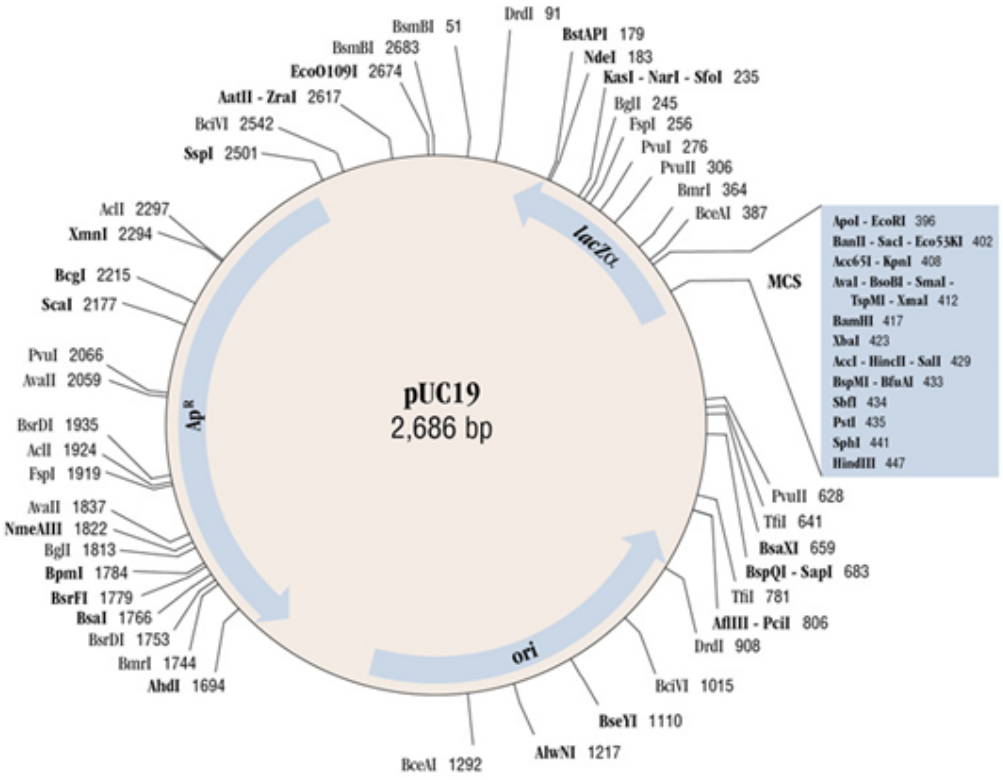

Figure 3.2 - Map of pUC19 plasmid with 2686 base pairs and 1772.76 kDa (GenBank Accession #: L09137).

3.1.4 Growth media

The growth media used and their formula are listed in Table 3.1. In contrast to the 2xYT medium, the LB and LB/Agar media (NZYTech) were already prepared and ready to be used. The growth media (25 g for LB and 35 g for LB/Agar) were always dissolved in 1 L of distilled water and autoclaved at 121 °C for 20 min. The solutions were allowed to cool-down before adding antibiotics (Ampicillin 100 mg/mL). The LB/Agar medium was then distributed in sterile Petri dishes, turning solid when completely cooled.

Table 3.1 - Growth media used and their composition and concentration (g/L).

Medium	Composition	Concentration (g/L)
LB	Tryptone	10
	NaCl	10
	Yeast extract	5
LB/Agar	Tryptone	10
	NaCl	10
	Yeast extract	5
	Agar	12
2xYT	Tryptone	20
	NaCl	20
	Yeast extract	10

3.1.5 Kits and Molecular Weight Markers

The kits used for DNA mutagenesis and DNA isolation (Miniprep and Midiprep) as well as the molecular weight marker (Low molecular weight) used for Sodium dodecyl sulfate polyacrylamide gel electrophoresis (SDS-PAGE) and agarose gel electrophoresis (NZYLadder II and NZYLadder III) were purchased from NZYTech and used according to the respective manuals. The electrophoretic profiles of the molecular weight markers are presented in Figure 3.3.

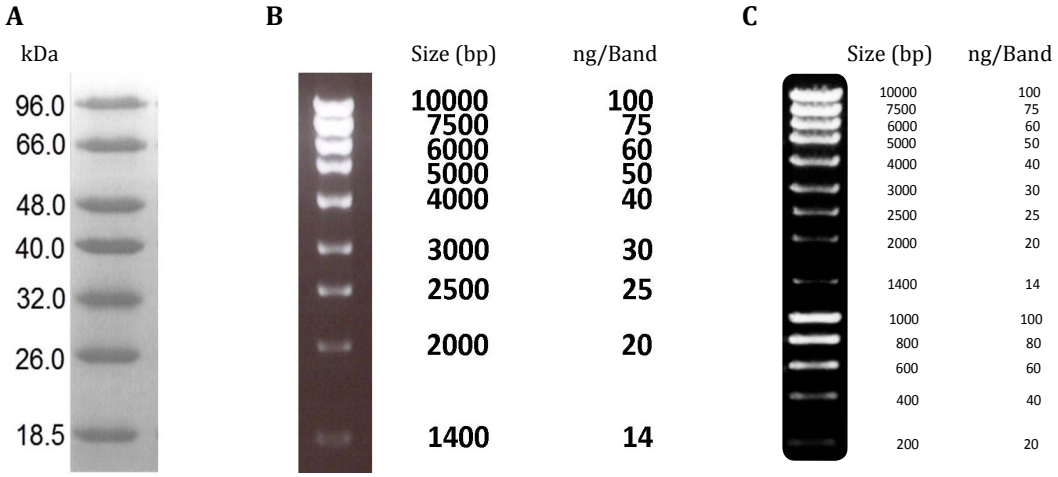

Figure 3.3 - Molecular weight markers used for electrophoresis gel. A) Low Molecular Weight Protein Marker (LMW). [57] B) NZYLadder II Marker. The molecular weight (bp) and the quantity of DNA (ng) of each DNA marker are indicated on the right side of the gel. [58] C) NZYLadder III Marker. [59]

3.1.6 Chromatography

For Dps purification the an ÄKTA Prime chromatography system (GE Healthcare) controlled by the PrimeView software were used. The chromatographic columns used as well as their characteristics are listed in Table 3.2. The columns were used according to the manufacturer's instructions and stored in 20 % EtOH.

Table 3.2 – Chromatographic columns used for protein purification as well as their characteristics and the respective manufacturer.

Column	Characteristics	Manufacturer
DEAE Sepharose Fast Flow	Weak anion exchanger Volume 160 mL Pressure Max. 0.3 MPa	Amersham Biosciences
Resource Q	Strong anion exchanger Volume 6 mL Pressure Max. 0.6 MPa	GE Healthcare
Superdex 200	Size exclusion 10-600 kDa Volume 82 mL Pressure Max. 1.5 MPa	GE Healthcare

3.2 Methods

3.2.1 Transformation of competent cells

Transformation of competent *E. coli* BL21 (DE3) cells was performed according to the manufacture's protocol. Cells were transformed with the expression vector pET21c-PnDps. The plasmid DNA was added to the cells and the transformations were incubated on ice for 30 min, followed by heat-shock at 42 °C for 40 s. Further 2 min of incubation on ice were performed, 900 µL of LB medium were added and the cells were incubated at 37 °C for 1 hour at 220 rpm.

After transformation, cells were plated in sterile Petri dishes containing LB/Agar medium with Ampicillin (100 mg/mL) and incubated overnight at 37 °C.

3.2.2 Protein expression

Test for protein expression in *E. coli*

Test expressions for Dps F46G expression in *E. coli* BL21(DE3) were performed in

order to find the best expression conditions by varying the culture media (LB and 2xYT), the induction agent (isopropyl-β-D-thiogalactopyranosid, IPTG 0.1, 0.5 and 1 mM), the optical density at 600 nm (0.5 or 2) and incubation time after induction (3 or 16 hours).

The bacterial growth was carried out at 37 °C and 200 rpm. Aliquots were taken every hour until 16 h after induction.

Samples were normalized considering OD_{600} and protein expression profile of each of them was evaluated by SDS-PAGE electrophoresis.

Protein expression and cell harvesting

For Dps WT expression, a single colony was picked and inoculated in 5 mL of LB medium containing Ampicillin (100 mg/mL) at 37 °C and 200 rpm for 8 h.

Then, 1 mL of pre-culture was inoculated in 100 mL LB medium containing Ampicillin (100 mg/mL) and incubated at 37 °C and 220 rpm for 16 h.

Expression cultures of 1 L were grown at 37 °C and 200 rpm in LB medium with Ampicillin (100 mg/mL). Induction was done with 0.5 mM IPTG at and OD_{600} of 0.5.

After 3 h of induction, the expression cultures were harvested by centrifugation for 10 min at 10,000 x g and 8 °C (Z 36 HK, HERMLE LaborTechnik). The cell pellets were collected and the wet cell mass was determined. Before storage at -80 °C, the pellets were resuspended in 10 mM Tris-HCl,pH 7.6.

For Dps F46G expression, the procedure used for was similar to the described for the WT. However, in this case, the medium used was 2xYT and the cells were induced by addition of 0.1 mM IPTG.

Cell disruption

The soluble cellular content was isolated from the remaining cellular components, before proceeding with the purification.

Cells were disrupted in two steps. In a first step cell disruption was performed by freeze-thaw cycles. The second step consisted in using an ultrasonic homogenizer equipped with a 7 mm diameter probe (LABSONIC M, Sartorius). Cells were disrupted through 3 or 7 cycles for Dps WT and Dps F46G, respectively, and each cycle consisted of 3 min of continue sonication with an amplitude of 80 % and 1.5 min of incubation on ice.

During cell disruption DNase I (Roche) was added to cell suspensions to reduce the viscosity of the cellular extract.

Cell suspensions were centrifuged at 10,000 x g and 8 °C for 10 min (Z 36 HK, HERMLE LaborTechnik). Further, cells were ultracentrifuged at 130,000 x g and 4 °C for 1 h 30 min to separate the membrane and the soluble fractions. The pellets were then resuspended in 10 mM Tris-HCl pH 7.6 and stored while the supernatant, containing the Dps

protein (soluble extract), was dialyzed overnight against 10 mM Tris-HCl, pH 7.8. SDS-PAGE gel electrophoresis was performed with all the cellular fractions mentioned above.

3.2.3 Protein purification

For the purification of Dps protein, the dialyzed cellular extract was centrifuged at 10000 x g and 8 °C for 10 min and filtered with a 0.45 µm membrane filter.

After each purification step, Dps fraction purity was assessed by SDS-PAGE electrophoresis (12.5 % acrylamide).

Dps protein fractions were tested for catalase contamination.

Ionic exchange chromatography

As a first purification step, a DEAE Sepharose Fast Flow column was used. The dialyzed cellular extract was loaded onto the column and washed with equilibration buffer (10 mM Tris-HCl buffer pH 7.6). Dps protein was then eluted with a discontinuous gradient of buffer 10 mM Tris-HCl buffer pH 7.6 and 500 mM NaCl. A flow rate of 5 mL/min was used and 12 mL fractions were collected.

For Dps WT, a second step of ion exchange step was done using a Resource Q column. The dialyzed protein was loaded onto the column with a flow rate of 4mL/min and washed with the equilibration buffer (10 mM Tris-HCl buffer pH 7.6). Dps protein was eluted with a continuous linear gradient of elution buffer 10 mM Tris-HCl buffer pH 7.6 and 500 mM NaCl). A flow rate of 1 mL/min was used and 4 mL fractions were collected.

Size exclusion chromatography

To separate further impurities from the target protein a size exclusion chromatography step was carried out using a Superdex 200 column. The column was equilibrated with a running buffer containing 10 mM Tris-HCl buffer, pH 7.6 and 500 mM NaCl and a concentrated protein sample was loaded onto the column. Protein was eluted with a flow rate of 1.5 mL/min and collected in 2 mL fractions.

3.2.4 Protein concentration determination

Protein concentration was determined by UV-Visible spectroscopy by measuring three samples prepared with different dilutions. The molar extinction coefficient of Dps protein at 280 nm, $2.93 \times 10^5\ M^{-1}cm^{-1}$ was used for the quantification. [55]

3.2.5 Electrophoresis

SDS-PAGE

SDS-PAGE is a technique widely used for the determination of protein's molecular mass and to verify the protein purity.

Gel polymerization was performed according to the protocol described by Laemmli, using the solutions and volumes showed in Appendix 8.1, Table 8.1. [60]

The samples were prepared by adding sample buffer containing β-mercaptoethanol in a 1:1 ratio and heated in boiling water for 5 min. Then, the samples were loaded on a 5 % stacking gel and the separation was done using a 12.5 % running gel.

The electrophoresis was carried out in the Mini-PROTEAN Tetra System (BIO-RAD) with a fixed voltage (80 V for the first 30 minutes and 120 V until the end of the run) in 1 x Tris-Glycine running buffer pH 8.3.

For the visualization of the protein bands, gels were stained with Coomassie Brilliant Blue R-250 staining solution for 30 min and destained using a methanol/acetic acid solution. After this gels were photographed with Gel Logic 100™ (Kodak).

The stock solutions for SDS-PAGE were prepared according to the described in Appendix 8.1, Table 8.2.

Agarose gel electrophoresis

Agarose gel electrophoresis is commonly used in the determination of DNA or RNA fragment's molecular weight and to assess the purity. This technique allows the separation of nucleic acids fragments according to their size by applying an electric field.

The concentration of agarose in each gel range between 0.8 and 1 % (w/v). Samples were prepared by adding BlueJuice™ Gel Loading Buffer (Invitrogen) in a 1:1 ratio to the DNA sample.

Electrophoresis was carried out at 80 V for 1 h 30 min in 1x TAE (v/v) buffer (40 mM Tris-acetate pH 8 and 0.1 mM EDTA).

After electrophoresis, gels were stained with SYBR Safe (Invitrogen) solution for 20-30 min. Gels were then imaged with Safe Imager™ (Invitrogen) and photographed with Gel Logic 100™ (Kodak).

3.2.6 Iron uptake assays

Iron incorporation and storage mechanism in Dps proteins can be studied by ferrous iron uptake assays. As described in literature, besides ferrous iron, these proteins can use two different co-substrates for the iron oxidation in the FOC, hydrogen peroxide (H_2O_2) and molecular oxygen (O_2).

To analyze the role of phenylalanine 46 in the iron incorporation mechanism, iron uptake assays were performed using the two co-substrates and two Dps variants, WT and the Dps F46G mutant.

The assays were monitored by UV-Visible spectroscopy, using an Evolution 300 spectrophotometer (Thermo Scientific) connected to a computer using VISION pro™ software. Quartz cuvettes of 3 mL (Hellma Analytics) were used. The baseline was performed with the reaction buffer, 200 mM MOPS buffer pH 7 and 200 mM NaCl.

A ferrous iron chloride solution was prepared and quantified using the protocol described below.

Iron quantification

Iron quantification performed by a colorimetric assay based on the reaction of 1,10-phenanthroline with Fe(II) solution. In this assay, hydroxylamine hydrochloride is used to reduce the iron to its ferrous state through the following reaction (3.1).

$$2\mathrm{Fe\ (III)} + 2\mathrm{NH_2OH} + 2\mathrm{OH^-} \rightarrow 2\mathrm{Fe(II)} + \mathrm{N_2} + 4\mathrm{H_2O} \qquad (3.1)$$

After this, Fe(II) reacts with 1,10-phenantroline and forms an orange-red complex (Figure 3.4) that can be monitored through UV-Vis absorption spectroscopy at 510 nm, which has a characteristic molar extinction coefficient of 11.2 $mM^{-1}cm^{-1}$. The iron content in each sample is proportional to the formation of the Fe-1,10-phenantroline complex. [61,62]

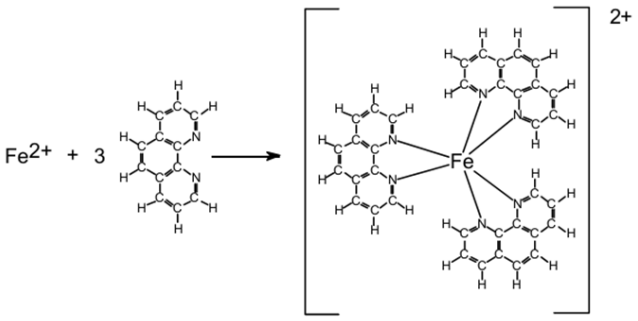

Figure 3.4 - Reaction of Fe(II) with 1,10-phenanthroline with the formation of the Fe-1,10-phenantroline complex. [61]

For the iron quantification a calibration curve was performed using a standard Fe(II) solution (0.01 mg/mL) and following a protocol adapted from Maloney, K. M., *et al*. [63] The standard iron solution was prepared using Milli-Q water at pH 3 to prevent the formation of iron oxides/hydroxides. After preparing the $FeCl_2$ samples and the standards (in triplicate) for a final volume of 5 mL, the absorbance measurements were carried out at 510 nm (Table 3.3 and 3.4).

Table 3.3 - Composition and experimental procedure applied do the standards solutions and used to obtain the calibration curve.

Reagent	Standard Tube (mL)					
Standard Fe solution	0	0.2	0.4	0.8	1.2	1.6
Milli-Q water	2.5	2.3	2.1	1.7	1.3	0.9
Mix (vortex)						
10% Hydroxylamine	0.4	0.4	0.4	0.4	0.4	0.4
Mix (vortex)						
0.3% Phenantroline	0.4	0.4	0.4	0.4	0.4	0.4
Mix (vortex) and wait 10 min						
Milli-Q water	1.7	1.7	1.7	1.7	1.7	1.7
Absorbance measurement at 510 nm						

Table 3.4 - Composition and experimental procedure applied to the iron samples used for the iron quantification.

Reagent	Sample Tube (mL)		
$FeCl_2$ solution	0.3	0.6	0.9
Milli-Q water	2.2	1.9	1.6
Mix (vortex)			
10% Hydroxylamine	0.4	0.4	0.4
Mix (vortex)			
0.3% Phenantroline	0.4	0.4	0.4
Mix (vortex) and wait 10 min			
Milli-Q water	1.7	1.7	1.7
Absorbance measurement at 510 nm			

With the absorbance measurements, the calibration curve was calculated and the molar extinction coefficient used for iron quantification was determined (Figure 3.5).

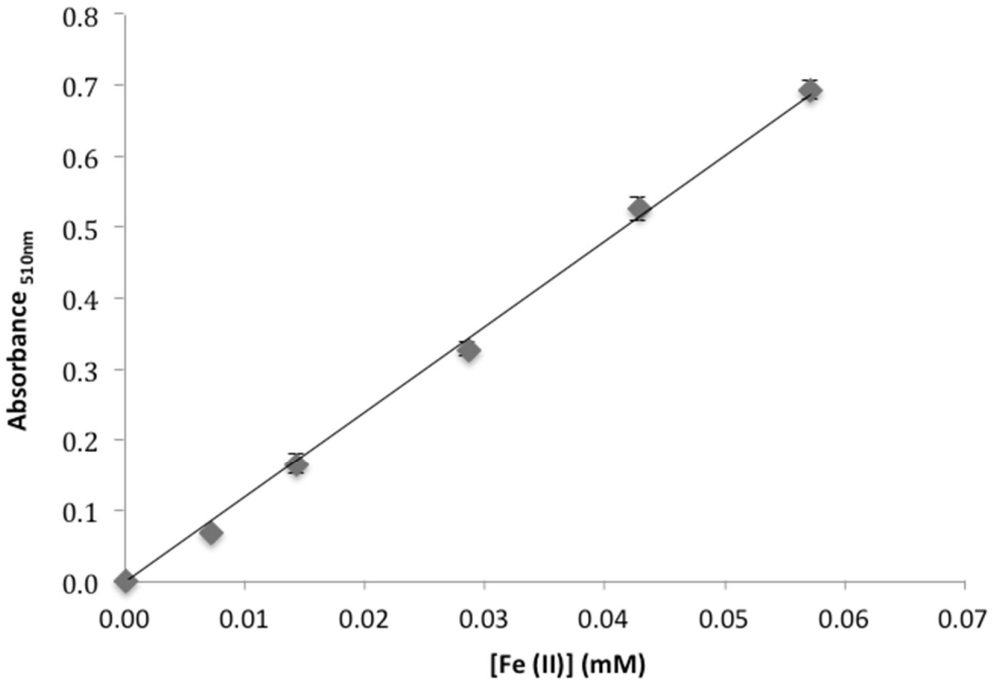

Figure 3.5 - Calibration curve obtained with the Fe standard solution. Experimental results were best fitted with the following equation: Abs_{510}= 12.038[Fe(II)] ± 0.16 (R^2=0.99786).

The iron content in the samples was determined using the calibration curve equation obtained (Figure 3.5). All the samples were quantified and the iron concentration calculated with the Lambert-Beer's Law and taking into account the dilutions performed (Table 3.5).

Table 3.5 - Iron quantification using the calibration curve.

Sample Tube (mL)	Abs_{510}	[Fe] (mM)	[Fe] median taking dilutions into account (mM)	StDev (mM)
0.3	0.134	0.498		
0.3	0.143	0.498		
0.3	0.139	0.498		
0.6	0.261	0.581		
0.6	0.247	0.581	1.826	0.005
0.6	0.265	0.581		
0.9	0.369	0.665		
0.9	0.376	0.665		
0.9	0.382	0.665		

The iron concentration of the $FeCl_2$ stock solution prepared for the loading assays was 1.826 ± 0.005 mM (Table 3.5).

Iron uptake assays using H_2O_2 as co-substrate

To determine maximum iron load by Dps WT and Dps F46G, consecutive additions of 48 Fe(II)/protein (9.6 μM of $FeCl_2$) followed by an excess of H_2O_2 (19.2 μM of H_2O_2, previously quantified by UV-Vis spectroscopy) were performed under aerobic conditions.

The additions were performed to a cuvette containing 2 mL of 0.2 μM of protein in 200 mM MOPS buffer pH 7 and 200 mM NaCl and measurements at 340 nm were recorded every 2 seconds. The reaction mixture was constantly stirred using a micro stir bar in the bottom of the cuvette.

The maximum iron storage capacity was determined by plotting the relative absorbance at 340 nm versus the calculated Fe(II)/protein molar ratio.

Kinetics of Fe(II) oxidation with O_2

To analyze the rate of iron oxidation by Dps WT and Dps F46G in the presence of O_2, 0.6 μM of protein in 200 mM MOPS buffer pH 7 and 200 mM NaCl was reacted with 192 Fe(II)/protein and O_2. Before the beginning of the assay, the sample solution was oxygenated inside the cuvette was oxygenated by exposing to molecular oxygen for 1 min. UV-Visible spectra between 250 and 800 nm were recorded every 30 min for 15 hours.

The kinetic data (Absorbance at 340 nm vs. Time) was further analyzed. The theoretical first order kinetic model proposed for Dps WT was adjusted to the experimental data using the Solver tool of Microsoft Excel and an apparent kinetic rate constant (k') was determined.

3.2.7 DNA binding assay

Electrophoretic Mobility Shift Assay

EMSA is a sensitive method for detection of protein-nucleic acid complexes *in vitro*. For this binding assay, samples of protein and nucleic acid are combined in a suitable buffer and the binding is allowed to occur. The resulting mixtures are then evaluated by electrophoresis under native conditions.

Generally, this assay is based on the observation that the electrophoretic mobility of a protein-nuclei acid complex is less than that of free nucleic acid. Thus, during electrophoresis the rate of DNA migration is shifted or retarded when bound to protein, resulting in discrete bands corresponding to protein-DNA complexes. EMSA is a qualitative technique, but it can also be used quantitatively to measure thermodynamic and kinetic parameters. [64,65]

To study the DNA binding ability of Dps from *P. nautica* and characterize the Dps-DNA interaction, an EMSA was carried out using different protein/DNA ratios.

The DNA binding assay was performed using a Dps variant, where a glutamine from the N-terminus was replaced by a glutamate (Dps Q14E), and the supercoiled plasmid DNA pUC19 (Figure 3.1.2.).

Supercoiled DNA pUC19 (15 nM) was incubated for 10 min at room temperature with Dps Q14E (between 0.21 and 7.5 μM) in 50 mM MOPS buffer (pH 7) and 50 mM NaCl in for a total volume of 10 μL. As control, samples where Dps Q14E was replaced by BSA (4.4 μM) and free plasmid DNA were also prepared and analyzed.

EMSA was performed in 1 % agarose gel in 1 x TAE buffer and run at 80 V at room temperature for 1 h 30 min. The results were visualized using SYBR Safe DNA gel stain, imaged with Safe Imager™ (Invitrogen) and photographed in a Gel Logic 100 Imaging System (Kodak).

Electrophoretic images evaluation

The electrophoretic images obtained were processed and analyzed (free DNA and DNA-protein complex bands) using ImageJ. [66] To analyze the relative DNA-protein complex formation, the fractional saturation of the complex formation was plotted as a function of protein concentration.

3.2.8 Site-directed mutagenesis

Site-directed mutagenesis is a technique used to modify template DNA by the controlled exchange of nucleotide(s) and deletion or insertion of DNA fragments(s). Synthetic oligonucleotide primers for mutagenesis must contain the desired mutation in both strand directions, forward and reverse, and also complement the desired target sequence on opposite strands of the plasmid. [67]

The desired mutation is usually placed in the middle of the primers with approximately 15 or more bases of correct sequence on both sides. Further, according to the standard conditions primers should have between 30 and 45 bases pairs with a melting temperature of at least 78 °C. Primers should also have a minimum GC content of 40 % and end with one or more C or G bases. [68]

The Dps variants, D9K, D11K, D9K/D11K and Q14K, were produced by site-directed mutagenesis using the NZYMutagenesis kit (NZYTech) following the manufacture's protocol. This kit is designed to introduce point mutations and delete or insert single or multiple nucleotides in a template double-stranded DNA sequence.

Oligonucleotides Primers

The oligonucleotide primers used to produce the point mutations were designed and analyzed for optimization with the software OligoAnalyzer. The primers were then synthesized and purified by STABVida (data sheets of the primers provided by STABVida in Appendix 8.3, Figures 8.1-8.4). The sequences of the primers are showed in Table 3.6 with the nucleotides coding for the mutations underlined.

Table 3.6 - Sequences of the primers used to obtain the mutations in Dps. The nucleotides coding for the mutations are underlined.

Dps Mutant	Oligonucleotide Primer Forward (FF)	Oligonucleotide Primer Reverse (RV)
D9K	5' – g ggc aag aat ttt att ggt ctc aag aca gac aaa acc cag aag c – 3'	5' – g ctt ctg ggt ttt gtc tgt ctt gag acc aat aaa att ctt gcc c – 3'
D11K	5' – att ggt ctc gac aca aag aaa acc cag aag ctg gc – 3'	5' – gc cag ctt ctg ggt ttt ctt tgt gtc gag acc aat – 3'
Q14K	5' – ggt ctc gac aca gac aaa acc aag aag ctg gca gat gca ctg – 3'	5' – cag tgc atc tgc cag ctt ctt ggt ttt gtc tgt gtc gag acc – 3'
D9K-D11K	5' – g ggc aag aat ttt att ggt ctc aag aca aag aaa acc cag aag c – 3'	5' – g ctt ctg ggt ttt ctt tgt ctt gag acc aat aaa att ctt gcc c – 3'

Polymerase Chain Reaction (PCR)

The Polymerase Chain Reaction (PCR) was used for DNA amplification in the mutagenesis experiments. This method is based on thermal cycles and on the ability of DNA polymerase to synthetize a new strand of DNA complementary to a DNA template. At the end of the PCR reaction, the specific DNA sequence will be accumulated in several copies. [69]

The reaction mixture prepared for the PCR was a combination of an appropriate buffer for the polymerase activity, a NZYProof DNA polymerase, a mixture of desoxyribonucleotides (dNTPs), the double-stranded DNA template (DNA fragment containing the gene of interest to be amplified, in this case, is the gene coding for Dps protein), a forward and a reverse primers.

The PCR mixtures and the cycling parameters used to produce the Dps variants are showed in Table 3.7 and 3.8, respectively. The PCR was performed with a thermocycler (Biometra, Invitrogen) and verified by agarose gel electrophoresis, followed by 1 h incubation with *DpnI* to hydrolyze the non-mutated template DNA. [68]

Table 3.7 - Composition of the PCR mixtures (50µL) used to produce each Dps variant.

Component	Volume (µL)			
	D9K	D11K	Q14K	D9K/D11K
Reaction Buffer	5	5	5	5
dNTP mix	1	1	1	1
dsDNA template	1.49	1.49	0.25	0.21
Oligonucleotide primer FF	0.64	0.96	0.87	0.59
Oligonucleotide primer RV	0.83	0.98	0.87	0.72
Milli-Q water	40.04	39.57	41.01	41.48
DNA polymerase	1	1	1	1

Table 3.8 – PCR conditions used to produce each Dps variant.

Segment	Cycles	Temperature (°C)	Time (min)
1	1	95	2
2	18	95	1
		60	1
		68	9
3	1	68	15

Cells transformation

After the hydrolysis, the PCR products were transformed into *E. coli* cells strain NZYStar. A 10 µL sample of the *Dpn* I treated DNA was transferred to 50 µL of NZYStar competent cells and the reactions were incubated on ice for 30 min. Then, it was performed the heat-shock of each transformation in a 42°C water bath for 40 s, followed by incubation on ice for 2 min. After this, 900 µL of pre-heated LB medium were added and the transformations were incubated for 60 min at 37°C and 200 rpm. Different volumes of transformed cells were plated (100, 150, 200 µL and the remaining reaction) in LB/Agar plates containing 100 µg/mL ampicillin and incubated overnight at 37 °C.

Plasmid isolation

Some of the colonies obtained were selected and isolation of plasmid DNA was performed using the NZYMiniprep kit (NZYTech). The DNA samples were sent to Eurofins for sequencing, which allowed the confirmation of the desired mutations in the DNA.

3.2.9 Protein crystallography

X-ray Crystallography

X-ray crystallography is the leading technique to determine high-resolution three-dimensional molecular structures at an atomic level. [70] This technique requires well-ordered crystals and is based on the interaction between X-ray photons and electrons of protein molecules in the crystal. [71]

To form crystals, protein molecules need to establish adequate crystal contacts to yield periodic crystal lattice structure.

A protein crystal is therefore a three-dimensional arrangement of regular repetitions. This regular and systematic molecular order defines a crystal lattice with a unit cell containing one or more asymmetric units that are related by crystallographic symmetry. The unit cell of a crystal can be composed either by atoms, small molecules or whole proteins and is defined by the cell axis a, b and c, and the angles α, β, γ. The asymmetric unit is the smallest unit of volume, which contains all the structural information.

The geometry and symmetry of the unit cell defines the space group of the crystal. For biological molecules there are 65 possible space groups, distributed in seven crystal systems (Appendix 8.4, Figure 8.5). The correct identification of the space group is essential for the determination of the protein crystal structure. [72]

The most common techniques for protein crystallization are the hanging and sitting-drop using vapor diffusion method (Figure 3.6, A). In this method, the protein solution is lead to a supersaturated state by the equilibration of a drop containing a mixture of protein solution against a reservoir solution (precipitant) in a closed environment. [73] Once the solubility limit of the protein is reached, the solution in the drop becomes supersaturated and under optimal crystallization conditions, nucleation process can occur followed by crystal growth (Figure 3.6, B). [74]

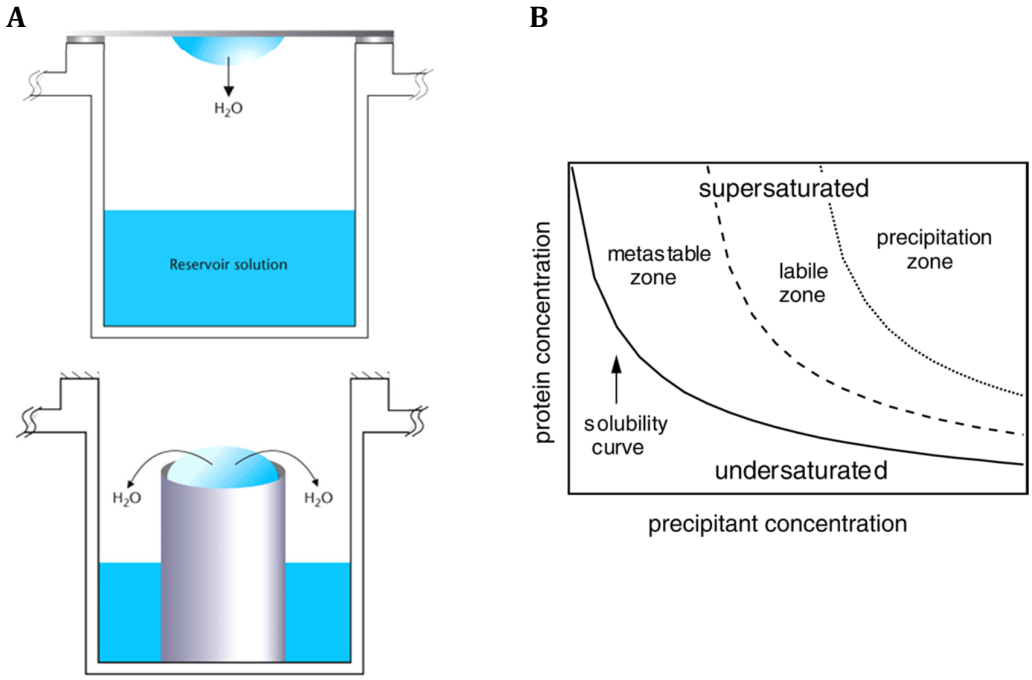

Figure 3.6 - Protein crystallization. A) Schematic representations of hanging (upper) and sitting-drop (lower) techniques in vapor diffusion setups. [73] B) Schematic phase diagram for protein crystallization showing the solubility of a protein in solution as a function of the concentration of precipitant present. Nucleation and crystal growth occur in the labile and the metastable zone, respectively. [74]

In a diffraction experiment, X-rays are scattered by the electrons of protein molecules. In diffraction conditions, the constructive interference of the scattered X-rays is observed with appropriate detectors in the form of diffraction spots with different intensities and inter-distances. This gives therefore a characteristic diffraction pattern at a certain crystal orientation with respect to the incoming X-rays. These spots are called reflections and the dimensions of the unit cell in the crystal (crystal lattice) are inversely proportional to the dimensions of the reciprocal lattice, that contains the reflections recorded by the detector.

In the crystal (real space), the position of an atom in the unit cell is given by cartesian coordinates (x, y, z), while in the diffraction pattern (reciprocal space) the position of a reflection is given by the Miller indices (*h, k, l*). [72]

The diffraction patterns can be understood using Bragg's law (3.2), where n is an integer number, λ is the wavelength of the X-rays, d is the distance between the lattice planes identified by the Miller indices and θ is the angle between the planes and the incident X-ray beam (Figure 3.7). [75]

$$n\lambda = 2d_{hkl}\sin\theta \tag{3.2}$$

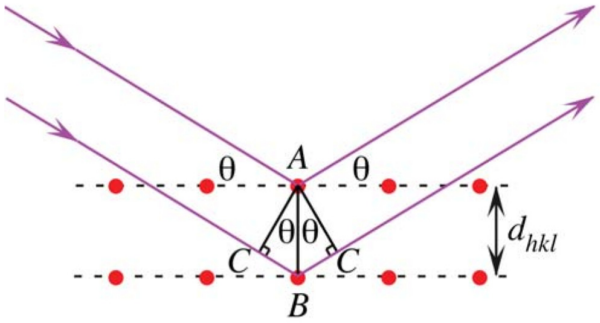

Figure 3.7 - Geometric representation of Bragg's law. In diffracting conditions, constructive interference occurs when the length $2d_{hkl}\sin\Theta$ is equal to an integer multiple of the wavelength of the incident X-ray beam. The scattered X-rays are then in phase and produce a reflection spot.[72]

Each reflection contains information from all atoms in the structure and is characterized by an amplitude and a phase. However, in the diffraction experiment the phase information is lost and only the reflection amplitudes can be obtained from the measured intensities.

To determine a protein structure, an electron density map with the distribution of the electrons in the crystal is calculated from the diffraction experiment. This is achieved by Fourier transformation of the so-called structure factors for all the Miller indices, F_{hkl}. [76]

Since the Fourier transform is a reversible operation, the electron density function ρ (*x, y, z*) can be described as a function of the structure factors for every atom position (*x, y, z*) in the real space (3.3). In the electron density function, (*x, y, z*), the atomic coordinates of the unit cell, V corresponds to the volume of the unit cell, $|F_{hkl}|$ to the structure factor amplitude and α_{hkl} to the angle phase of each reflection.

$$\rho\,(x,y,z) = \frac{1}{V}\sum_{hkl}|F_{hkl}|e^{[-2\pi i\,(hx+ky+lz-\alpha_{hkl})]} \tag{3.3}$$

Although, the structure factor amplitude $|F_{hkl}|$ is proportional to the square root of the reflection intensities measured in the diffraction experiment (3.4), without the phase angles, the electron density map cannot be calculated directly (Figure 3.8). [75]

$$|F_{hkl}|^2 \propto I_{hkl} \quad (3.4)$$

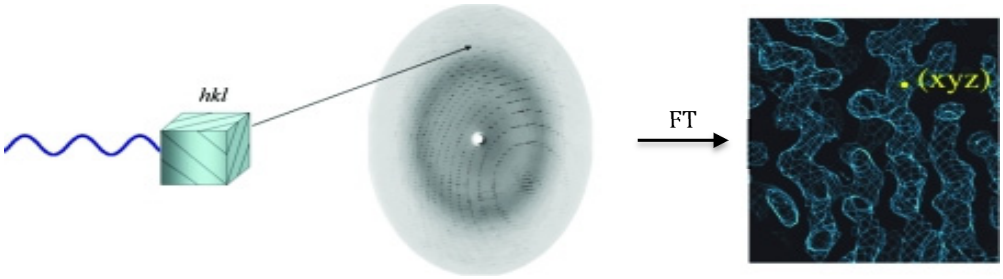

Figure 3.8 - X-ray diffraction experiment. The intensities of the X-rays diffracted by the electrons in a protein crystal are recorded on a detector and used to determine an electron density map. [77]

To overcome the phase problem and determine a protein three-dimensional structure, several methods can be used to obtain the phase information: molecular replacement (MR), single or multiple isomorphous replacement (SIR/MIR) and single or multiple-wavelength anomalous dispersion (SAD/MAD). [77]

MR is widely used when the structure of a homologous protein is already available. In order to obtain the unknown phase information, the model has to be correctly oriented and positioned into the unit cell of the unknown protein structure. Thereby, intermolecular distances are used to obtain a theoretical diffraction pattern for the existing structure that is similar to the experimental diffraction pattern of the unknown protein structure.

Once the phase problem of the new protein is solved, a model can be built into the electron density map and multiple refinement cycles, model re-fitting and validation have to be performed to generate a correct three-dimensional structure of a protein at atomic resolution. [75,77]

Anomalous X-ray Scattering

Anomalous X-ray scattering can be exploited in protein crystallography with a wavelength-tunable incident beam from synchrotron radiation sources[78]By selecting appropriate wavelengths, X-ray diffraction measurements can be performed to identify and determine the positions of distinct atoms with high precision, providing a definitive experimental solution for the crystallographic phase problem. [79]

Anomalous scattering occurs when the energy of the incident X-ray beam is in vicinity of an atom absorption edge. A fraction of the absorbed radiation is reemitted with an altered phase causing the breakage of Friedel's law seen in the measured intensities of the reflections. [72]

The anomalous scattering factor comprises three components: a normal scattering term f_0 that is dependent on the Bragg angle and two terms f' and f'' related by the Kramers-Kronig transformation that are dependent on the wavelength of the incident X-ray beam (3.5). These

two latter terms represent the anomalous scattering, corresponding to the real (dispersive) and imaginary (absorption) corrections to the scattering factor f_0. [77,80]

$$f(\theta,\lambda) = f_0(\theta) + f'(\lambda) + if''(\lambda) \quad (3.5)$$

Friedel pairs are the Bragg reflections (h, k, l) and (-h, -k, -l) related by inverse symmetry in the diffraction pattern. [72]

Friedel's law holds that $|F_{hkl}| = |F_{-h-k-l}|$. However, in the presence of anomalous scattering by atoms, Friedel's law breaks leading to distinct anomalous differences between the Friedel pairs, also designated as Bijvoet differences that can be used to locate these anomalous scatterers in the unit cell. [77,79]

The most frequent elements in protein structures are light elements such as carbon, hydrogen, nitrogen and oxygen and these do not contribute to anomalous scattering, because their absorption edges are not within the energy range of X-rays. In contrast, most of the heavy atoms have absorption edges within this range, allowing the collection of anomalous data with higher intensities. [72]

For heavy atoms, the real and imaginary components of the anomalous scattering factors can be estimated through the theoretical values calculated by Cromer and Liberman (Figure 3.9). However, in practice, the predicted values are not precise because the scattering factors depend not only on the element but also on coordination environment and oxidation state. [71] Consequently, an experimental evaluation is essential before data collection. [79,80] Fluorescence scans are directly measured from protein crystals to identify the maximum absorption (peak) and the inflection for subsequent data collection. [81]

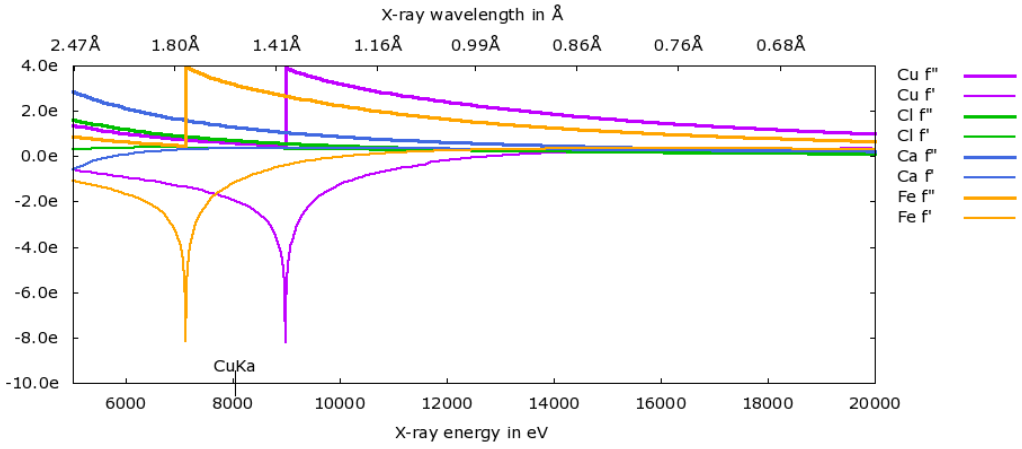

Figure 3.9 - Anomalous scattering factors, *f'* and f'' derived using the theoretical approximation developed by Cromer and Liberman, predicted for copper, chloride, calcium and iron atoms. [82]

In the present work, the anomalous diffraction promoted by iron and copper atoms was used to determine the positions of these metals within the three-dimensional structure of Dps

protein. Calcium and chloride atoms were present in the reservoir solution used to obtain the crystals and in the protein buffer.

Dps protein samples preparation

To solve the structure of *P. nautica* Dps crystallization experiments were set up in the absence of metals. The samples designated as Apoprotein Dps (Apo-Dps) were used in this work at 10 mg/mL under aerobic conditions.

To investigate the binding of iron and copper to Dps, the protein at 10 mg/mL was previously incubated with these metals ($FeSO_4$ and $CuSO_4$) to a final ratio of 12 metal ions per Dps molecule. Incubation was carried out for 1 hour at room temperature under anaerobic conditions for Dps incubated with 12 Fe(II)/Dps (12Fe-Dps) and under aerobic conditions for Dps incubated with 12 Cu(II)/Dps (12Cu-Dps).

Crystallization of Dps protein

To obtain protein crystals suitable for X-ray diffraction experiments, the sitting drop vapor diffusion method was used in all the crystallization trials.

Crystallization experiments were performed manually on 24-well Cryschem M plates (Hampton Research) or using the OryxNano Protein Crystallization Robot (Douglas Instruments) on 96-well MRC 2-drop plates (Molecular Dimensions).

Generally, in the crystallization experiments performed manually, the wells contained 300 µL of reservoir solution and the drops contained 1 µL of protein solution at 10 mg/mL and 1 µL of reservoir solution.

In the crystallization experiments performed using an automation system, 50 µL of reservoir solution were pipetted with the Phoenix\RE robot (Art Robbins Instruments) and the drops set with 0.3 µL of protein solution at 10 mg/mL and 0.3 µL of reservoir solution.

Crystallization plates were immediately sealed and stored at 20°C.

The crystallization process was monitored using a M165 C microscope (Leica) and a Discovery V20 microscope (Zeiss) in regular intervals. For the plates set up using the robot, the crystallization process was followed using the Minstrel HT imaging system together with the CrystalTrak software system (Rigaku).

Initially crystals were obtained using different crystallization screens, namely the Index screen (Hampton Research), the Morpheus screen (Molecular Dimensions) and the Footprint I-IV screens (Stura & Hermann).

To improve the diffraction quality of the crystals, fine screens, additive screens and micro-seeding experiments were performed. The fine screens were designed to change the volume of the drops and the reservoir solution in the wells, as well as, the protein concentration and the temperature of crystallization.

With the Additive Screen HT (Hampton Research), 96 unique reagents were tested by adding 0.2 µL (10 % of total drop volume) of a reagent such as salt, detergent or a small organic molecule to the drops containing 1 µL of protein solution at 10 mg/mL and 1 µL of reservoir solution or 30 µL of an additive (only alcohols) to the wells with 270 µL of reservoir solution.

In micro-seeding, fragments of crushed crystals previously obtained, were added to a new drop to act as nuclei for crystal growth. Micro seeds were prepared from crystals of an initial hit condition and 0.1 µL of such micro-seeds (1:200) were added to the drops with 0.3 µL of protein solution at 10 mg/mL and 0.2 µL of reservoir solution. For the seeds preparation, the drop containing the selected crystals was removed with a pipette. Subsequently, the solution was transferred to an eppendorf tube containing a micro seed bead and filled up with reservoir solution to a volume of 50 µL. Micro-seed stocks were generated by ten repeated cycles of vortexing for 10 seconds and incubation on ice for 20 seconds. For the crystallization trials, micro-seeds were diluted 1:200 using the reservoir solution.

Finally optimal crystallization conditions used for X-ray diffraction data collection consisted of 1) 10 % (w/v) polyethylene glycol (PEG) 4000, 20 % (v/v) glycerol, 0.03 M halogens (NaF, NaBr, NaI) and 0.1 M MES/Imidazole buffer with pH 6.5 and 2) 26 % (v/v) PEG 400, 0.2 M calcium acetate ($Ca(OAc)_2$) and 0.1 M HEPES buffer with pH 7.5.

Cryo protection and X-ray diffraction experiments

Crystals suitable for X-ray experiments grown overnight and were transferred to nylon loops according to their size. In order to reduce radiation damage of the crystals by the X-ray beam, crystals were flash-frozen in liquid nitrogen and irradiated with X-rays in a gas stream of liquid nitrogen (100 K) during the measurement.

To avoid formation of ice crystals during freezing, cryoprotective conditions are needed. For some crystals, 26% (v/v) PEG 400 was used as cryoprotectant, whereas for other crystals the cryoprotectant used was 10% (w/v) PEG 4000 and 20% (v/v) glycerol.

The diffraction quality of the crystals and the improvements in the crystallization conditions were evaluated using an in-house diffractometer set to a wavelength of 1.5418 Å produced by a rotating copper anode X-ray generator MicroMax-007 HF (Rigaku) combined with a Saturn944+ CCD detector (Rigaku) or a mar345 image plate detector (MAR reasearch). For data collection in-house, an exposure time of 420 s was selected and an oscillation range of 0.5 ° per image was applied over a total range of 180 °.

One dataset of Apo-Dps was collected in-house using the MAR345 image plate detector, while the other datasets were collected using synchrotron radiation at the beamline ID23-1 at the European Synchrotron Radiation Facility (ESRF).

The strategy adopted for data collection at the ESRF consisted on the collection of 1440 images with an oscillation range of 0.25° per image. For some measurements the kappa-based goniometer was used to change the orientation of the crystal, allowing the collection of distinct data from the same crystal. For the anomalous data collection, fluorescence scans were

previously recorded to determine the correct X-ray energies of the absorption edge and the inflection point of the iron and copper elements.

Several datasets at element's absorption edge, inflection and high energy remote (1 Å) were collected for the protein structures determination and identification of metal positions.

Structure determination and refinement

The diffraction data collected were indexed and integrated with XDS [83] and the scaling and merging were carried out with Aimless from the CCP4 software suite (Collaborative Computational Project Number 4) [84]. During these processes, images were excluded considering the scaling factors and resolution cut-offs were applied based on the signal-to-noise ratio ($I/\sigma(I)$) and the correlation coefficient between random half datasets ($CC_{1/2}$). [85]

For the dataset collected in-house, molecular replacement was carried out to obtain phase information using MOLREP from the CCP4 [84]. The initial model used was the Dps from *E. coli* (PDB code: 1 DPS) [31]. For datasets collected at the ESRF, the phase problem was solved by directly refining the new datasets against the structure obtained by molecular replacement.

Model building was performed using the program COOT [87] and refinement was carried out using PHENIX [86] and REFMAC5 from the CCP4 [84]. Furthermore, the obtained structures were improved with cycles of refinement using non-crystallographic symmetry (NCS) restraints.

To assess the model quality, structure validation was performed using COOT [87] and MOLPROBITY [88].

All protein structures presented in this work were illustrated and compared using PyMOL [89].

4 Results

4.1 Protein expression and purification

4.1.1 Dps WT expression and purification

Dps WT expression in *E. coli* BL21 (DE3) cells was performed according to the conditions described in the protein expression section in the materials and methods chapter (3.2.2). After cellular growth, cells were harvested by centrifugation and an average of 3.68 g cells/L culture medium (wet weight) was obtained. The pellet containing the Dps WT protein was then resuspended in 10 mM Tris-HCl pH 7.6 and the cellular extract was disrupted following the procedure described in the previous chapter.

Dps WT expression and fractions after disruption and centrifugation were analyzed through SDS-PAGE electrophoresis (Figure 4.1).

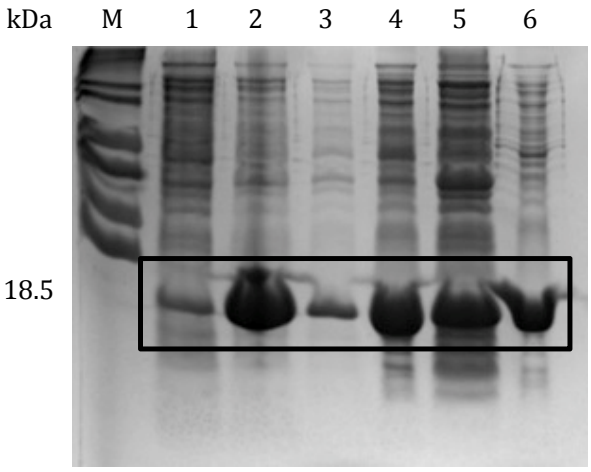

Figure 4.1 – Dps WT expression in *E. coli* BL21(DE3) cells was assessed by SDS-PAGE (12.5 % acrylamide, 80-120 V, 1 h 30 min). The gel was stained with Coomassie Brilliant Blue.Lanes: M – LMW Standard; 1 – Total cell content before induction; 2 – Total cell content after 3 hours of induction with 0.5 mM IPTG; 3 - Pellet after low-speed centrifugation; 4 – Supernatant low-speed centrifugation; 5 – Pellet after ultracentrifugation; 6 – Supernatant after ultracentrifugation. The black box highlights the bands corresponding to the expression of Dps WT.

The observation of the electrophoretic profile of Dps WT expression in Figure 4.1 reveals an intense band corresponding to the fraction containing Dps WT protein (bands highlighted in the black box). Despite the electrophoretic profile observed for the LMW marker does not correspond to the expected, as showed in the materials and methods chapter (3.1.5), the electrophoretic profile of Dps WT expression was already known and the bands with higher intensity correspond cellular extract that contain this protein. As can be observed in the gel, the

ultracentrifugation step had relatively low separation efficiency of the soluble fraction, containing Dps WT protein, from the membrane fraction. A significantly amount of the expressed Dps WT remained in the pellet instead of staying in the supernatant as expected.

The fraction containing the Dps WT protein collected after ultracentrifugation was then dialyzed and purified as described in the protein purification section in the materials and methods chapter (3.2.3).

For Dps WT purification three purification steps were performed to make sure that the protein was pure to be used in the crystallization experiments and functional assays. For the first step of purification a weak anionic exchange column, DEAE, was used. The protein was eluted using a discontinuous linear gradient of 10 mM Tris-HCl pH 7.6 and 500 mM NaCl. The elution profile of this purification step of Dps WT is represented in Figure 4.2.

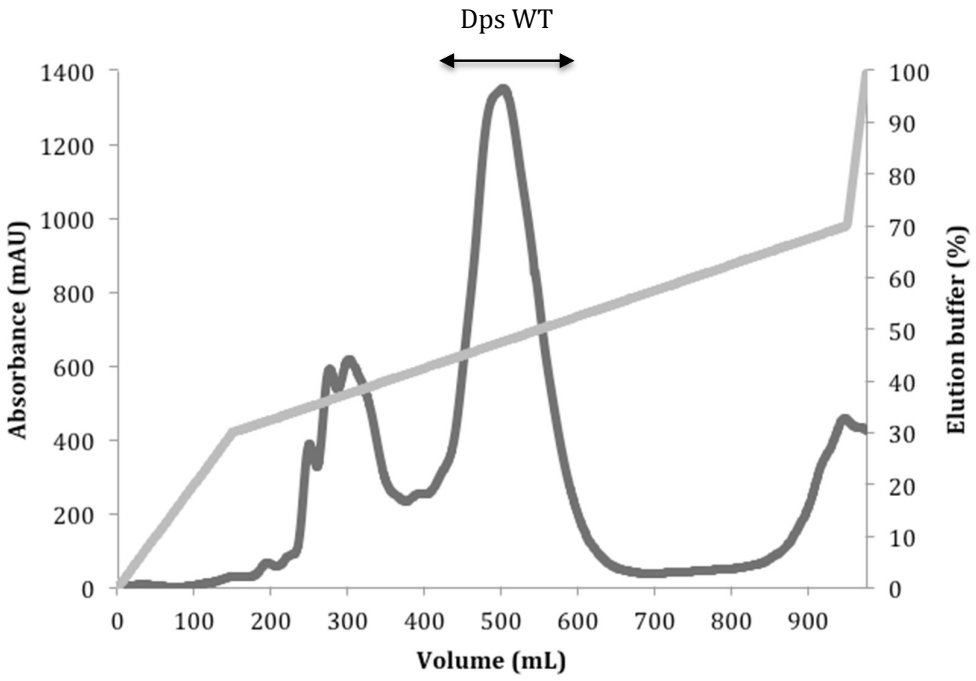

Figure 4.2 – Elution profile of DEAE ionic exchange chromatography used in Dps WT purification. A discontinuous linear gradient using the elution buffer 10 mM Tris-HCL pH 7.6 and 500 mM NaCl at a flow rate of 5 mL/min was applied for protein elution. 12 mL fractions were collected. The dark grey line corresponds to the Dps WT elution and the light gray line represents the elution buffer gradient. The black arrow indicates the fraction containing Dps WT protein.

According to the elution profile, Dps WT was eluted between 210 mM to 260 mM of the elution buffer 10 mM Tris-HCl pH 7.6 and 500 mM Nacl(i.e., from 42 % to 52 %). SDS-PAGE electrophoresis was then used to assess the purity of the collected fractions. The most pure fractions were pooled and the resulting fraction SDS-PAGE profile is showed in Figure 4.5.

The purification of Dps WT was followed by a second step of ionic exchange chromatography, where a strong anion exchanger column, Resource Q, was used. The elution profile of the second purification step of Dps WT is presented in Figure 4.3.

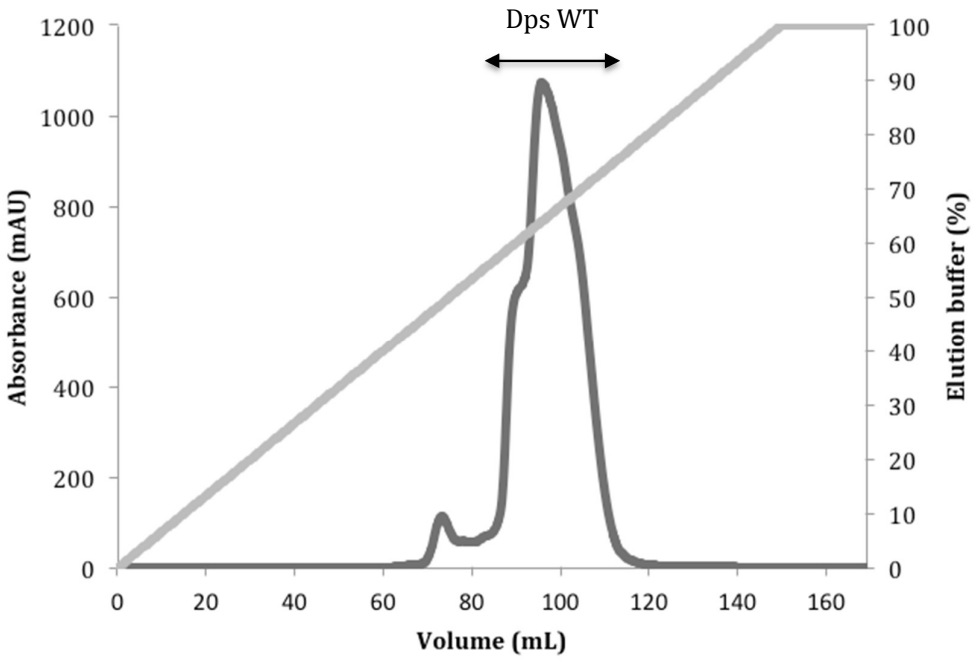

Figure 4.3 – Elution profile of Resource Q ionic exchange chromatography used in Dps WT purification. A continuous linear gradient using the elution buffer 10 mM Tris-HCL pH 7.6 and 500 mM NaCl at a flow rate of 4 mL/min was applied for protein elution. 4 mL fractions were collected. The dark grey line corresponds to the Dps WT elution and the light gray line represents the elution buffer gradient. The black arrow indicates the fraction containing Dps WT protein.

In the second step of purification, a continuous linear gradient of 10 mM Tris-HCl pH 7.6 and 500 mM was used to elute the Dps WT, which occurred between 280 mM and 375 mM of 10 mM Tris-HCl pH 7.6 and 500 mM NaCl (i.e., from 56 % and 75 % of elution buffer). Such as for the latest purification step, SDS-PAGE electrophoresis was also used to evaluate the purity of the collected fractions. The fractions with higher purity were pooled and the electrophoretic profile of the resulting fraction is showed in Figure 4.5.

As last step of purification, a size exclusion chromatography using a Superdex 200 column was used. The protein was eluted with 10 mM Tris-HCl pH 7.6 and 500 mM NaCl and the elution profile is represented in Figure 4.4.

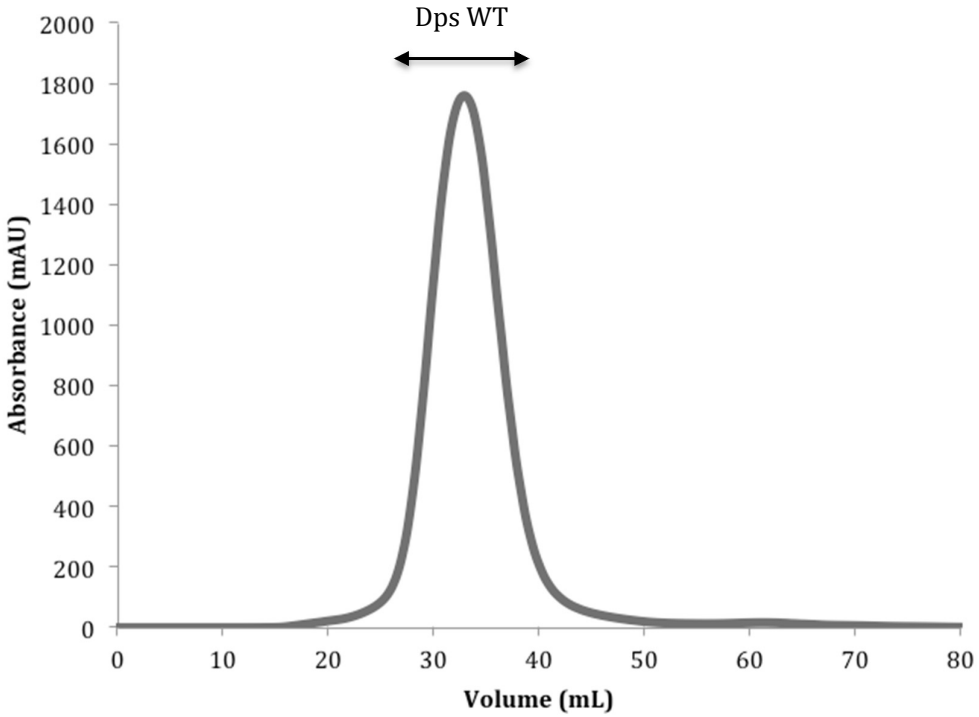

Figure 4.4 – Elution profile of Superdex 200 size exclusion chromatography used in Dps WT purification. The buffer used in this step 10 mM Tris-HCL pH 7.6 and 500 mM NaCl at a flow rate of 1.5 mL/min. 2 mL fractions were collected. The dark grey line corresponds to the Dps WT elution. The black arrow indicates the fraction containing Dps WT protein.

The elution profile of Dps WT purification (Figure 4.4) showed a high-intensity elution peak correspondent to the elution of this protein, which was confirmed by the SDS-PAGE analysis of the collected fractions. The purity of the fractions can be observed in the gel showed in Figure 4.5.

The electrophoretic profile of the Dps WT through the purification steps is showed in an acrylamide gel presented in Figure 4.5.

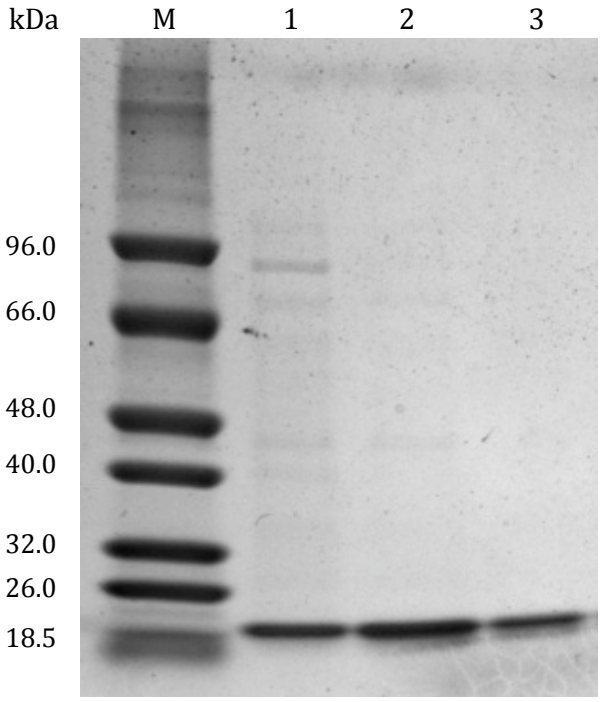

Figure 4.5 – SDS-PAGE analysis of the fractions collected from the different purification steps of Dps WT (12.5 % acrylamide, 80-120 V, 1 h 30 min). The gel was stained with Coomassie Brilliant Blue. A) Lanes: M – LMW; 1 – Fraction of Dps WT protein after DEAE; 2- Fraction of Dps WT protein after Resource Q; 3 – Fraction of Dps WT protein after Superdex 200.

As can be seen in Figure 4.5 the purification steps performed revealed to be efficient for the purification of Dps WT. The last lane showed a single band with approximately 18 kDa that corresponds to pure Dps WT fraction and a final yield of pure protein of about 24.2 mg/L was obtained. The final fraction was tested negative for catalase activity. Pure Dps WT was then used to iron uptake assays and for the crystallization experiments.

4.1.2 Dps F46G expression tests

In order to find the best expression conditions for Dps F46G expression in *E. coli* BL21(DE3) cells, test expressions were performed. The culture media (LB and 2xYT) as well as the concentration of the IPTG (0.1, 0.5 and 1 mM), the optical density OD_{600} for induction (0.5 or 2) and the incubation time after induction (3 or 16 h) were the parameters tested. Subsequently, after normalizing the cellular samples collected throughout the expression test expression, their electrophoretic profile was assessed by SDS-PAGE electrophoresis, as can be observed in the Figure 4.6.

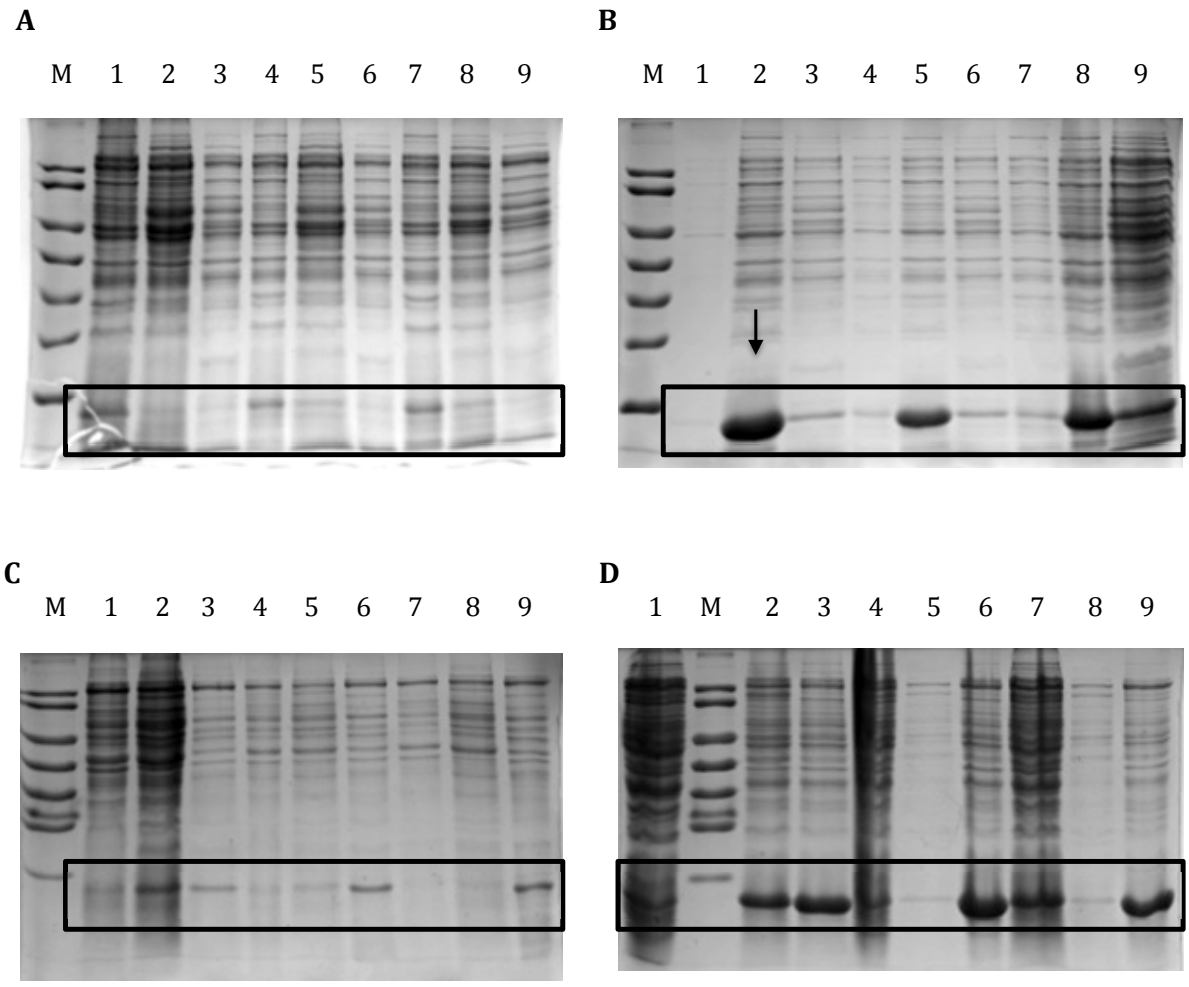

Figure 4.6 – Dps F46G expression tests in *E. coli* BL21(DE3) cells was assessed by SDS-PAGE (12.5 % acrylamide). A) LB medium and induction with OD_{600} of 0.5. B) 2xYT medium and induction with OD_{600} of 0.5. C) LB medium and induction with OD_{600} of 2. D) 2xYT medium and induction with OD_{600} of 1. Lanes: M – LMW, 1, 4 and 7 – Total cell content before induction; 2 - Total cell content after 3 hours of induction with 0.1 mM IPTG; 3 - Total cell content after 3 hours of induction with 0.1 mM IPTG; 5- Total cell content after 3 hours of induction with 0.5 mM IPTG; 6 - Total cell content after 16 hours of induction with 0.5 mM IPTG; 8 - Total cell content after 3 hours of induction with 1 mM IPTG; 9 - Total cell content after 16 hours of induction with 1 mM IPTG. The black box highlights the bands corresponding to Dps F46G. The black arrow indicates the expression conditions selected for Dps F46G expression.

By analyzing the gels presented in Figure 4.6 where the black boxes highlight the bands correspondent to the Dps F46G, which has an approximately molecular weight of 18 kDa, it is possible to determine the best expression conditions for the expression of this protein in *E. coli* BL21(DE3) cells. The LB medium does not have a high efficiency in the expression of Dps F46G, in contrast to the expression of Dps WT. Thus, for the large-scale expression of this Dps variant the following conditions were selected: 2xYT medium, induction at an OD_{600} of 0.5 with 0.1 mM of IPTG and cellular growth after induction of 3 hours.

The electrophoretic profile of the conditions selected for Dps F46G expression is present in the lane with the black arrow (gel B, Figure 4.6). After achieving the optimal

conditions for Dps F46G expression, this protein was expressed and purified for the iron uptake assays.

4.1.3 Dps F46G expression and purification

Dps F46G expression in *E. coli* BL21(DE3) cells was performed following the protocol described in the protein expression section in the materials and methods chapter (3.2.2). After cellular growth, cells were harvested by centrifugation and an average of 4.85 g cells/L culture medium (wet weight) was obtained. The pellet containing the Dps F46G protein was then resuspended in 10 mM Tris-HCl pH 7.6 and the cellular extract was disrupted as described in the previous chapter. Dps F46G expression and fractions after disruption and centrifugation were assessed through SDS-PAGE electrophoresis (Figure 4.7).

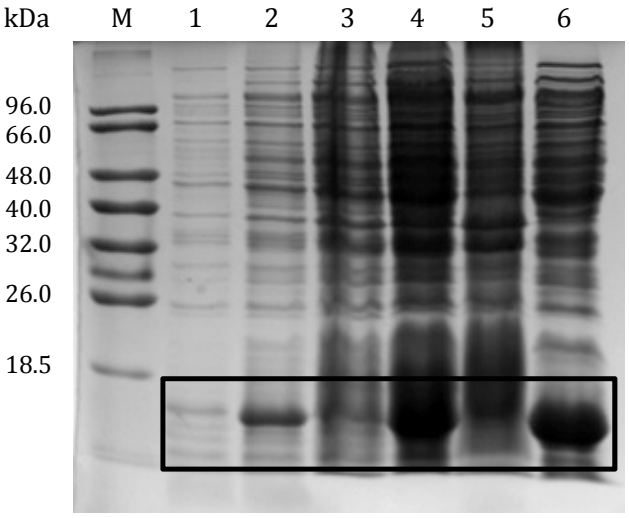

Figure 4.7 – Dps F46G expression in *E. coli* BL21(DE3) cells was assessed by SDS-PAGE (12.5 % acrylamide, 80-120 V, 1 h 30 min). The gel was stained with Coomassie Brilliant Blue.Lanes: M – LMW Standard; 1 – Total cell content before induction; 2 – Total cell content after 3 hours of induction with 0.5 mM IPTG; 3 - Pellet after low-speed centrifugation; 4 – Supernatant after low-speed centrifugation; 5 – Pellet after ultracentrifugation; 6 – Supernatant after ultracentrifugation. The black box highlights the Dps F46G protein bands.

The Figure 4.1 shows the electrophoretic profile of Dps WT expression, where the observed intense band correspondents to the fraction containing Dps F46G protein (bands highlighted in the black box), with an approximately molecular weight of 18 kDa. As can be observed in the gel, the ultracentrifugation step had relatively high separation efficiency of the soluble fraction, containing Dps F46G protein, since the electrophoretic profile of the supernatant after ultracentrifugation has a band with high intensity at about 18 kDa, in contrast to the electrophoretic profile of the pellet. The fraction containing the Dps F46G protein

collected after ultracentrifugation was then dialyzed and purified as described in the protein purification section in the materials and methods chapter (3.2.3).

For Dps F46G purification only two purification steps were performed. For the first step of purification a DEAE column was used. The protein was eluted using a discontinuous linear gradient of 10 mM Tris-HCl pH 7.6 and 500 mM NaCl and the elution profile of Dps F46G is showed in Figure 4.8.

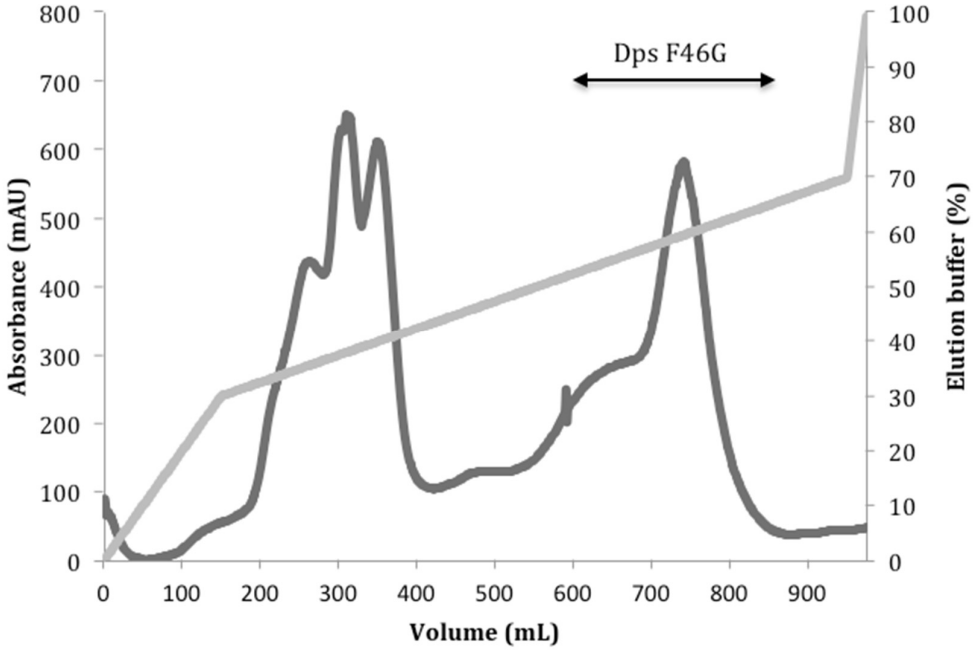

Figure 4.8 – Elution profile of DEAE ionic exchange chromatography used in Dps F46G purification. A discontinuous linear gradient using the elution buffer 10 mM Tris-HCL pH 7.6 and 500 mM NaCl at a flow rate of 5 mL/min was applied for protein elution. 12 mL fractions were collected. The dark grey line corresponds to the Dps F46G elution profile and the light gray line represents the elution buffer gradient. The black arrow indicates the fraction containing Dps F46G protein.

Dps F46G was eluted between 260 mM to 315 mM of 10 mM Tris-HCl pH 7.6 and 500 mM NaCl (from 52 % to 63 %). From observation of the Figure 4.8, it can be assumed that some of the contaminants were eliminated at the first purification step. To assess the purity of the collected fractions, SDS-PAGE was used and in Figure 4,10 A is showed the electrophoretic profile of the collected fraction that corresponds to the maximum of the elution peak.

The second step of purification was done using a size exclusion chromatography to isolate Dps F46G from the remaining proteins with the elution buffer of 10 mM Tris-HCl pH 7.6 and 500 mM NaCl. The elution profile of this purification step with a Superdex 200 column is presented in Figure 4.9.

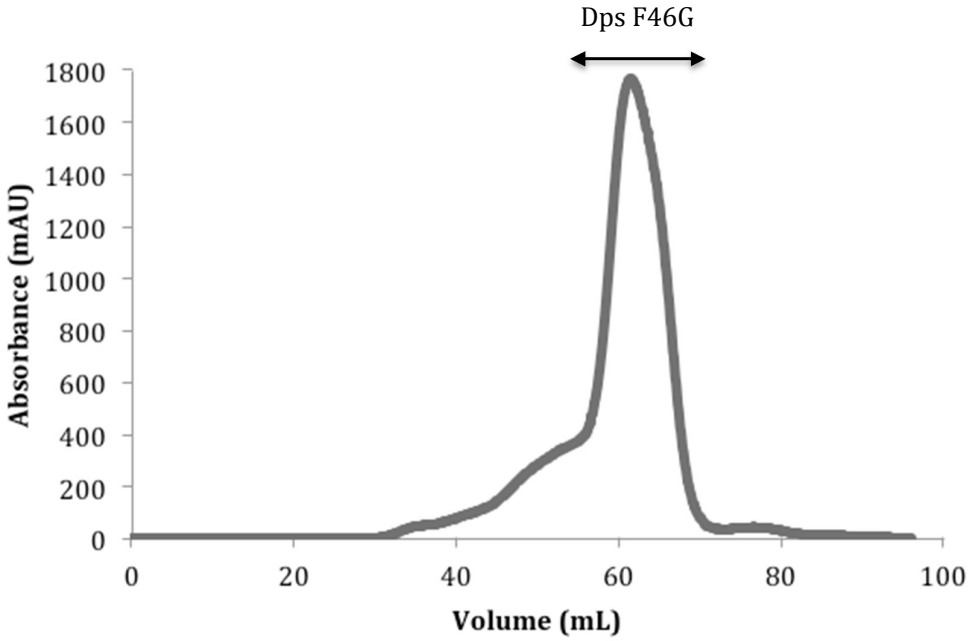

Figure 4.9 – Elution profile of Superdex 200 size exclusion chromatography used in Dps F46G purification. The protein was eluted using the elution buffer 10 mM Tris-HCL pH 7.6 and 500 mM NaCl at a flow rate of 1.5 mL/min. 2 mL fractions were collected. The dark grey line corresponds to the Dps F46G elution. The black arrow indicates the fraction containing Dps F46G protein.

The high-intensity elution peak observed in Figure 4.9 corresponds to the elution of Dps F46G, which could be confirmed by SDS-PAGE electrophoresis.

The purity of the fractions collected throughout the purifications was analyzed by SDS-PAGE electrophoresis, showed in Figure 4.10.

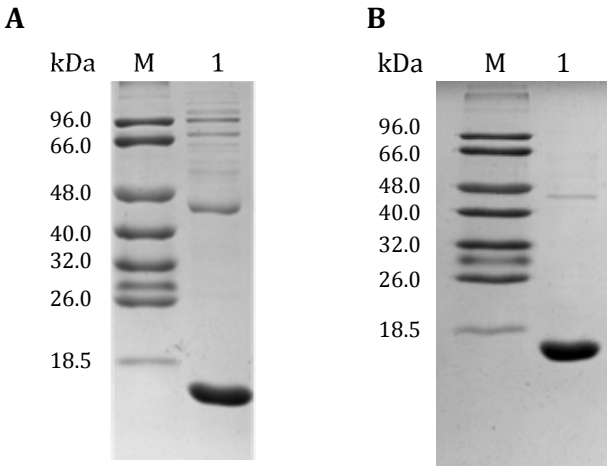

Figure 4.10 – SDS-PAGE analysis of the fractions collected from the different purification steps of Dps F46G purification by SDS-PAGE (12.5 % acrylamide, 80-120 V, 1 h 30 min). The gel was stained with Coomassie Brilliant Blue. A) Lanes: M – LMW; 1 – Fraction of Dps F46G from the elution peak of the DEAE; B) Lanes: M – LMW; 1 – Fraction of Dps F46G protein after Superdex.

The SDS-PAGE gels showed that most of the contaminants were removed with the second purification step and the protein sample collected after the size exclusion chromatography is pure. A final pure protein yield of 19.1 mg/L was obtained. Such as for Dps WT, the test for catalase activity was also applied to the sample of Dps F46G and the result was negative. Dps F46G was then utilized for iron uptake assays.

4.2 Iron uptake assays

To study the iron incorporation and storage capacity by Dps proteins, Dps WT and Dps F46G from *P. nautica* were used for iron uptake assays. In order to compare the behavior of Dps WT versus Dps F46G, the same set of experiments (in similar experimental conditions) were performed. The results obtained with iron uptake assays performed by using H_2O_2 and O_2 as co-substrate, will help to understand the mechanism or iron oxidation and incorporation.

The proteins, Dps WT and Dps F46G, were expressed and purified in the apo-form, which was previously confirmed by determination of the iron content by Inductively Coupled Plasma Atomic Emission Spectroscopy (ICP-AES). [55] The variant of Dps F46G was produced in order to study the role of phenylalanine 46 (Phe46) in iron incorporation mechanism, due to its location near to the FOC and to the presence of an aromatic ring, as can been seen in Figure 4.11. Phenylalanine 46 was replaced by a glycine, which allows to observe the influence of the aromatic ring, since both amino acids are hydrophobic and the charge of its side-chain is neutral at pH 7.

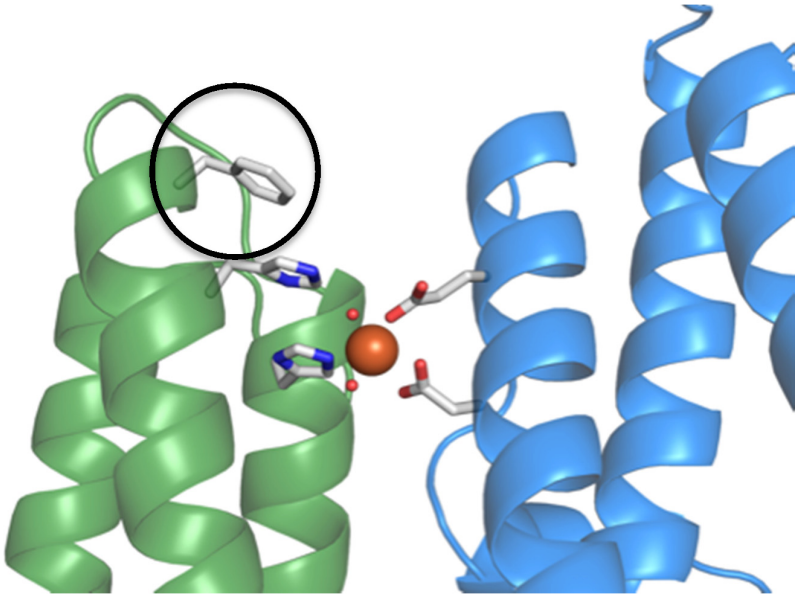

Figure 4.11 – Structure representative of a dimer of Dps protein highlighting the FOC with iron bound. The side-chains of the protein residues and the waters coordinating the iron are showed as sticks as well as the phenylalanine 46. Phenylalanine 46 is highlighted with a black circle.

As can be seen in Figure 4.11, phenylalanine 46 is located in the proximity of the FOC and its aromatic ring is orientated to the interior of two symmetry-related monomers. By observing its position and orientation relatively to the histidine residues (histidine 50 and histidine 38, where the last one is involved in the iron coordination), phenylalanine can be involved in π-stacking interactions between neighboring aromatic rings, stabilizing their position within the protein structure. On the other hand, the aromatic ring of Phe46 can be involved in electron transfer processes necessary for iron oxidation in the FOC.

Therefore, the replacement of residue 46 by an amino acid without an aromatic ring as its side-chain can affect the iron incorporation in Dps protein by two different ways. It can destabilize the position and orientation of both histidine residues, affecting the iron coordination in the FOC or it can influence the iron oxidation process.

4.2.1 Iron uptake assays using H_2O_2 as co-substrate

Iron uptake assays using H_2O_2 as co-substrate for iron oxidation reaction were monitored by UV-Vis spectroscopy at 340 nm. The assays were performed in 200 mM MOPS pH 7 and 200 mM NaCl as described in the iron uptake assays section in the materials and methods chapter (3.2.6). This method allows studying the maximum of iron storage capacity of Dps proteins through the successive additions 48 Fe(II)/molecule and an excess of H_2O_2. As the formation of iron core using H_2O_2 as co-substrate was previously determinate to be a very fast process [36], measures were recorded every 2 seconds.

To analyze the iron storage capacity by these Dps WT and Dps F46G, the relative absorbance measured at 340 nm was plotted as a function of the molar ratio Fe(II)/Dps molar, as showed n Figure 4.12. This plot allows observing the variation introduced by every addition of Fe(II) and H_2O_2.

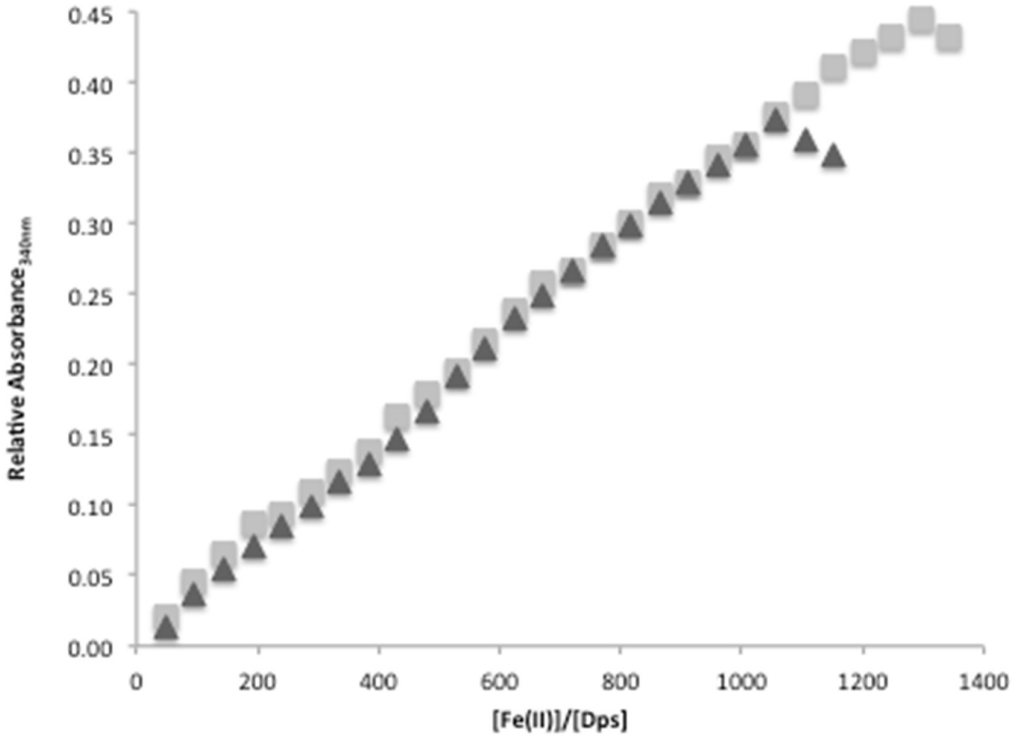

Figure 4.12 - Dps WT and Dps F46G iron loading experiment in the presence of an excess of H_2O_2. Reaction of 0.2 μM Dps with Fe(II) ions and H_2O_2 in 200 mM MOPS pH 7 and 200 mM NaCl. Each point represents the ΣΔAbsorbance measured at 340 nm after an addition of 48 Fe(II)/Dps and an excess of H_2O_2.

Under the experimental conditions tested, the iron appears to be incorporated by Apo-Dps until its inner cavity reaches its maximum, which can be seen by the maximum of the absorbance at 340 nm (Figure 4.12.). Both Dps WT and Dps F46G have the ability to incorporate iron atoms, as can be observed by the increase of the absorbance at 340 nm. The decrease that is later observed in the absorbance indicated that iron is no longer incorporated by Dps protein and ferric iron precipitates in solution (Figure 4.13 C).

According to the results obtained, the Dps proteins used in this study were able to incorporate different amounts of iron. For Dps WT an iron incorporation ratio of about 1300 Fe(II) per molecule was verified, whereas for Dps F46G this was about 1000 Fe(II) per molecule. Nevertheless, this difference cannot be considered significant, since more data would be necessary to proper evaluate its significance.

The amounts of iron incorporated observed in these experiments are not comparable with the theoretical maximum amount of iron atoms incorporated described in literature, where about 500 iron atoms can be accommodated in the inner cavity of Dps protein as hydrous ferric oxide mineral core. [24] This could be explained by a chemically different nature of the iron cores. As previously mentioned, the core can have a variable amount of phosphate, which can influence the space occupied by the molecules stored in the central cavity. A different hypothesis may be related with a certain flexibility of Dps protein, where the assembling of its

monomers can create cavities with different sizes and therefore accommodate different amounts of iron atoms, according to the environment and the conditions of the protein.

The different phases of the iron uptake assays with hydrogen peroxide in solution can also be observed with the photographed pictures of the solution present in the cuvette, as showed in Figure 4.13.

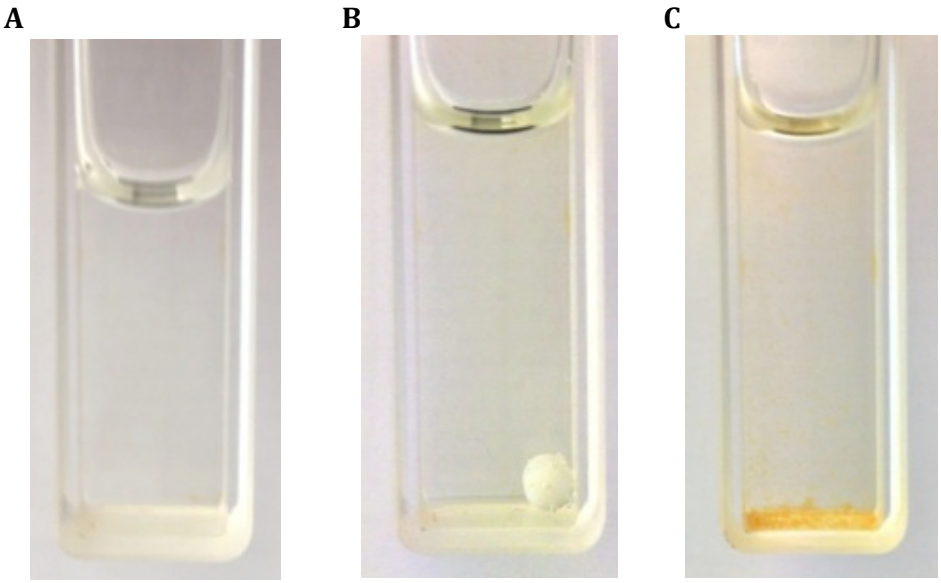

Figure 4.13 - Effect of Dps WT on the iron oxidation reaction in the presence of an excess of H_2O_2. The cuvettes are in 200 mM MOPS pH 7 and 200 mM NaCl and contain the 0.2 µM of Dps protein and different amounts of $FeCl_2$. A) Apo-Dps protein in solution. B) Dps protein with iron core. The solution is clear, meaning that the inner cavity is not saturated. C) Dps protein with iron core and an excess of iron. The excess of iron formed a yellow precipitate present in solution due to the saturation of the cavity of Dps.

Addition of iron atoms to Dps protein in solution and its oxidation and incorporation can be visualized by the color and the transparency of the solution present in the cuvette. In the beginning of the experiment, only Apo-Dps protein was present in the solution and no color is observed, since Dps does not absorb in the visible region of the spectrum (Figure 4.13 A). However, after some additions of Fe(II) and H_2O_2 to the solution, a yellow clear solution was observed in the cuvette, which is due to the iron oxidation and its incorporation inside the protein molecule (Figure 4.13 B). When the central cavity of these protein molecules reached a saturation, iron was no longer incorporated and precipitation occurred. Therefore, at the end of the experiment, a yellow precipitate was observed inside of the cuvette Figure 4.13, C).

The process above mentioned was observed either for Dps WT and Dps F46G, has both proteins have the ability to bind and incorporate iron atoms inside of its inner cavity despite the difference of iron atoms that can be loaded into the protein.

4.2.2 Kinetics of Fe(II) oxidation with O_2

According to the results aforementioned, there is no significant difference between Dps WT and Dps F46G relatively to the iron incorporation and its storage in the central cavity, when H_2O_2 is used as co-substrate in iron oxidation reaction. However, the mutation of Phe46 may have some influence in the mechanism formation of the iron core. Therefore, O_2 was used as co-substrate to follow the formation of the iron core at 340 nm, since it is already known that the reaction with O_2 occurs at a slower rate than with H_2O_2. [36]

The kinetics of iron oxidation with O_2 in Dps WT and Dps F46 was monitored by UV-Visible spectroscopy and 192 Fe(II)/Dps molecule were added to the protein solution. The reaction was monitored for 15 hours by measuring the absorbance at 340 nm in 200 mM MOPS pH 7 and 200 mM NaCl, as previously described in the iron uptake assays section in the material and methods chapter (3.2.6). The progress curves of iron uptake by Apo-Dps WT and F46G from *P. nautica* upon addition of 192 Fe(II)/molecule are showed in Figure 4.14, which allows to follow the iron core formation and analyze its kinetic mechanism.

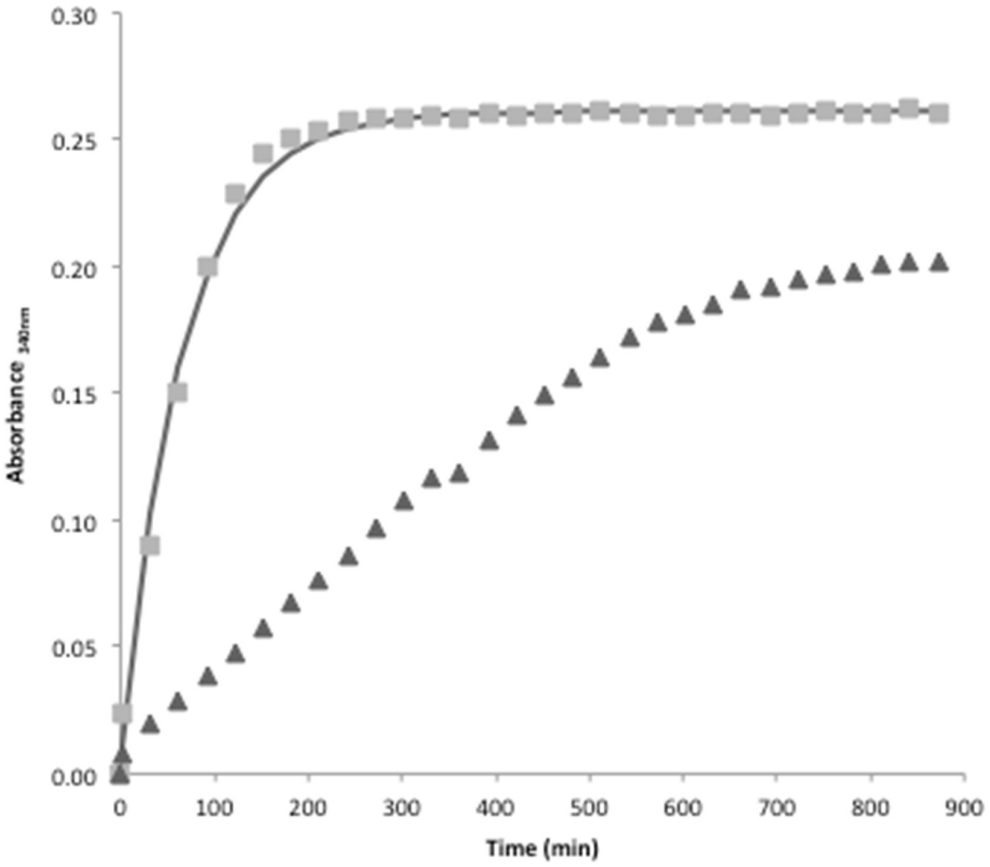

Figure 4.14 - Kinetics of Fe(II) oxidation by Dps WT and Dps F46G in the presence of O_2. Reaction of 0.6 µM Dps in 200 mM MOPS pH 7 and 200 mM NaCl with a molar ratio of 192 Fe(II)/Dps and saturation with O_2. The reaction was started at 2 min by addition of the $FeCl_2$ solution and monitored spectrophotometrically at 340 nm. Light grey squares - experimental data of Dps WT; Dark grey line - theoretical curve adjusted to the experimental data of Dps WT; Dark grey triangles - experimental data of Dps F46G.

The results obtained in these experimental conditions allowed only the adjustment of a theoretical curve to the experimental data of Dps WT with Solver, as can be seen in Figure 4.14. This theoretical curve can be used to calculate a mechanism model for the iron core formation in Dps WT. The best theoretical fit was obtained when a first order kinetic model was applied to the experimental data with a pseudo-first order rate constant (k') and the following reaction (4.1).

$$A + Fe^{2+} + O_2 \overset{k\prime}{\rightarrow} B \tag{4.1}$$

In this model A corresponds to the Apo-Dps protein in absence of an iron core, that does not absorb in the visible spectrum, and B corresponds to the Dps protein with an iron core that absorbs at 340 nm. As the formation of B is a slow process, its detection is possible with this technique. [36]

From the plot presented above (Figure 4.14) it can be assume that the model applied is a good fit for the experimental data of iron oxidation by Dps WT. Considering the model mentioned above, a first order kinetic equation (4.2) can be used to describe the formation of the iron core observed in the experimental results showed in Figure 414.

$$B = -A_0\, e^{-k\prime t} \tag{4.2}$$

With this equation and the theoretical curve applied to the experimental data is possible to calculate the apparent kinetic rate constant (k') for the iron core formation with O_2 for Dps WT, which was determined to be 0.015 min^{-1}.

As for the experimental data of Dps F46G a theoretical adjustment was not possible, it can be assumed that the iron core formation within this protein has a different mechanism.

By comparison of the curves obtained for the iron core formation at 340 nm (Figure 4.14) it is possible to observe that iron core formation is significantly slower with Dps F46G. Therefore, it is clear to say that phenylalanine 46 is involved in iron core formation within Dps protein and its absence decreases the rate at iron core formation occurs with O_2. However, with these results it not clear if Phe46 affects the formation of the iron core due the stabilization of the aromatic rings of due to the electron transfer processes.

4.3 DNA binding assay

Some Dps proteins have the ability to bind DNA without an apparent sequence specificity. However, the mechanism of the binding between DNA molecules and Dps is still not fully understood.

In order to investigate the DNA binding ability of Dps WT protein from *P. nautica*, EMSAs were performed. Previous EMSA experiments carried out in our group have showed the capacity of this protein to bind supercoiled plasmid DNA in 50 mM MOPS pH 7 and 50 mM NaCl, as can be seen in the agarose gel showed in Figure 4.15.

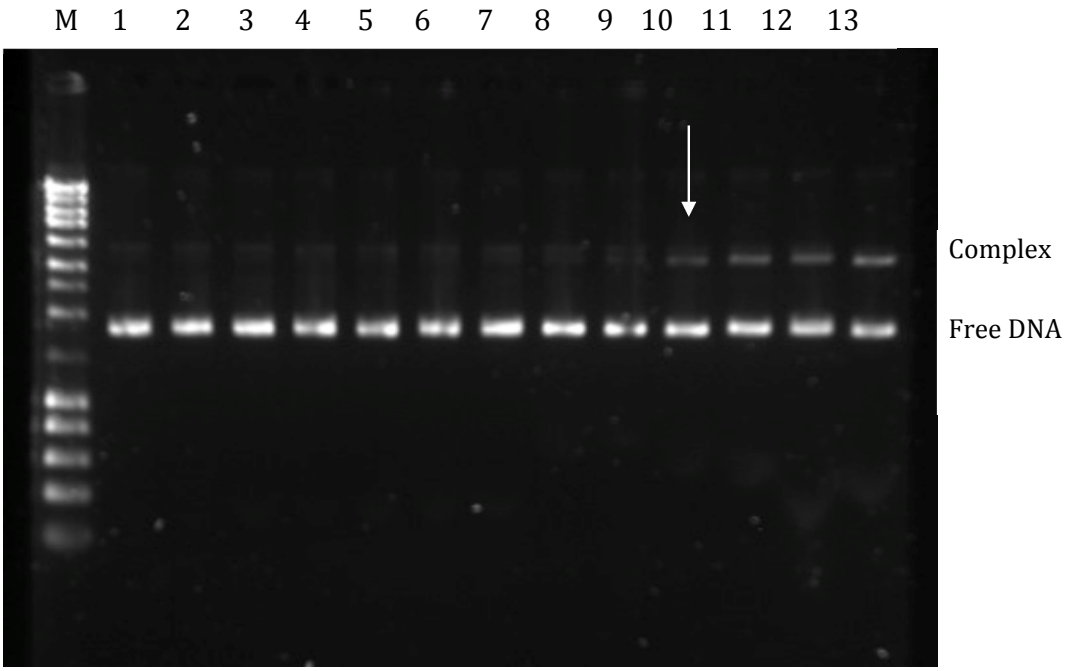

Figure 4.15 - Binding of Dps WT to supercoiled plasmid DNA pUC19 in 50 mM MOPS pH 7 and 50 mM NaCl tested by EMSA (1 % agarose gel, 80 V,1 h 30 min). The gel was stained with SYBRSafe. Lanes: M- NZYDNA Ladder III; 1 – pUC19 (15 nM); 2 – Binding reaction of BSA (4.4 μM) to pUC19 (15 nM); 3 to 13 – Binding reaction of Dps WT (0.21, 0.375, 0.75, 1.05, 1.5, 1.8, 2.7, 3.75, 4.5, 6.0, 7.5 μM) to pUC19 (15 nM). The white arrow indicates the protein/DNA molar ratio of 250. The free supercoiled DNA band (Free DNA) and the protein-DNA band (Complex) are indicated on the right.

Binding of Dps WT to supercoiled DNA generates larger DNA-protein complexes that migrate slower than free DNA, which can be seen in Figure 4.14 by the shifting of the band of free DNA with increasing concentrations of Dps WT.

It is clear that Dps is able to bind DNA since replacing this protein by 4.4 μM BSA (a protein that does not bind DNA) did not cause any mobility retardation of the plasmid DNA band. Further, by analyzing the agarose gel it can be seen that, in these experimental conditions, the apparent saturation of the complex formation was not achieved.

As mentioned before, it has been suggested that the binding of Dps to DNA is due to the presence of positively charged residues in the N-terminal regions that protrude to the outside of Dps molecule. Thus, in order to characterize this binding, a variant of Dps from *P. nautica*, where a glutamine from the N-terminus was replaced by a glutamate (Dps Q14E), was used to carry out EMSA experiments with supercoiled plasmid, pUC19. These experiments were carried out in 50 mM MOPS pH 7 and 50 mM NaCl, as described in the DNA binding assay section in the materials and methods chapter (3.2.7). At pH 7, glutamine has a neutral side-chain,

whereas glutamate is negatively charged. Therefore, the use of this variant to study the DNA binding ability of Dps allowed to observe the influence of the charge of residues from the N-terminus in the DNA binding.

The electrophoretic mobility of Dps Q14E incubated with supercoiled pUC19 can be observed in the agarose gel showed in Figure 4.15.

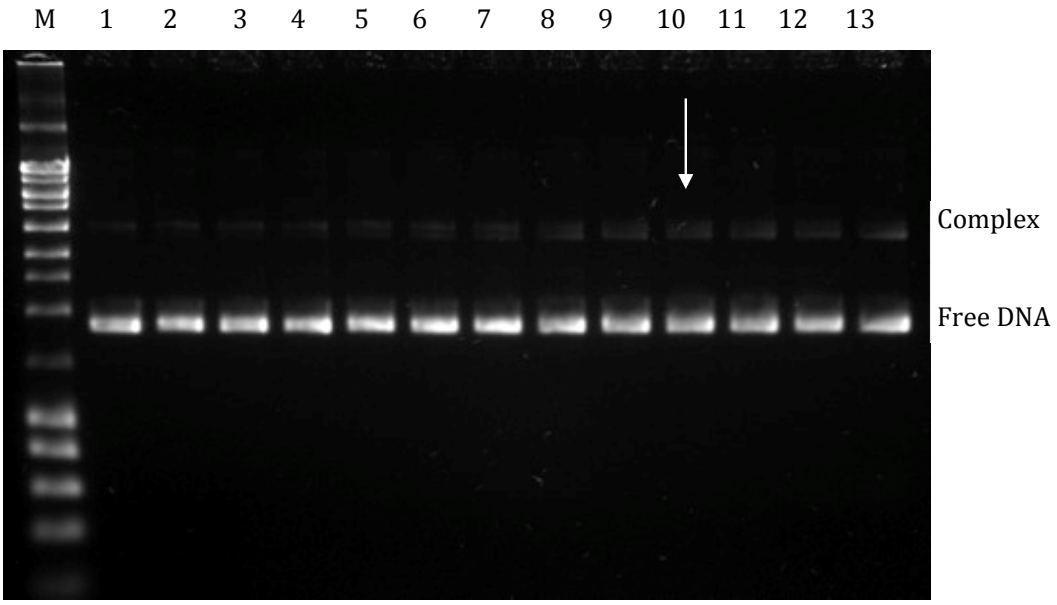

Figure 4.16 - Binding of Dps Q14E to supercoiled plasmid DNA pUC19 in 50 mM MOPS pH 7 and 50 mM NaCl tested by EMSA (1 % agarose gel, 80 V,1 h 30 min). The gel was stained with SYBRSafe. Lanes: M- NZYDNA Ladder III; 1 – pUC19 (15 nM); 2 – Binding reaction of BSA (4.4 μM) to pUC19 (15 nM); 3 to 13 – Binding reaction of Dps Q14E (0.21, 0.375, 0.75, 1.05, 1.5, 1.8, 2.7, 3.75, 4.5, 6.0, 7.5 μM) to pUC19 (15 nM). The white arrow indicates the protein/DNA molar ratio of 250. The free supercoiled DNA band (Free DNA) and the protein-DNA band (Complex) are indicated on the right.

The agarose gel presented on Figure 4.15 showed that, when Dps Q14E was incubated with supercoiled pUC19, it did not promote a significant retardation in the mobility of the free plasmid DNA band in comparison to Dps WT. This indicates that Dps Q14E was able to bind DNA, but with a significantly lower affinity. Thus, the presence of this single mutation in the N-terminus of Dps protein has the ability to influence the binding affinity of DNA molecules, which is consistent to what has been suggested for the DNA binding mechanism, regarding the presence of positively charged residues.

To determine the DNA-binding ability of Dps WT and Dps Q14E, the electrophoretic images were processed using ImageJ[66]. For densiometric quantification, regions above the free DNA were considered as DNA-Dps complex. The results of this processing are presented in Figure 4.16 as plot of the fractional complex formation of Dps WT and Dps Q14E with supercoiled plasmid pUC19 as a function of protein concentration.

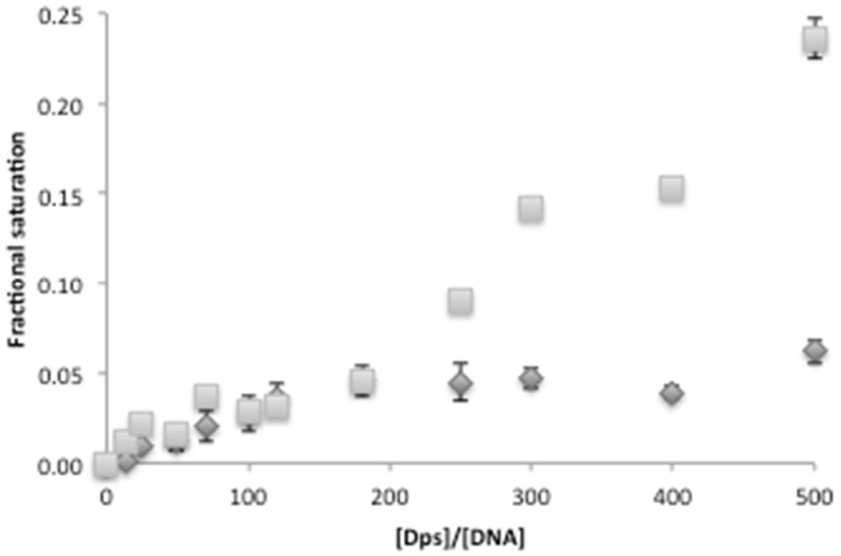

Figure 4.17 - Plot of Dps Q14E and Dps WT binding to supercoiled plasmid DNA pUC19 resulting from three analyzes to the EMSA gels. The range of protein/DNA molar ratio used was between 0 and 500 and the DNA concentration was 15 nM. Grey triangles represent the experimental data of binding of Dps Q14E to pUC19; Grey squares represent the experimental data of binding of Dps WT to pCU19.

A qualitative analysis is possible with these experiments and as can be seen in Figure 4.16, Dps WT was able to bind DNA and this binding was higher from a protein/DNA molar ratio of 250 to superior molar ratios. On the other hand, Dps F46G has a significantly lower affinity for DNA when compared to Dps WT.

Thus, from the obtained results is possible to conclude that Dps is capable of unspecific DNA binding and that the change of the charge of a single amino acid in the N-terminus was enough to significantly decrease the DNA binding affinity. This suggests that the charges of the residues from N-terminus affect the formation of the complex DNA-protein.

4.4 Site-directed mutagenesis

To obtain more insights about the interaction between DNA molecules and Dps protein, mutants of Dps from *P. nautica* were designed and obtained by site-directed mutagenesis.

These Dps mutants consisted of punctual mutations on DNA, where one nucleotide coding for an amino acid with neutral or negative charge (glutamate and aspartate, respectively) at pH 7 from N-terminus was mutated in order to produce a positively charged amino acid, a lysine. The replacement of these amino acids by positively charged residues was designed in order to obtain variants of Dps that might be able to bind DNA molecules with higher affinity, since it has been suggested the involvement of lysine residues in the interaction with DNA.

Four Dps mutants were prepared, three with a single mutation in the N-terminus, Dps D9K, Dps D11K and Dps Q14K and one with a double mutation in this same region, Dps

D9K/D11K. After producing the mutations, the clones of DNA obtained were amplified and sent for sequencing to confirm the presence of the desired mutation. The results of the sequencing are showed in Figure 4.17, through a multiple sequence alignment of Dps WT and Dps mutants.

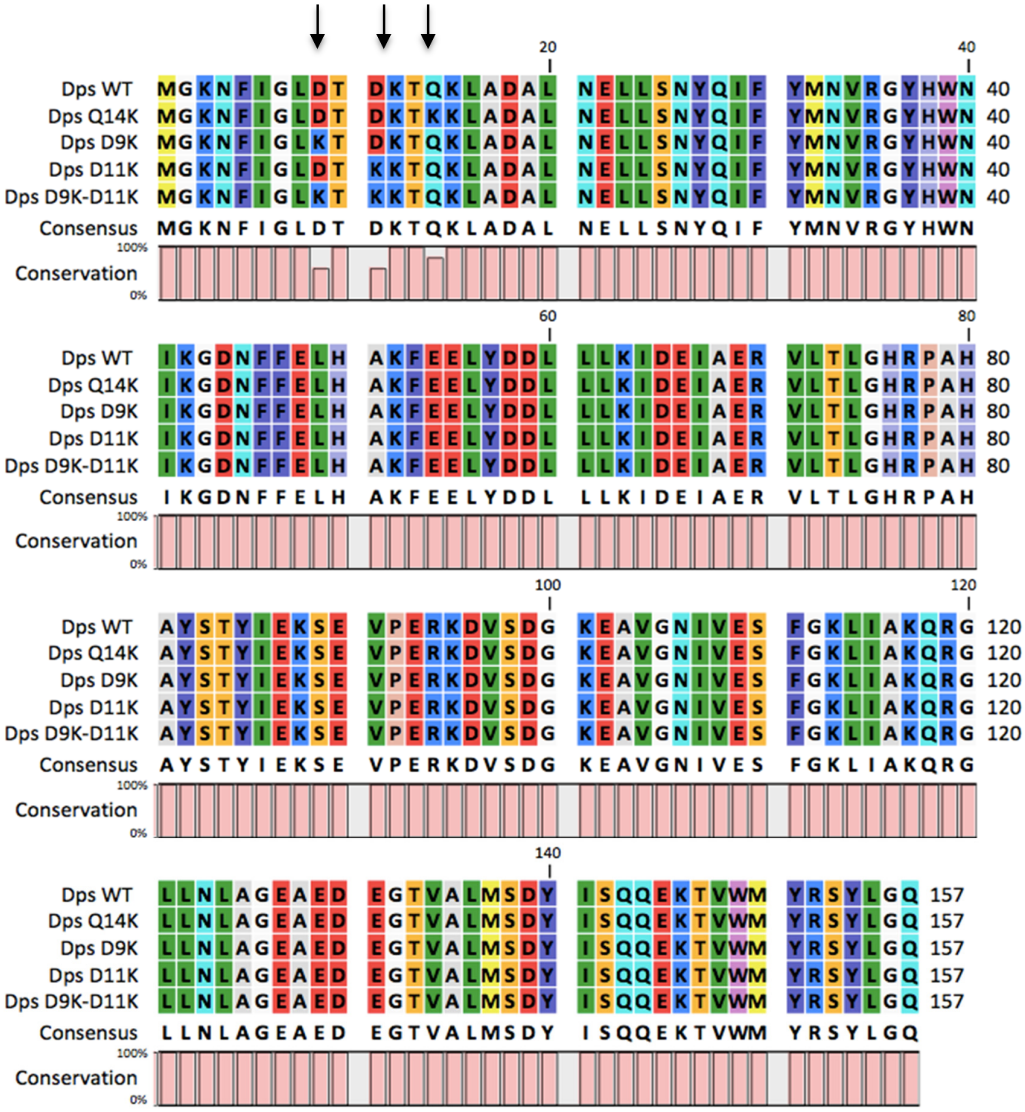

Figure 4.18 – Multiple sequence alignment of Dps WT from *P. nautica* with Dps mutants obtained by site-directed mutagenesis, Dps Q14K, Dps D9K, Dps D11K and Dps D9K/D11K. The multiple sequence alignment was produced with CLC sequence viewer and the black arrows indicate the mutated amino acids.

The multiple sequence alignment was generated to analyze the results from the DNA sequencing. As it is possible to observe in Figure 4.17, where the black arrows indicate the point mutations, all the clones with the desired mutations were successfully obtained. Therefore, these clones can be used to produce and purify the desired Dps variants, allowing further studies on Dps-DNA interaction and a better characterization of this binding.

4.5 Protein crystallography

4.5.1 Protein crystallization

In order to analyze the structural features of metal binding to the FOC and its incorporation into Dps protein from *P. nautica*, crystallization trials were performed to obtain crystals for posterior X-ray crystallographic structures determination of Apo-Dps, 12Fe-Dps and 12Cu-Dps.

Initial screens were tested and crystal growth was followed using an UV imaging system, as described in the protein crystallography section in the materials and methods chapter (3.2.9). Crystals appeared overnight and by comparison of pictures taken with visible and with UV light, it was possible to distinguish between protein and salt crystals (Figure 4.18).

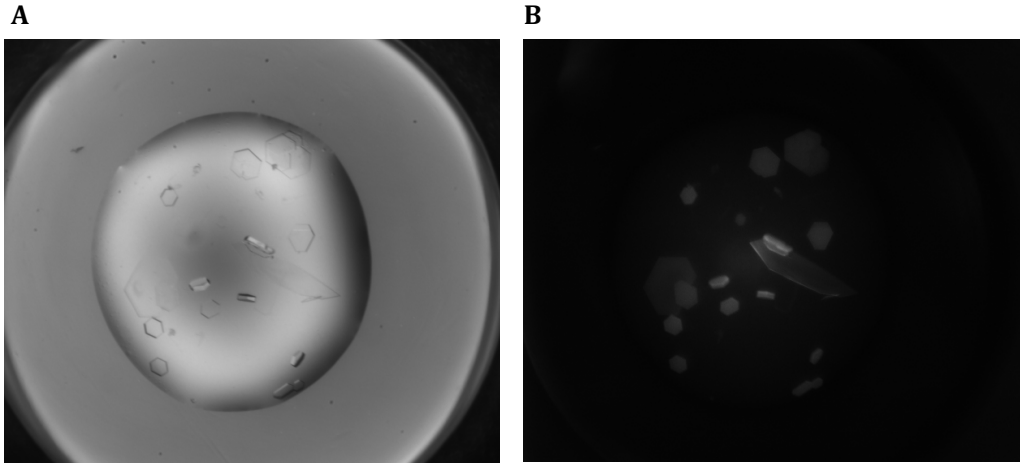

Figure 4.19 – Apo-Dps crystals. 0.3 µL of 10 mg/mL Dps protein were mixed with 0.3 µL reservoir solution consisting of 10 % (w/v) PEG 4000, 20 % (v/v) Glycerol, 0.03 M Halogens and 0.1 M MES/Imidazole buffer pH 6.5 of the Morpheus screen. Crystals under visible light (A) were identified as protein crystals by UV light (B).

Optimization of the initial protein crystals using additive screens yielded two crystallization conditions that produced better diffracting crystals, used for data collection.

The first crystallization condition used consisted of 10 % (w/v) PEG 4000, 20 % (v/v) glycerol, 0.03 M halogens and 0.1 M MES/Imidazole buffer with pH 6.5. Crystals obtained with this condition appeared overnight and had a hexagonal shape and dimensions about 250 x 250 x 25 µm (Figure 4.19, A). The diffraction quality of these crystals was improved when 0.5 µL of 0.1 M trimethylamine hydrochloride was added to the drop.

The second crystallization condition consisted of 26 % (v/v) PEG 400, 0.2 M $Ca(OAc)_2$ and 0.1 M HEPES buffer with pH 7.5. This condition was improved by adding 30 % (v/v) DMSO

and plate-shaped crystals that were grown together were obtained overnight with the dimensions about 900 x 150 x 50 µm (Figure 4.19, B).

For both crystallization conditions, plates were set up using a drop mixture of 1 µL of Dps protein (10 mg/mL), 1 µL of reservoir solution and 0.5 µL of additive with 300 µL as reservoir solution. The sealed plates where then incubated at 20 °C for crystal growth.

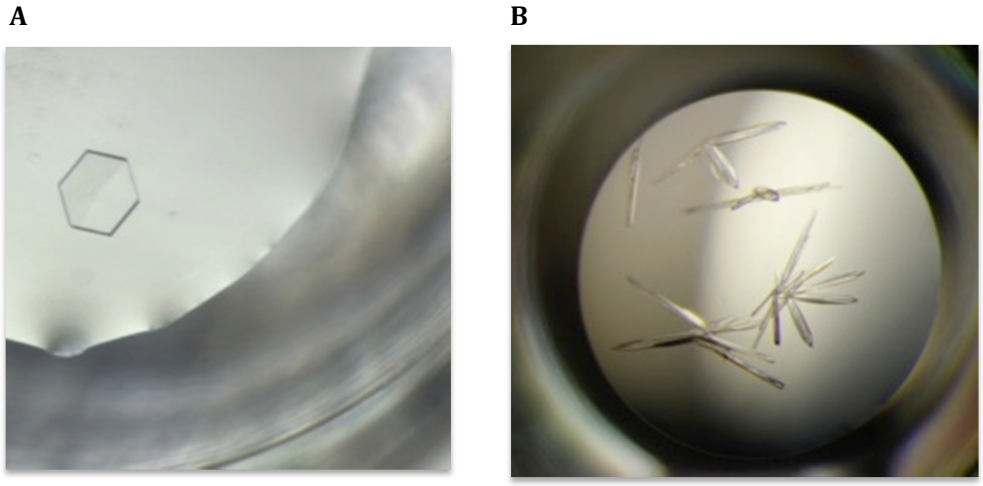

Figure 4.20 - Dps protein crystals obtained with protein 10 mg/mL under different crystallization conditions. A) Crystals of 12Cu-Dps were obtained using 10 % (w/v) PEG 4000, 20 % (v/v) glycerol, 0.03 M halogens and 0.1 M MES/Imidazole pH 6.5. B) Crystals of Apo-Dps were obtained with 26 % (v/v) PEG 400, 0.2 M $Ca(OAc)_2$ and 0.1 M HEPES pH 7.5 in the presence of 30 % (v/v) DMSO.

The second crystallization condition was found prior to this work. In this condition, crystals suffered from radiation damage when exposed to X-rays (Figure 4.20). This effect was then reduced by the addition of 30 % (v/v) DMSO to the drop.

As can be seen in Figure 4.20, the radiation damage suffered by the crystals can be observed in the plot of R_{merge} as a function of the image Number (N), after the data was processed using AIMLESS from the CCP4 package. [84] This plot shows the radiation damage of the crystal, indicated by the increase of the R_{merge} during total X-ray exposure time.

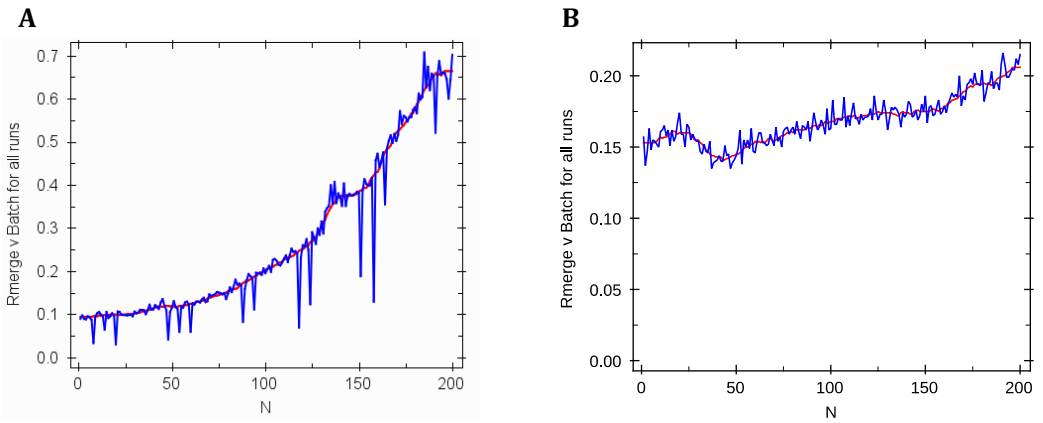

Figure 4.21 - Radiation damage of Dps crystals, as seen from a R_{merge} vs image Number (N) plot, with the second crystallization condition in the absence (A) and presence (B) of 30 % (v/v) DMSO. Data were collected at 1.5418 Å on a mar345 detector with an exposure time of 480 s and 420 s, respectively. In the absence of DMSO, the R_{merge} increases dramatically during data collection, whereas in the presence of DMSO, only a slight increase of the R_{merge} was observed.

Comparison of the plots clearly shows that DMSO increased the resistance of crystals to radiation damage when exposed to an X-ray beam. In the absence of DMSO, the R_{merge} increases dramatically during data collection caused by radiation damage. However, in the presence of DMSO, only a slight increase of the R_{merge} was observed during data collection, which shows the resistance of these crystals to radiation damage.

4.5.2 Data collection and structure determination

Data collection of Apo-Dps crystals was performed in-house using a rotating copper anode X-ray generator combined with a Saturn944+ CCD detector and at the beamline ID23-1 at the ESRF in Grenoble, France for Dps crystals with 12 Cu/Dps. The data collection of 12Fe-Dps crystals were previously performed at the beamline X06DA at Swiss Light Source (SLS) in Villigen, Switzerland.

For crystals of Dps incubated with Fe(II) and Cu(II), fluorescence scans were also recorded at the beamlines, allowing the determination of the absorption edges for anomalous data collection. For these crystals, several datasets were collected and merged with AIMLESS (CCP4 package) to improve data quality and, consequently, model quality. [85]

All data collection and refinement statistics of Apo-Dps, 12Fe-Dps and 12Cu-Dps are summarized in Table 4.1. Datasets of Dps with metals were used for structure determination and metal identification, high energy remote and peak for 12Fe-Dps and peak and inflection for 12Cu-Dps.

Molecular replacement was performed for the Apo-Dps structure using the Dps protein structure from *E. coli* (PDB code: 1DPS) as a search model, whereas the phase information for other structures was obtained by refining these structures against the model of Apo-Dps with REFMAC5 from CCP4 package. [84]

Table 4.1 – Data collection and refinement statistics for Apo-Dps, 12Fe-Dps and 12Cu-Dps. Values in parentheses represent the highest resolution shell. (a.u.: asymmetric unit).

	Apo-Dps	**12Fe-Dps**	**12Fe-Dps**	**12Cu-Dps**	**12Cu-Dps**	**12Cu-Dps**
Data collection						
Space group	$P22_12_1$	$P22_12_1$	$P22_12_1$	$P22_12_1$	$P22_12_1$	P6
Cell dimensions						
a,b,c (Å)	88.3,148.7,161.8	87.8,148.3,161.1	88.0, 148.4, 161.0	88.0,148.1,161.1	88.0,148.2,161.0	150.7,150.7,90.35
α,β,γ (°)	90.0, 90.0, 90.0	90.0, 90.0, 90.0	90.0, 90.0, 90.0	90.0, 90.0, 90.0	90.0, 90.0, 90.0	90.0,90.0,120.0
Monomers per a.u.	12	12	12	12	12	4
Wavelength (Å)	1.54179	1.00004	1.74108	1.37763	1.40893	1.37777
Resolution (Å)	56.89-1.90 (1.93-1.90)	49.43-1.70 (1.73-1.70)	49.46-2.03 (2.06-2.03)	49.36-1.80 (1.83-1.80)	47.21-1.95 (1.98-1.95)	65.25-2.95 (3.13-2.95)
Multiplicity	7.7 (7.6)	10.2 (10.1)	11.0 (2.3)	23.2 (21.0)	13.2 (11.5)	17.9 (17.8)
Completeness (%)	97.1 (94.4)	100 (100)	97.1 (62.4)	99.9 (98.1)	100 (100)	99.9 (99.9)
I/σ(I)	11.2 (2.1)	15.6 (2.1)	14.1 (0.9)	15.5 (2.6)	11.2 (1.4)	8.9 (1.9)
No. of unique reflections	162795	230540	132445	194777	153649	24750
R_{merge}	0.170 (1.004)	0.093 (1.107)	0.111 (0.996)	0.182 (1.386)	0.249 (1.886)	0.201 (1.528)
Mean (I) half-set correlation $CC_{1/2}$	0.994 (0.541)	0.999 (0.737)	0.998 (0.480)	0.998 (0.777)	0.994 (0.550)	0.998 (0.931)
Refinement						
R_{cryst}/R_{free} (%)	17.6/21.1	17.4/19.5	17.0/20.1	15.2/17.4	16.1/18.5	27.6/29.2
rmsd. deviations						
Bond lengths (Å)	0.013	0.010	0.016	0.009	0.013	0.012
Bond angles (°)	1.447	1.287	1.569	1.278	1.483	1.477
No. atoms						
Protein	15174	15142	15134	15137	15137	5028
Water	2135	1894	1031	2348	2230	-
Average B-factors (Å^2)						
Protein	18.82	23.22	32.95	17.17	21.66	-
Water	27.81	33.16	38.52	29.55	30.08	-
Ramachandran favored (%)	99.30	99.35	99.03	99.35	99.35	85.55
Ramachandran outliers (%)	0	0	0	0	0	1.79

As can be seen in Table 4.1, al crystals belong to the orthorhombic space group $P22_12_1$ with the exception of one dataset of 12Cu-Dps, crystallized in the hexagonal space group P6. These different crystals packing are likely due to the different crystallization conditions used.

The crystals with space group $P22_12_1$ and approximately unit cell dimensions of a=88 Å, b=148 Å and c=161 Å, α=β=γ=90°, were obtained with the crystallization condition that consisted of 26 % PEG 400, 0.2 M $Ca(OAc)_2$ and 0.1 M HEPES pH 7.5 and the additive 30 % DMSO. These crystals diffracted up to 1.7 Å.

Crystals with space group P6 and unit cell parameters a=b=150.7 Å and c=90.35 Å, α=β=90° and γ=120°, were obtained in 10 % PEG 4000, 20 % (v/v) glycerol, 0.03 M halogens and 0.1 M MES/Imidazole buffer with pH 6.5 and the additive 0.1 M trimethylamine hydrochloride. These crystals showed a limited diffraction quality to about 3 Å and an anisotropic diffraction pattern, as can be seen in Figure 4.21.

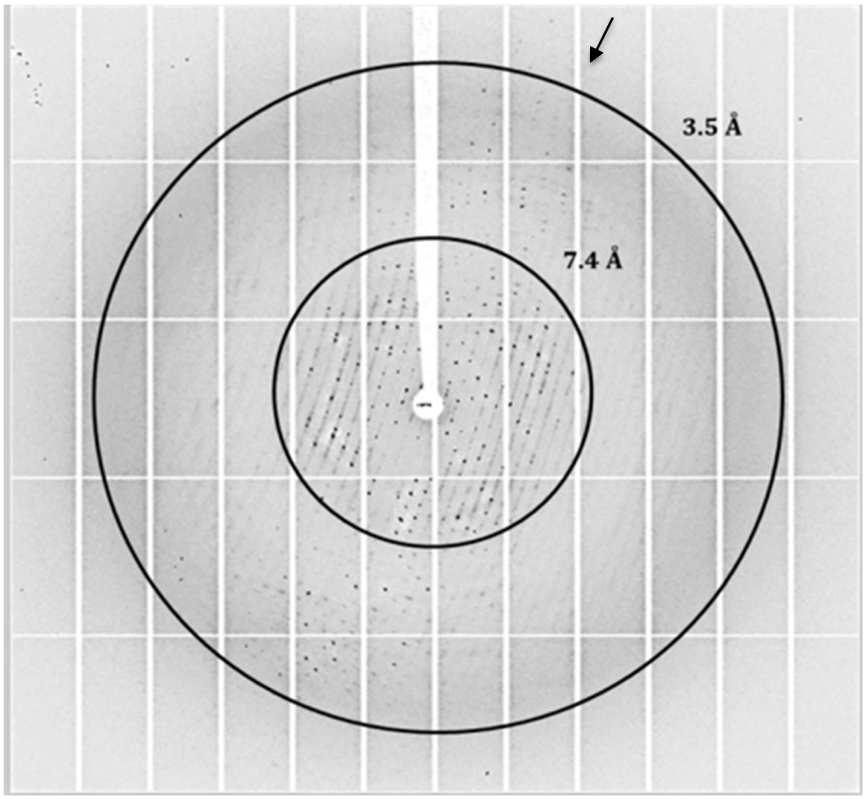

Figure 4.22 – Diffraction pattern of a crystal of 12Cu-Dps in space group P6 showing anisotropic diffraction limited to a maximum resolution of about 3 Å. The two circles highlight resolution shells of 3.5 Å (outer) and 7.4 Å (inner). The arrow points into the direction where the crystal diffracts to higher resolution.

The dataset in space group P6 was not completely refined, since a dataset with better resolution (up to 1.8 Å) was collected from a crystal of 12Cu-Dps in space group

$P22_12_1$. Therefore, the structural model obtained with this dataset was only used to analyze the crystal packing.

For all collected datasets, with the exception of the data in P6 space group, twelve monomers per asymmetric unit were detected. A solvent content of c.a. 50 % was determined for these crystals by using the Matthews program from CCP4 package. [84,91] For crystals in space group P6, four monomers were identified in the asymmetric unit with a solvent content of about 70 %.

During data processing, resolution cut-offs were set and applied to the collected data in order to improve statistics and the quality of the electron density map without losing relevant information. These limits were established considering the parameters I/σ(I) and $CC_{1/2}$, where the range of signal-to-noise ratio should be at least above 1 and the correlation coefficient $CC_{1/2}$ should be close to 1 at low resolution and about to 0.5 at high resolution. [85]

During refinement cycles, NCS restrains were applied, to improve the refinement statistics and the electron density maps. Besides, Dps protein is composed by 12 similar monomers that comprise the asymmetric unit of the crystals.

After model building and several cycles of refinement, the structural models of Apo-Dps, 12Fe-Dps and 12Cu-Dps were refined to a resolution range between 1.7 Å and 2.95 Å with R-factors between 15.2 % and 17.6 % for R_{cryst} and between 17.4 % and 21.1 % for R_{free} (Table 4.1).

4.5.3 Protein structures

4.5.3.1 Apo-Dps structure

The final model of Apo-Dps WT from *P. nautica*, composed of twelve similar monomers (Figure 4.22) represents a nearly spherical shell with an outside diameter of 9 nm and an internal cavity with a diameter of about 4.5 nm. The final R-factor and R_{free} for the model refined at 1.9 Å are 17.6 % and 21.1 %, respectively. These values and the model geometry are consistent with the high quality and resolution of the diffraction data.

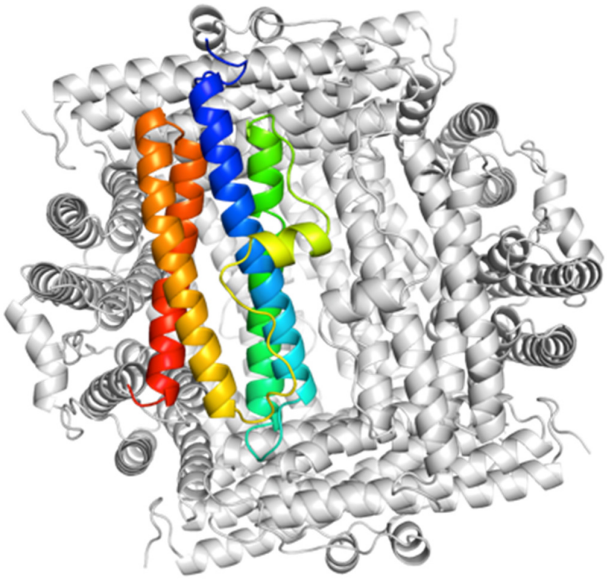

Figure 4.23 – Crystal structure of Apo-Dps WT from *P. nautica*. The cartoon representation of the overall structure displays twelve monomers assembled, showing the typical architecture of Dps protein family members. One Dps monomer is colored from blue at the N-terminus to red at the C-terminus.

During model building, electron density could be modeled for 157 amino acids. This represents the entire polypeptide sequence with the exception of the first methionine residue. Electron density for N- and C-terminal regions were observed, but these residues showed higher B-factor values due to their increased flexibility.

In the crystal structure, the internal cavity is most likely filled with disordered water molecules that cannot be observed in the calculated electron density maps (F_o-F_c and $2F_o$-F_c).

As can be seen in Figure 4.22, the *P. nautica* Dps monomer, like all other Dps family members, folds into a four α-helix bundle. Helices B and C of the monomer are connected by a loop that divides the N-terminal region (helices A-B) from the C-terminal region (helices C-D). In the middle of this loop, a short perpendicular helix was observed, most likely participating in the assembly and stabilization of dimers via its interaction with the identical short parallel helix situated in the neighboring monomer, related by a two-fold symmetry axis. [92]

As previously described, all structures available for Dps family members show a similar overall architecture. Therefore, in order to obtain more insights about amino acid composition of Dps and to identify conserved residues, a multiple sequence alignment (Figure 4.23) was performed with the Geneious Aligner from the Geneious Software. [93]

Sequence analysis was carried out with Dps protein from *P. nautica* and Dps-like proteins with known structures from *E. coli*, *L. innocua*, *S. suis*, *A. tumefaciens*, *Mycobacterium smegmatis* (*M. smegmatis*), *B. anthracis*, *D. radiodurans*, *H. pylori* and *Microbacterium arborescens* (*M. arborescens*). The Dps-like proteins used for the sequence alignment were selected from the Protein Data Bank (PDB) search.

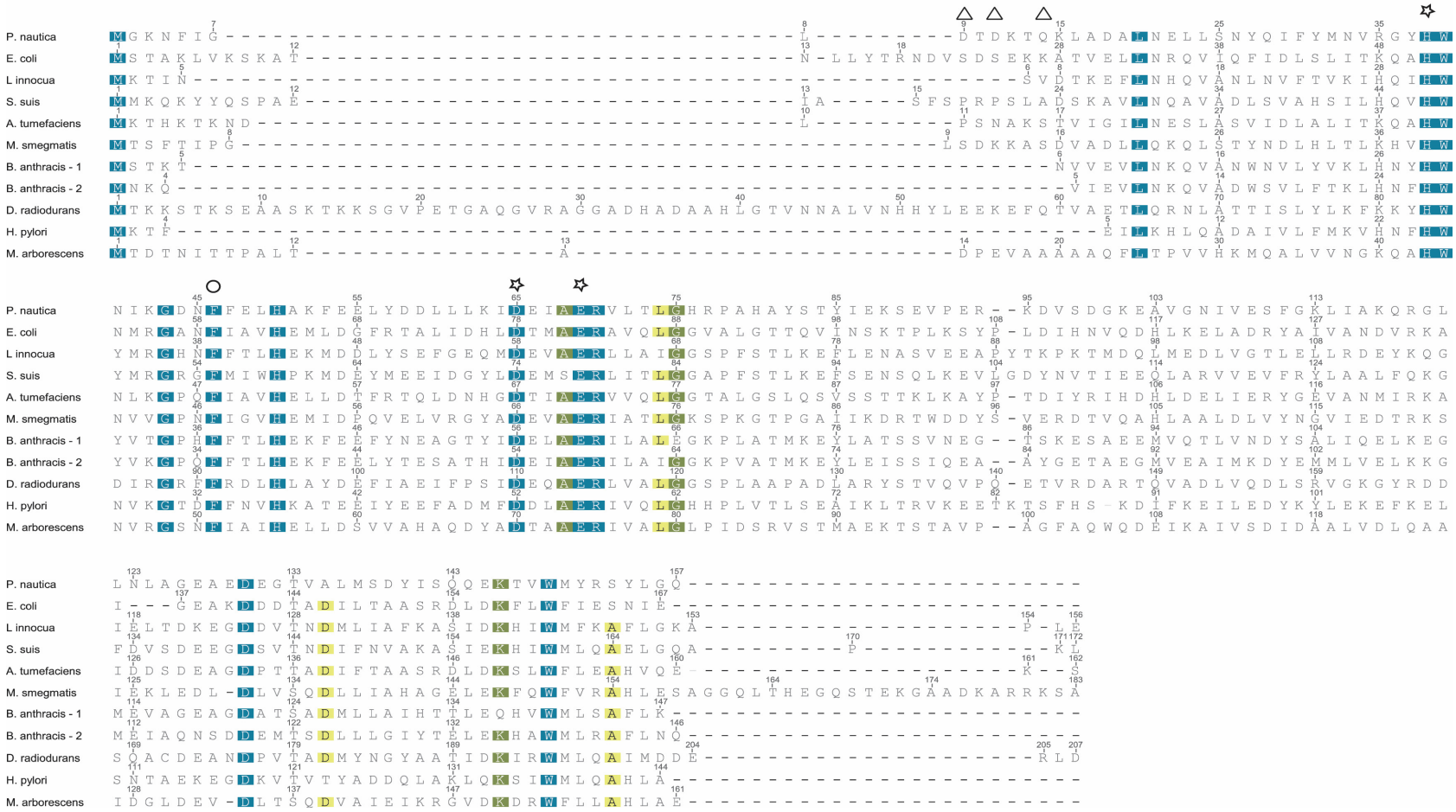

Figure 4.24 – Multiple sequence alignment of Dps WT from *P. nautica* with Dps-like proteins from different organisms, using Geneious Aligner. Conserved residues are showed with a blue, green and yellow background. The stars indicate the residues involved in iron coordination in the FOcs and the circles and triangles and circles mark the residues used for mutational studies within this thesis: D9, D11, Q14 and F46.

The multiple sequence alignment shows the conserved residues between Dps family members, highlighted with a blue, green and yellow background as well as the residues that constitute the FOC and participate in iron coordination (indicated with stars).

As seen on the sequence analysis, Dps family members share only little sequence identities (24.7 %). Three conserved residues are involved in metal coordination within the FOC: histidine (H), aspartate (D) and glutamate (E).

In Figure 4.23, mutants that were used to study the DNA binding ability of Dps are highlighted with triangles (residues Glu9 (D9), Glu11 (D11), Gln14 (Q14)), whereas circles indicate mutants that were used to study the ferroxidase activity of Dps and its ability to incorporate iron atoms (residue Phe46 (F46)).

As can be observed in the sequence alignment, only Phe46 is conserved in all Dps like proteins, whereas the N-terminus shows a higher variability.

A structural comparison of the Dps monomer from *P. nautica* with those *of E. coli*, *L. innocua*, *S. suis*, *A. tumefaciens*, *M. smegmatis*, *B. anthracis*, *D. radiodurans*, *H. pylori* and *M. arborescens* was performed to analyze the structural features of this family of proteins and is showed as ribbon representation in Figure 4.24.

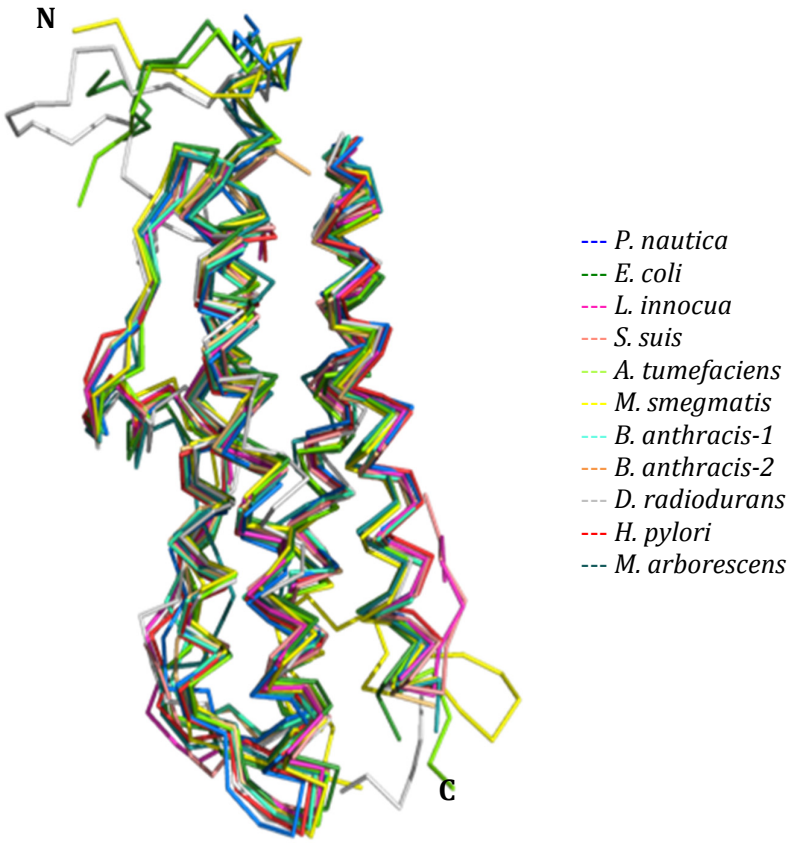

Figure 4.25 – Structural comparison of a Dps monomer from *P. nautica* with monomers from Dps-like proteins (the structures of these proteins correspond to the sequences showed in the multiple sequence alignment). Ribbon representation of the monomers in different colors (color code on the right) with N- and C-terminal regions indicated as N and C, respectively.

The most significant difference in Dps monomer is observed for the N- and C-terminal regions. In contrast to the conserved four α-helix bundle, N- and C-terminal regions exhibit a low structural similarity together with different lengths. These two regions are also more flexible than the helix bundle as reflected by increased B-factors values.

The superposition of these structures was performed using PYMOL and root-mean-square deviations values (rmsd) were calculated (Table 4.3). The rmsd values give an accurate measure of the average deviation between the atoms of the superimposed proteins. [94]

Table 4.2 – Root-mean-square deviations (Å) between Dps from *P. nautica* and Dps-like proteins with known structure (these proteins correspond to proteins showed in the multiple sequence alignment and the structural comparison).

	P. nautica **rmsd (Å)**
E. coli	1.81
L. innocua	1.32
S. suis	1.41
A. tumefaciens	1.61
M. smegmatis	1.86
B. anthracis-1	1.06
B. anthracis-2	1.05
D. radiodurans	1.81
H. pylori	0.91
M. arborescens	1.81

The superposition of the monomers of Dps from *P. nautica* and Dps-like proteins mentioned above, yield rmsd deviations of the Cα positions ranging from 0.91 Å to 1.86 Å (Table 4.3). These low values highlight the high structural similarity of Dps family members, in contrast to their primary structures.

Within the Apo-Dps structure, FOCs with different geometries and flexibility were observed in the interface of two symmetry-related monomers (Figure 4.25).

The nature of the metal coordination at the FOC is very similar to the one observed in other Dps structures and involves interactions with the side-chains of the hydrophilic amino acids His38, Aps65, Glu69 and water molecules.

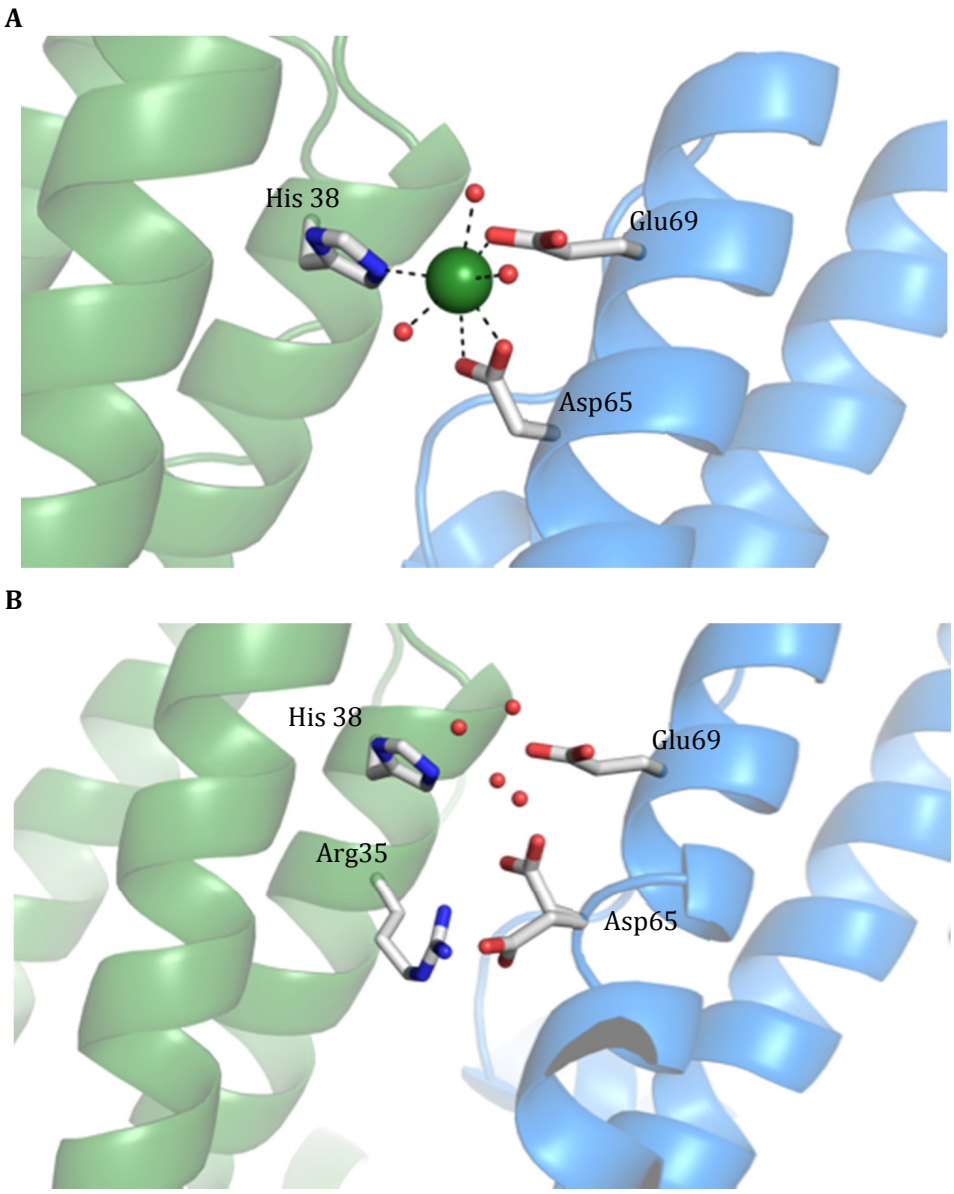

Figure 4.26 - Detailed view of FOCs located between two symmetry-related monomers of Apo-Dps structure. The two monomers are showed as a cartoon representation in green and blue. The side-chains of the residues that form the FOC and the residue that participates in the salt bridge are represented as sticks (His38, Aps 65, Glu29 and Arg35). A calcium atom is showed as a green sphere and the water molecules as red spheres. The coordination sphere is presented in black dashed lines. A) FOC with bound Ca^{2+}. B) FOC center without metal bound.

As expected, no iron was observed in the Apo-Dps structure since the protein was purified in its absence. This is supported by the absence of electron density at the FOC within the anomalous map.

As showed in Figure 4.25 A, in one of the twelve FOCs, a Ca(II) atom was modeled according to the high electron density peak and the observed coordination sphere.

The presence of calcium ions within the protein structure is justified by the high concentration of $Ca(OAc)_2$ in the reservoir solution used for the crystal growth.

Calcium atoms were also found in the interface between symmetry-related Dps molecules, facilitating crystal contacts (similar to what is showed in Figure 4.34).

The distances between the Ca(II) atom and the side-chain of the residues that form the FOC and the coordinating water molecules are showed in Table 4.4, together with their correspondent B-factor values.

In seven FOCs no metals were found and residue Asp65 adopts two alternative conformations (Figure 4.25, B). This different positioning of Asp65 side-chain demonstrates a certain degree of flexibility for the active site that can also be seen by the B-factor values presented in Table 4.5. One of the conformations of Asp65 act as a ligand for metal binding to the FOC, whereas the other conformation forms a salt bridge with the side-chain of Arg35 from the symmetry-related monomer (Figure 4.25, B). This salt bridge is similar to what was observed for the structure of Dps protein from *A. tumefaciens*. [40]

In the other four FOCs no metals were observed and Asp65 adopts only the conformation that act as ligand for metal binding.

Table 4.3 – Residues and distances of calcium coordination (Å) and B-factor values (Å^2) of FOC with calcium bound in the structure of Apo-Dps.

Residue	B-factor (Å^2)
Asp65 (OD1)/A	13.19/19.67
Asp65 (OD2)/A	14.46/18.18
Glu69 (OE2)/A	36.16
His38 (NE2)/B	21.87
W13	23.21
W1832	18.57
W1833	28.68
W2014	36.64

Table 4.4 – Residues of the FOC without metals bound and B-factor values (Å^2) in the structure of Apo-Dps.

Residue	Distance to Ca(II) (Å)	B-factor (Å^2)
Ca(II)	-	22.96
Asp65 (OD1)/A	3.3	15.28
Asp65 (OD2)/A	2.2	17.09
Glu69 (OE2)/A	2.5	14.31
His38 (NE2)/B	2.8	14.73
W1829	2.5	17.32
W1830	2.4	20.35
W1981	2.2	30.66

The distances observed between protein residues and water molecules that participate in calcium coordination range from 2.2 Å to 3.3 Å. The B-factors observed for these residues and for the calcium atom ranged from 14.31 $Å^2$ to 30.66 $Å^2$ were considered reasonable. Thus, Ca(II) is able to bind to the FOC with a coordination number of 7, which is in accordance to what expected for this atom within a crystal structure (between 6 and 8). [95]

In case of metal absence in the FOC, the B-factors are increased significantly, evidencing the fact that Aps65 can adopt alternative conformations and a conformational change in its side-chain might be necessary to favor metal binding.

4.5.3.2 12Fe-Dps structure

The final model of Dps incubated with 12 Fe(II)/Dps from *P. nautica* is assembled by twelve similar monomers (Figure 4.26) with 157 amino acids per monomer, as observed in the Apo-Dps structure. In contrast to Apo-Dps, several iron atoms were identified in this structural model.

The diffraction data used to obtain this model was collected at high energy remote (wavelength of 1.74108 Å) and it could be refined to a higher resolution. After refinement, a final R-factor of 17.4 % at a resolution of 1.7 Å was achieved. The final model geometry parameters reveal the high quality and resolution of the diffraction data (Table 4.1).

For the assignment of all iron atoms within the protein structure, diffraction data collected at the iron peak and inflection point were used as determined by a fluorescence scan.

As observed for the Apo-Dps structure, calcium atoms were also found in this structural model located between symmetry-related molecules and facilitating crystal contacts (similar to what is showed in Figure 4.34).

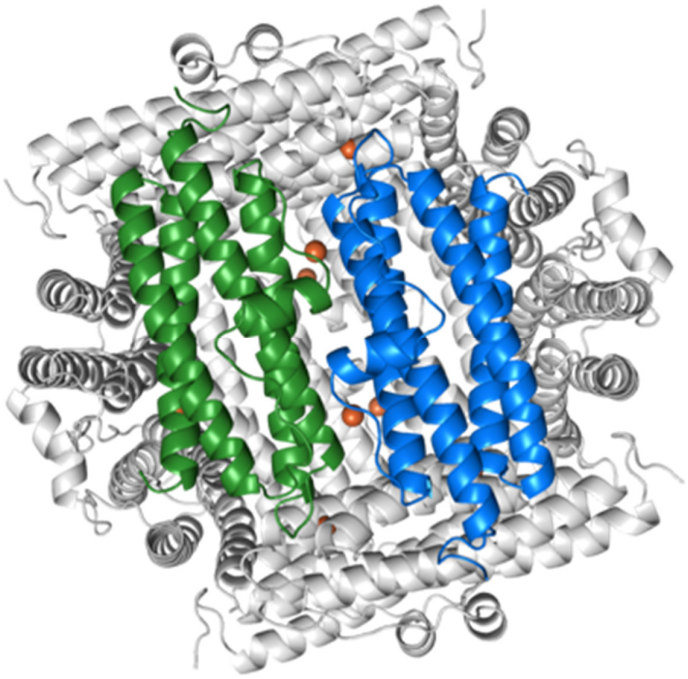

Figure 4.27 - Crystal structure of *P. nautica* 12Fe-Dps. The overall structure showed in cartoon representation displays twelve monomers assembled into a hollow sphere and twelve Fe(II) atoms bound to the FOCs. A Dps dimer is highlighted in green and blue and the iron atoms are showed as orange spheres.

Twelve iron atoms were found in each FOC located at the interface of two symmetry-related monomers (Figure 4.26).

The ferrous iron atoms represented as orange spheres identified in the FOCs were assigned with occupancy of 1. Besides these iron atoms, seven additional iron atoms with an occupancy of 0.5 were assigned within the protein structure. They are located in the pores at the junction of the threefold symmetry-related monomers that connect the outside of the dodecamer with the internal cavity (similar to what is showed in Figure 4.30).

The assignment of iron atoms was performed considering the calculated anomalous maps as well as the σ level of the electron density map (F_o-F_c) and the difference electron density map ($2F_o$-F_c). In the FOC, two iron atoms were identified per dimer by a strong anomalous signal found in the electron density maps calculated from the data collected at the iron absorption edge (Figure 4.27).

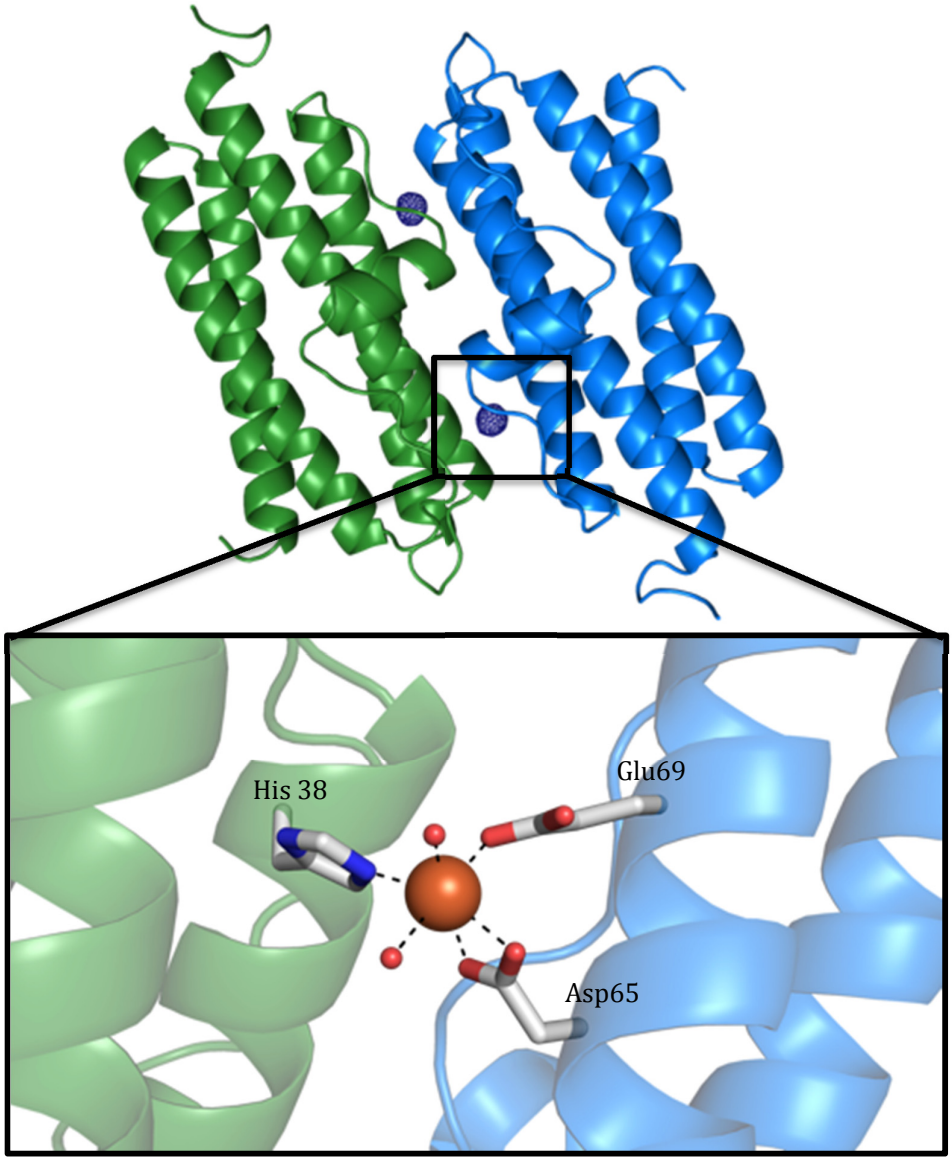

Figure 4.28 –Detailed view of the FOC in a dimer of 12Fe-Dps. The two monomers are showed as a cartoon representation in green and blue. The side-chains of residues that build up the FOC are showed as sticks (His38, Aps 65 and Glu29). A) Representation of two FOCs located between two symmetry-related monomers. The anomalous density, showed as blue grid, represents the position of the iron atoms. Electron density in the anomalous map was contoured at 3.0 σ. B) Detailed view of one FOC with one iron atom bound. The iron atom is showed as an orange sphere and the water molecules as red spheres. The black dashed lines represent the interactions established by the iron within the coordination sphere.

Each iron atom is coordinated by side-chains of Asp65 and Glu69 from one monomer, by His38 from the symmetry-related monomer and by two water molecules.

Considering the distances and the B-factors observed for these residues (Table 4.6), iron has a coordination number of 6 (octahedral), which is in accordance to one of its preferred coordination numbers within protein structures (preferred coordination number for Fe(II) is between 4 and 6). [96,97]

Table 4.5 – Coordination residues and distances to iron binding (Å) and B-factor values (Å^2) of one FOC from the structural model of 12Fe-Dps.

Residue	Distance to Fe(II) (Å)	B-factor (Å^2)
Fe(II)	-	17.94
Asp65 (OD1)/A	2.4	15.59
Asp65 (OD2)/A	2.2	14.69
Glu69 (OE2)/A	2.1	15.75
His38 (NE2)/B	2.2	14.35
W772	2.0	22.58
W623	2.3	19.70

One iron atom was found in each FOC, with similar B-factor values to the one presented in Table 4.6. FOCs were fully occupied with Fe(II) proved by the low B-factor value of 17.94 Å^2.

4.5.3.3 12Cu-Dps structure

The final model of *P. nautica* Dps incubated with 12 Cu(II)/Dps comprised the typical twelve monomers with 157 amino acids (Figure 4.28). This model was built using the of high quality diffraction data collected at the copper absorption edge (wavelength of 1.37763 Å) to a final resolution of 1.8 Å and an R-factor of 15.2 % (Table 4.1). This showed that Cu(II) atoms could also bind to Dps protein in the same iron sites of the FOCs.

For unambiguous assignment of copper atoms, the anomalous diffraction data collected at the copper peak and inflection point was used, allowing the identification of its position within the protein structure.

As for the Apo-Dps and the 12Fe-Dps structure, Ca(II) atoms were also found facilitating crystal contacts (Figures 4.34 and 4.35).

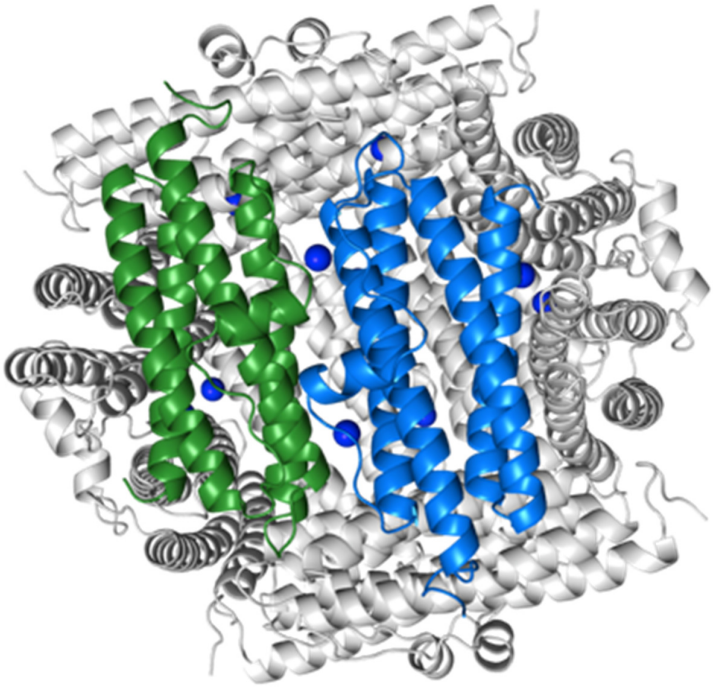

Figure 4.29 - Crystal structure of *P. nautica* 12Cu-Dps. The overall structure showed in cartoon representation displays twelve monomers assembled into a hollow sphere and twelve Cu(II) atoms are bound to the FOCs. A Dps dimer is highlighted in green and blue and copper atoms are showed as blue spheres.

Cu(II) atoms were found in the FOCs with an occupancy of 1 according to the strong electron density peaks in the F_o-F_c map together with strong signals found in the anomalous difference map that was calculated from data collected at the copper absorption edge. As mentioned for the 12Fe-Dps, additional seven Cu(II) atoms were assigned in the structure (Figure 4.29), as will be showed later.

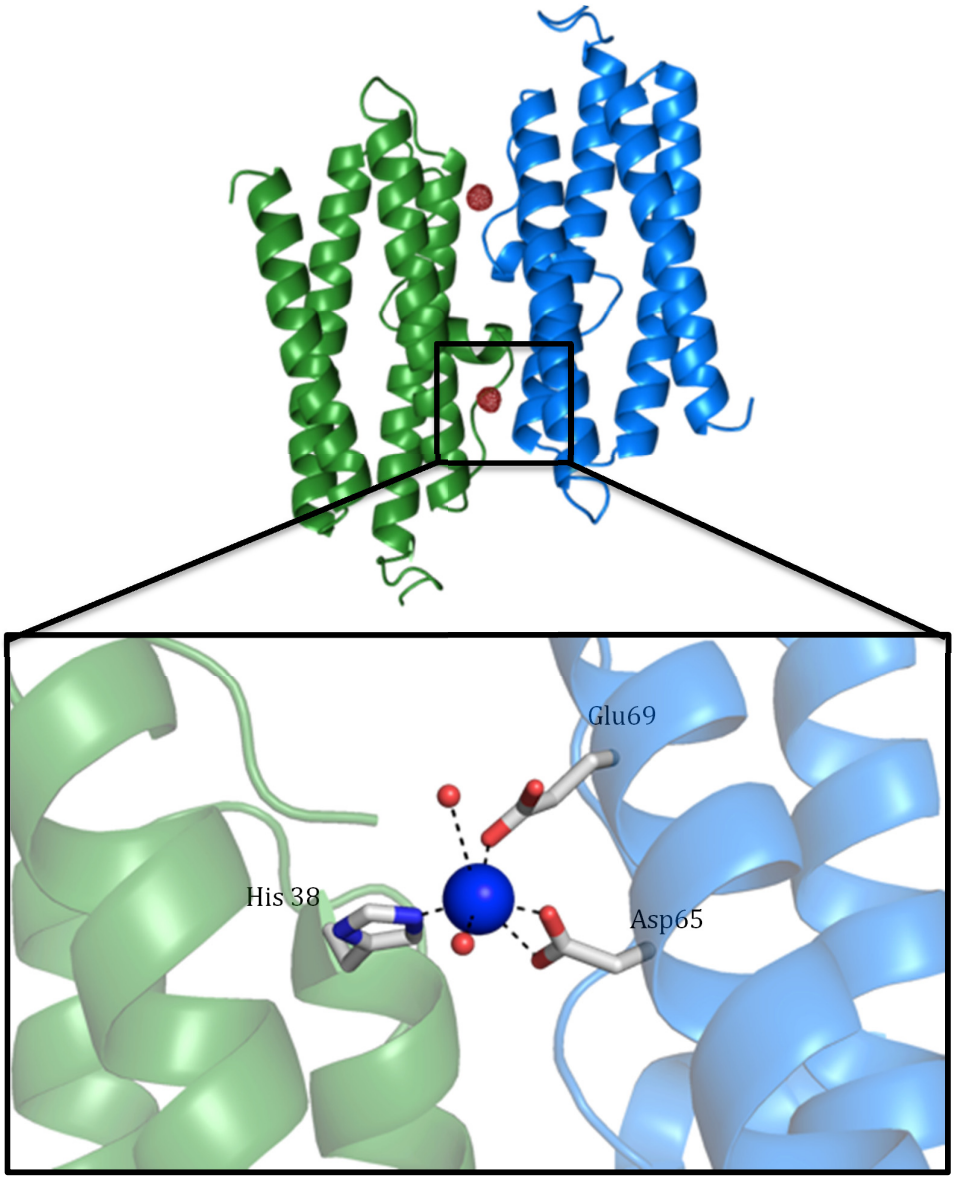

Figure 4.30 – Detailed view of the FOC in a dimer of 12Cu-Dps. The two monomers are showed as a cartoon representation in green and blue. The side-chains of residues that build up the FOC are showed as sticks (His38, Aps 65 and Glu29). A) Representation of two FOCs located between two symmetry-related monomers. The anomalous density, showed as a red grid, represents the position of the copper atoms within the protein structure. The electron density in the anomalous map was contoured at 3.0 σ. B) Detailed view of the FOC with one copper atom bound. The copper atom is showed as a blue sphere and water molecules as red spheres. The black dashed lines represent the interactions established by the copper within its coordination sphere.

The side-chains of protein residues His38, Asp65 and Glu69 are involved in copper binding in the FOCs, as observed for the iron and calcium binding. However, considering the distances and the B-factors (Table 4.7), copper has a different coordination number in comparison to iron.

Table 4.6 – Coordination residues and distances of copper binding (Å) and B-factor values (Å^2) of one FOC from the structural model of 12Cu-Dps. The coordination of Cu(II) by W228 and W1782 (underlined) can be questioned due to an increased distance of 3.3 Å for W228 and a very high B-factor of 45.07 Å^2 for W1782.

Residue	Distance to Cu(II) (Å)	B-factor (Å^2)
Cu(II)	-	16.47
Asp65 (OD1)/A	2.7	10.75
Asp65 (OD2)/A	2.0	11.08
Glu69 (OE2)/A	2.0	14.89
His38 (NE2)/B	2.0	10.64
W228	3.3	23.59
W1782	2.4	45.07

Here, Cu(II) appears not to be coordinated by water molecules, which can be seen by the high distance of 3.3 Å for W228 and by the high B-factor of 45.07 Å^2 for W1782. This results in a tetrahedral coordination of copper, which is in agreement with a coordination number of 4 or 5 for Cu(II). [96,98]

Additionally, seven copper atoms were assigned in positions located at the junction of three symmetry-related monomers created by the Dps dodecamer, with a 0.5 occupancy (Figure 4.30). This is similar to the observed for the structure of 12Fe-Dps.

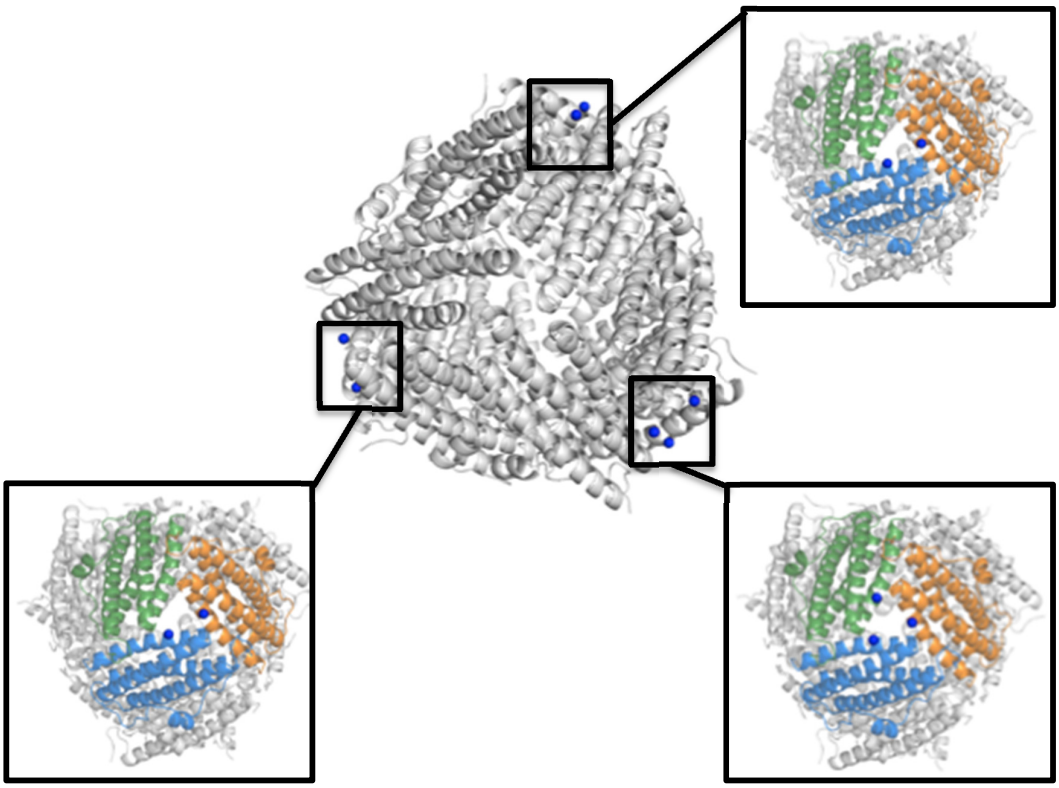

Figure 4.31 – Hydrophilic pores formed at the interception of three 12Cu-Dps monomers. Three hydrophilic pores with copper atoms bounds are highlighted. The three monomers in cartoon representation are showed in different colors (green, blue and orange) and the copper atoms are showed as blue spheres.

At the junction of three symmetry-related monomers, pores are created connecting the exterior of the dodecamer to the inner cavity. In the structure, only three pores out of four were observed with copper atoms bound (Figure 4.30). In one pore, three copper atoms were found, whereas in the other two pores, only two copper atoms were found.

In these extra positions where copper atoms were assigned, peaks in the electron density maps (F_o-F_c and $2F_o$-F_c) were observed together with strong anomalous signals in the anomalous map, generated with data collected at the copper absorption edge. These peaks were interpreted as partially occupied Cu(II) atoms giving B-factor values of about 30 $Å^2$.

The residues that participate in copper coordination demonstrate the presence of hydrophilic pores (Figure 4.31).

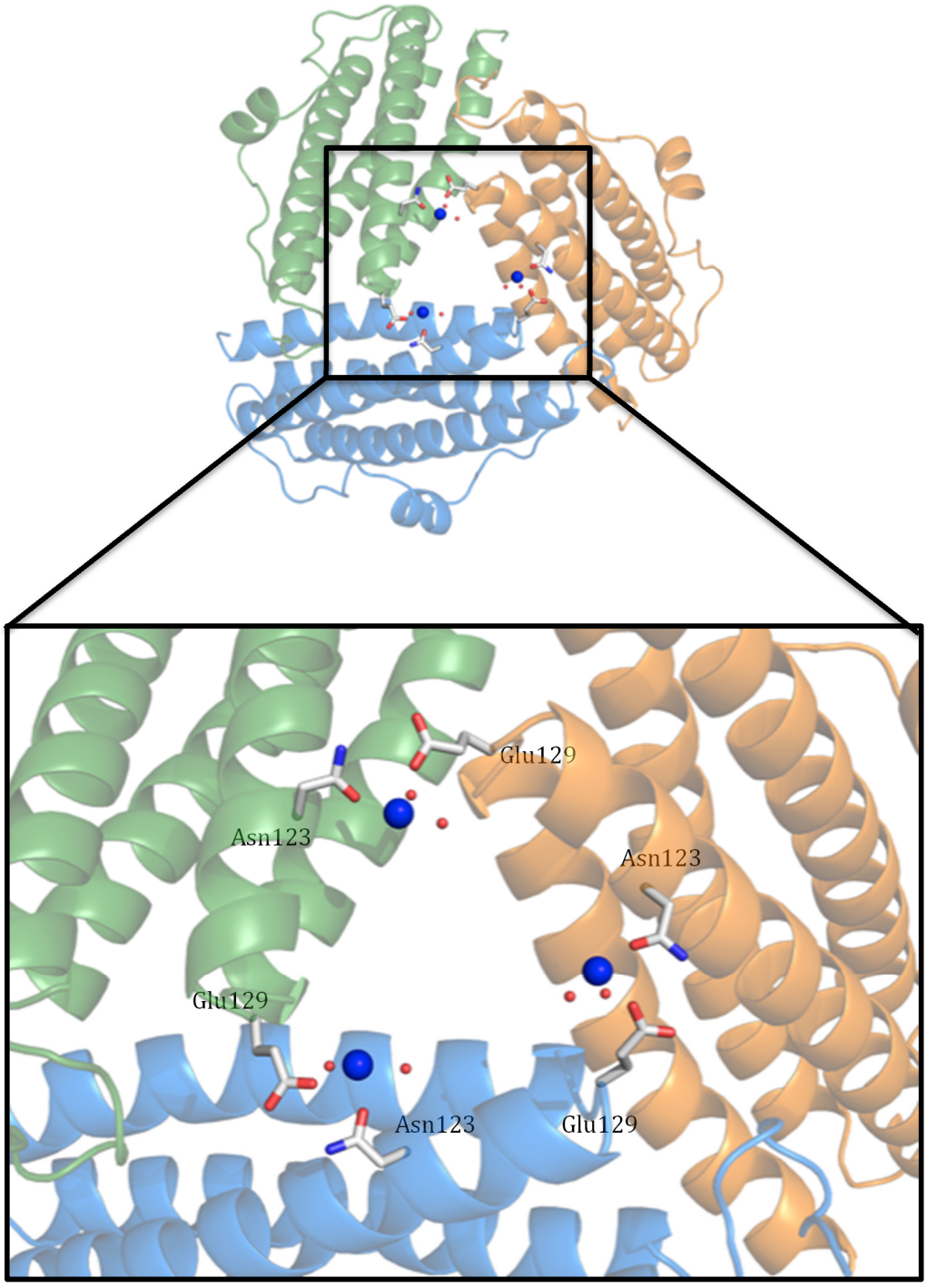

Figure 4.32 – Detailed view of the junction of three monomers forming a hydrophilic pore with copper atoms bound. The monomers that create these pores are showed as a cartoon representation in different colors. The blue spheres represent copper atoms, while the small red spheres represent water molecules. The side-chains of residues that might participate in metal coordination in these pores are showed as sticks (Asn123 and Glu129).

The copper atoms in these positions have most likely a coordination number of 4, as seen in the FOC. They are coordinated by the side-chains of Asp123 and Glu129 from different monomers and by two water molecules, with distances ranging from 2.3 Å to 2.7 Å and B-factor values between 20.17 $Å^2$ to 38.52 $Å^2$ (Figure 4.31).

The pores (with an approximately diameter of 10 Å) lined up with hydrophilic residues, mainly negatively charged such as glutamate, are potential entry routes for Cu(II) or Fe(II) atoms. The residues present in these pores might form a negatively charged gradient towards the pore, which guides the metal ions to the interior of the Dps dodecamer.

The crystal structure of 12Cu-Dps from *P. nautica* in space group $P22_12_1$ reveals, at atomic resolution, the packing details about the packing of the molecules within the crystal. A view of the crystal packing along the different unit cell axes (a, b and c) is showed in Figure 4.32 with layers of Dps molecules presented in different colors.

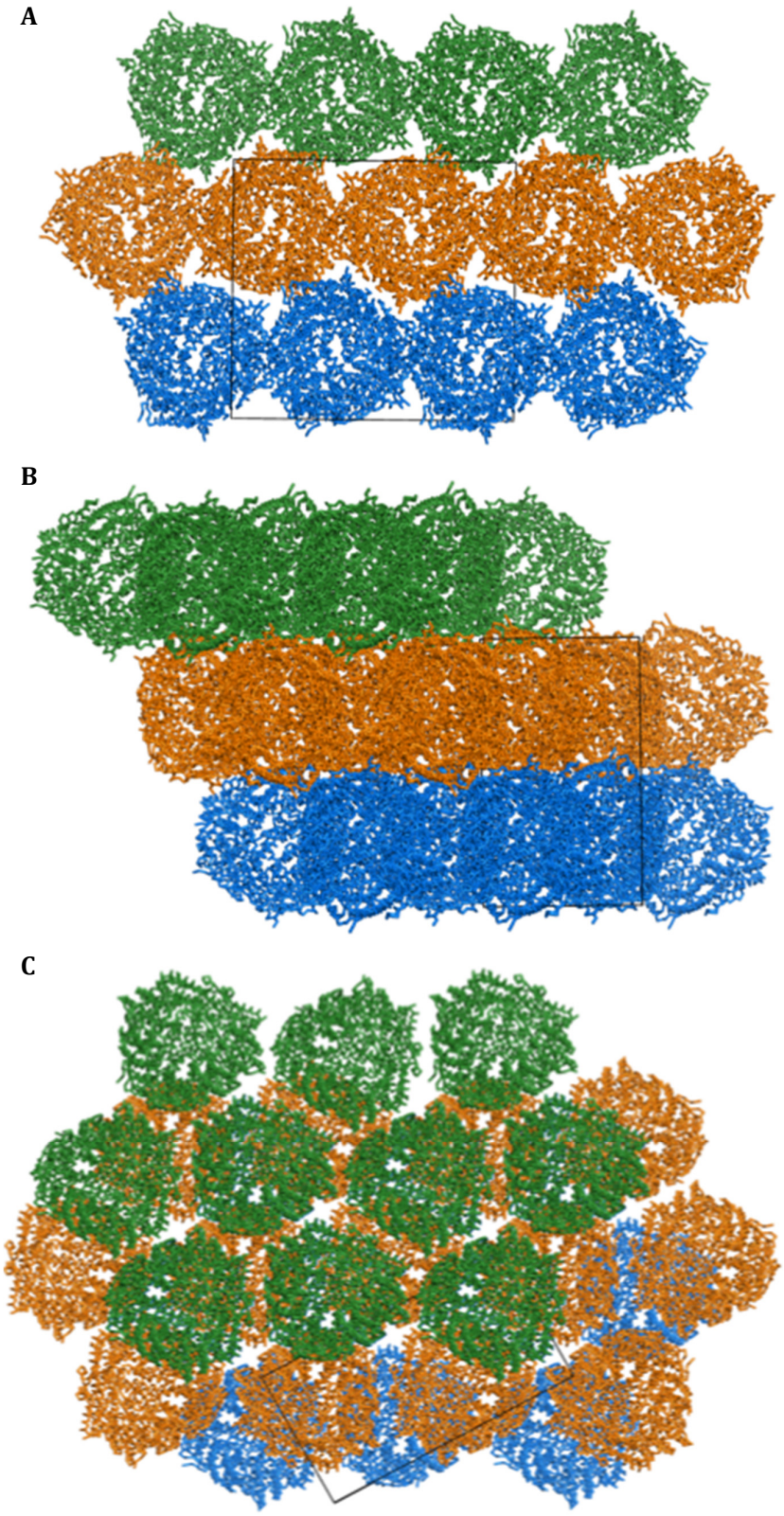

Figure 4.33 – Overall view of the crystal packing of 12Cu-Dps (space group: $P22_12_1$) along the different cell axes a (A), b (B) and c (C). Each asymmetric unit contains a Dps dodecamer. Dps molecules are showed in different colors (green, orange and blue) to evidence the different layers. The black rectangle represents the unit cell.

The packing of the Dps dodecamers within this multi-layered structure is approximately hexagonal. This pseudo-hexagonal and very tight crystal packing is similar to that observed in electron microscopy studies *in vivo* for Dps molecules and Dps-DNA complexes (Figure 4.33).[27,46]

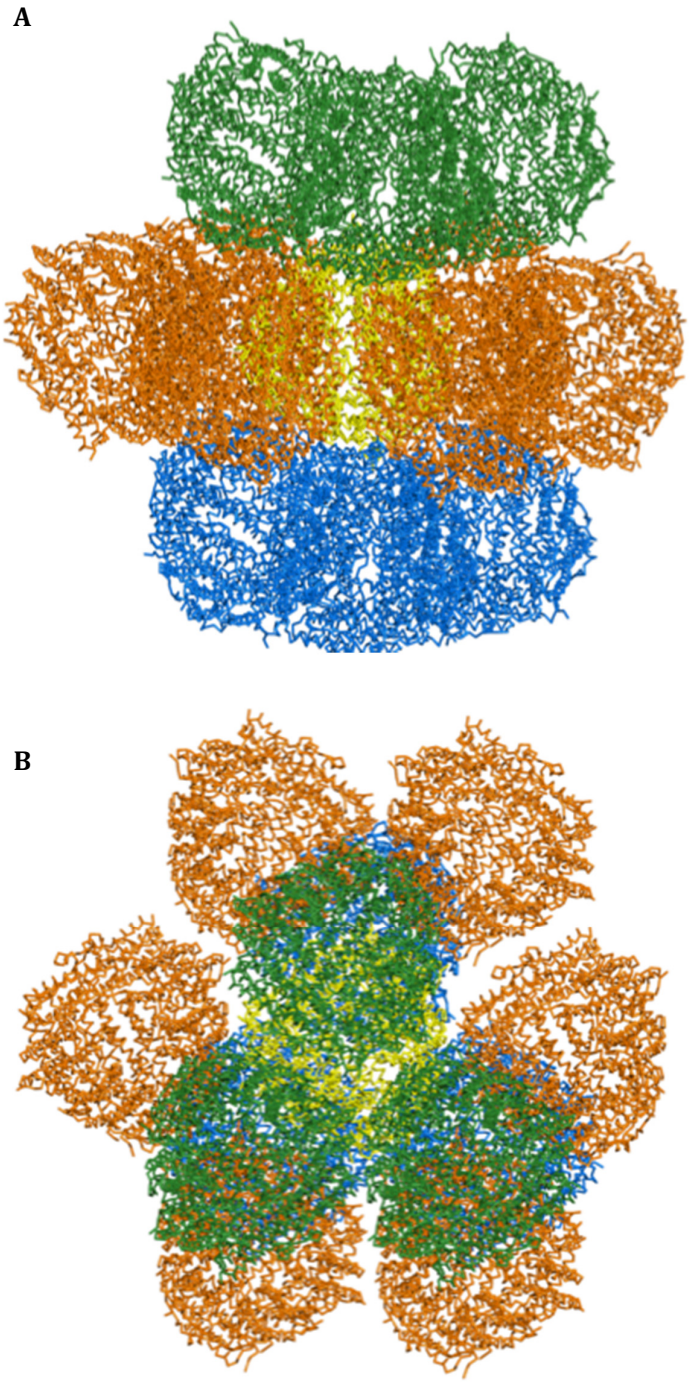

Figure 4.34 – Crystal contacts of 12Cu-Dps (space group: $P22_12_1$). One Dps molecule (yellow) is neighbored by 12 Dps molecules, with three molecules in the layer below (blue), three molecules in the layer above (green) and six molecules within the same layer (orange). A and B are views of the crystal contacts rotated by 90 °.

Each Dps molecule is neighbored by twelve monomers (Figure 4.33). From these twelve neighbors, three are located in a layer below, three in a layer above and six are situated within the same layer.

It was observed that some of these crystal contacts were facilitated by calcium atoms coordinated by the side-chains of residues from symmetry-related molecules, (Figures 4.34 and 4.35). In these positions, Ca(II) atoms were assigned with occupancy of 1 (giving B-factor values of about 20 $Å^2$), due to the high level of electron density supported by the presence of anomalous signal collected at the copper inflection point. Calcium atoms were present in the reservoir solution used for crystal growth.

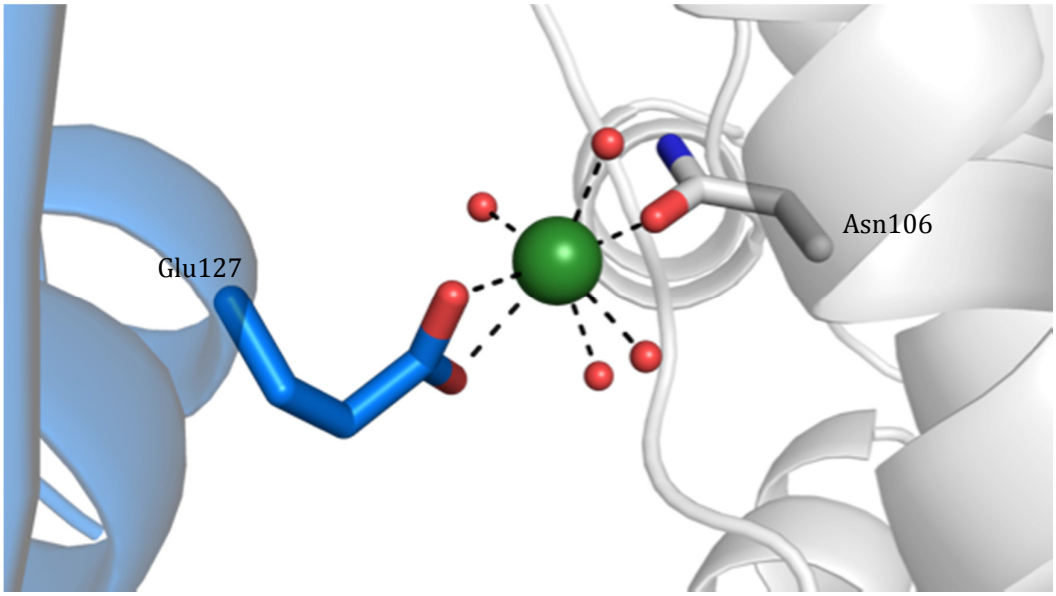

Figure 4.35 – Detailed view of a crystal contact established between two symmetry-related Dps molecules. One calcium atom is involved in the crystal contact, coordinated by Glu127 from one molecule (blue) and Asn106 from another, symmetry-related molecule (grey). The Ca(II) atom is showed as a green sphere and water molecules as small red spheres. The coordination sphere is presented in black dashed lines.

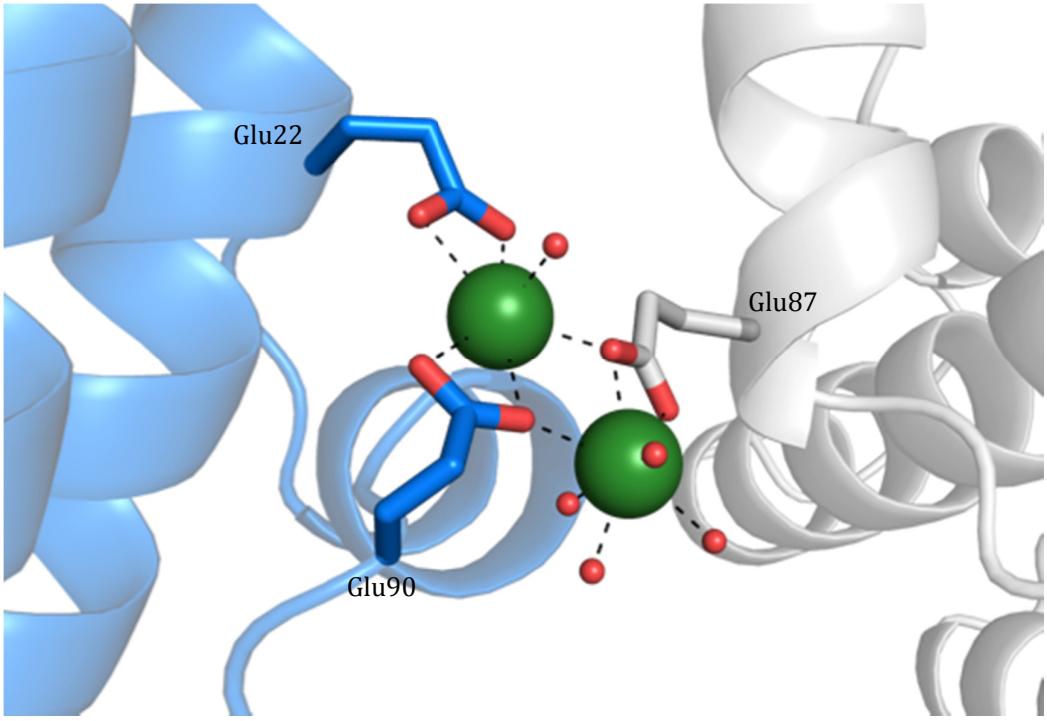

Figure 4.36 - Detailed view of a crystal contact established between two symmetry-related Dps molecules. Two calcium atoms are involved in the crystal contacts, coordinated by Glu22 and Glu90 from one molecule (blue) and Glu87 from the neighbored, symmetry-related molecule (grey). Ca(II) atoms are showed as green spheres and water molecules as small red spheres. The coordination sphere is presented in black dashed lines.

In Figure 4.34, one calcium atom was observed with a coordination number 7, as observed in the FOC of the Apo-Dps structure, whereas in Figure 4.35, two calcium atoms were assigned with coordination numbers of 6 and 7.

Refinement of this structure reveled suitable B-factor values ranging from 19.30 $Å^2$ to 32.40 $Å^2$ and coordination distances between 2.0 Å and 2.6 Å that support the presence of calcium atoms promoting crystal contacts at the interface between symmetry-related dodecamers. These atoms may help in the stabilization of the crystal packing.

On the other hand, a different crystal packing was observed for the crystal structure of 12Cu-Dps from *P. nautica* in space group P6 (Figure 4.36).

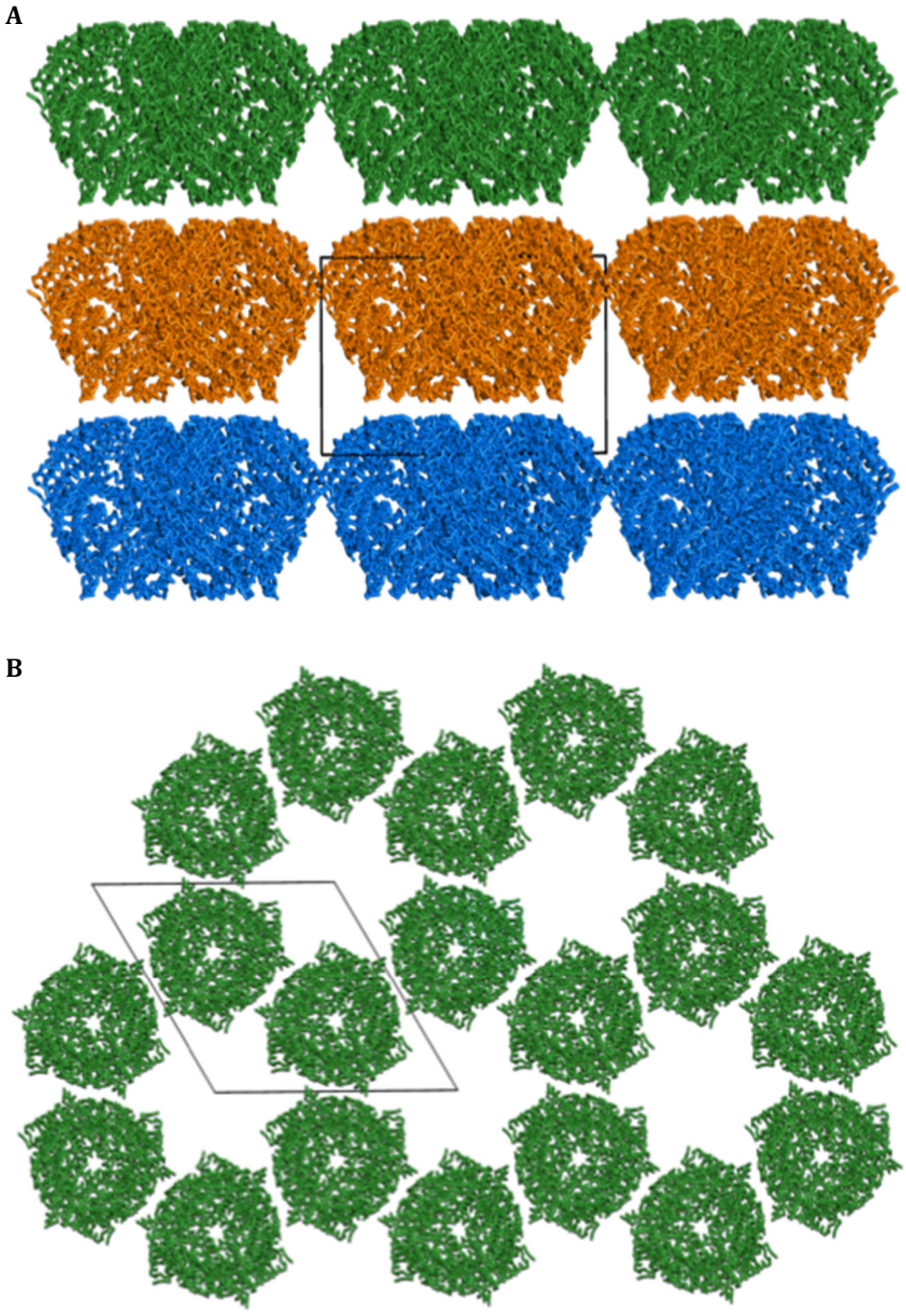

Figure 4.37 - Overall view of the crystal packing of 12Cu-Dps (space group: P6) along the different cell axes a, b (A) and c (B). Each asymmetric unit contains 4 Dps monomers forming two homodimers. Dps molecules are showed in different colors (green, orange and blue), evidencing the different layers. The black rectangle represents the unit cell.

In this crystal, a multi-layered structure is observed where molecules are superimposed along the c axis resulting in a rather loose crystal packing in comparison with crystals obtained

in space group $P22_12_1$. This packing causes the anisotropic effect along the c axis that can be seen in the diffraction pattern (Figure 4.21)

Crystal contacts were not analyzed in detail since the crystal showed limited quality and maximum diffraction of 2.95 Å. Figure 4.37 shows the crystal contacts between adjacent Dps molecules.

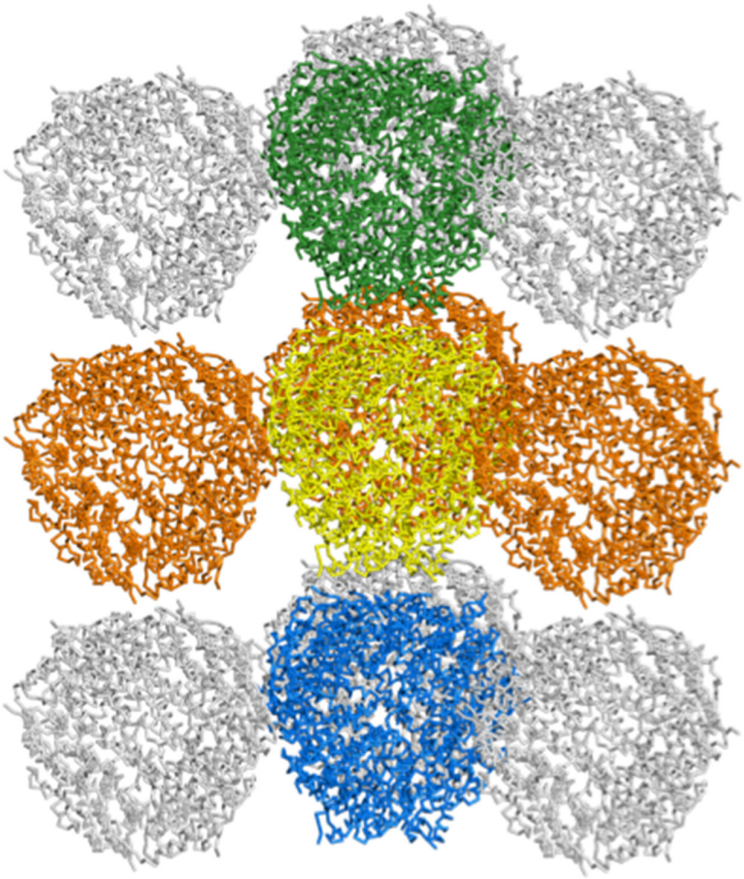

Figure 4.38 - Overall view of crystal contacts of 12Cu-Dps (space group: P6). One Dps molecule (yellow) has five Dps molecules as neighbors, one molecule in the layer below (blue), one molecule in the layer above (green) and three molecules within the same layer (orange).

Every dodecamer within the layer has contacts with five neighboring dodecamers. Three of these Dps dodecamers are located within the same layer, one is situated in the layer above and one is in the layer below.

5 Discussion

Dps are proteins that are expressed in different bacterial organisms. These proteins have the ability to incorporate and store iron atoms in their inner cavity and, in some organisms, to protect DNA from oxidative damage. Although Dps proteins have a highly conserved three-tridimensional structure, through a multiple sequence alignment (Figure 4.23) is possible to observe that these proteins have very different primary structures, which can be seen by the low number of conserved residues and by their low sequence identity of 24.7 %.

A structural comparison between monomers of Dps-like proteins from different organisms (Figure 4.24), showed a conserved four α-helix bundle and variable N- and C-terminal regions. The functional advantage of flexible regions is still under debate, however, it is most likely related with the N-terminus involvement in the DNA binding. [31,99] Only for *M. smegmatis* Dps, the C-terminus has been suggested to be involved in DNA binding. [100] The calculated root-mean-square deviations for the proteins used for the structural comparison and the sequence alignment (Table 4.3) ranging between 0.91 Å and 1.86 Å, also showed the high structural similarity observed for Dps protein family.

Despite sharing the same function with ferritins, the ability to sequester and accommodate iron atoms in the central cavity through an oxidation step catalyzed in the FOC, the molecular mechanism of iron incorporation in Dps proteins is not fully described. Incorporation of other metals is also poorly understood.

Previous kinetic and spectroscopic experiments performed in our group have shown the presence of a mononuclear iron-binding site. However, the available crystallographic structures of Dps are ambiguous regarding the number of iron atoms that bind to the FOC. In this sense, this thesis was focused on the iron incorporation mechanism and on the structural characterization of metals, Fe(II) and Cu(II), binding to the FOC.

With X-ray crystallography, high resolution crystal structures up to 1.7 Å of Apo-Dps, 12Fe-Dps and 12Cu-Dps from *P. nautica* were obtained (Table 4.2) and revealed a nearly spherical shell composed by twelve similar monomers and two FOCs located between symmetry-related monomers with different geometries and different metals bound (Figures 4.22, 4.26 and 4.28). These crystals in space group $P22_12_1$ showed a pseudo-hexagonal crystal packing, where Dps molecules form a tightly packed, multi-layered structure (Figure 4.32). This hexagonal packing feature is similar to that observed by electron microscopy for *E. coli* Dps and by X-ray crystallography for *B. brevis* Dps. [46,47] In total, every Dps molecule formed crystal contacts with its twelve neighbors and these crystal contacts facilitated by calcium atoms help to stabilize the crystal packing (Figures 4.33-4.35).

In the crystal structural of 12Fe-Dps, one iron atom, with full occupancy, was bound to each FOC with an octahedral coordination sphere (Figure 4.27). The coordination of the Fe(II) comprised the side-chains of the protein residues Asp65 and Glu69 from one monomer and His38 from the monomer symmetry-related as well as two water molecules. This mononuclear

site was previously observed for other structures of Dps, such as for *M. smegmatis*, *H. pylori* and *A. tumefaciens*, whereas a binuclear site was reported for other Dps protein structures. For Dps from *D. radiodurans* and *B. brevis* a second iron site close to the one referred for *P. nautica* Dps was described to be present with loose coordination. The iron in the second position appeared to be directly coordinated by one protein residue and indirectly by two protein residues *via* two water molecules. [32,34,40,47,101]

Protein residues that coordinate the iron in the FOC are conserved, as showed in the multiple sequence alignment, but usually a tetrahedral geometry of iron coordination is referred for iron binding. [26,32,38,40] For Dps *P. nautica*, the observed FOC is similar to the FOCs of other Dps-like proteins, even though the geometry of iron coordination is octahedral. The similarity observed for the FOCs in all members of the Dps family could explain the similarity of the iron oxidation using H_2O_2 and O_2 as co-substrates, where H_2O_2 is more efficient than O_2. [25] In order to clarify the mechanism of iron incorporation into Dps protein, Phe46 was investigated, since this residue could be involved in this process. Phe46 is structurally close to the FOC and due to its aromatic ring it could be involved in the electron transfer process necessary for the iron oxidation (Figure 4.11).

Crystal structure of 12Fe-Dps showed the ability of this protein to bind iron in the FOC, however its storage as well as the iron oxidation reaction could not be observed with this technique. Therefore, iron uptake assays were performed using H_2O_2 as co-substrate for Dps WT and Dps F46G (Figure 4.12) as well as the kinetic of Fe(II) oxidation with O_2 was followed by UV-Vis spectroscopy (Figure 4.14). These studies demonstrated that not only the Dps WT but also the Dps F46G variant were capable of performing the ferroxidase activity. It was also demonstrated that Phe46 residue did not influence the amount of iron atoms that can be accommodated by each protein variant. About 1000 iron atoms were stored by these proteins when H_2O_2 was used as the oxidant, which is significantly higher when compared to the 500 iron atoms previously described for other Dps proteins. [40,102] This fact could be explained by a chemically different the iron core, due to the variable amount of phosphate that can be incorporated or by a flexibility of the Dps monomers that can form protein shells with different sizes. [24]

On the other hand, when Phe46 was replaced by a glycine, the rate of iron core formation drastically decreased, showing its influence in this process. A first order kinetic model was described for the iron core formation in Dps WT when O_2 was used to follow the Fe(II) oxidation and k' was determined to be 0.015 min^{-1}. Nevertheless, for Dps F46G was not possible to describe the iron core formation. It was only observed that Dps F46G has a different mechanism for the iron core formation in comparison to Dps WT. With these experiments was possible to observe that Phe46 has a role in the iron core formation, but further studies have to be performed to clarify if Phe46 has a structural or a chemical influence in the iron core formation.

The Cu(II) was used in this study in order to investigate if this metal, with paramagnetic properties, could be used as a structural probe for the mechanism of iron binding.

Within the crystal structure of 12Cu-Dps, it was possible to observe a similar binding of Cu(II) compared to the 12Fe-Dps structure. In the mononuclear FOCs was observed the binding of 12 Cu(II) atoms coordinated by the side-chains of the same protein residues that participate in iron binding. However, Cu(II) atoms were most likely tetrahedral coordinated (Figure 4.29).

Dps can utilize copper in a similar way as iron and the metal-binding takes place in the same site. Nevertheless, with this structural characterization of the binding of Cu(II) to the FOC was not possible to observe what happens to the copper atoms after the binding to the FOCs. So far, it is still unknown if Dps proteins are able to incorporate and store these atoms in the central cavity as observed for the iron atoms, but previous work in our group showed the ability of Dps to perform heterometallic cores with divalent metals. [103]

As Cu(II) was already in its oxidized state and Cu(I) atoms might enter the cytoplasm of the cells more easily and they are more toxic, Dps should rather use Cu(I) than Cu(II) for metal incorporation and storage. However, Cu(I) was not used in the X-ray crystallographic experiments due to its low stability. [104,105] Thus, Cu(II) was used and its binding to Dps might mimic the binding of Cu(I) atoms, since they can have same the tetrahedral coordination geometry. [96]

In both crystal structures of 12Fe-Dps and 12Cu-Dps, additional peaks of electron density were observed, besides the ones located in the FOCs. These peaks interpreted as partially occupied iron or copper atoms are located at the junction of three symmetry-related monomers created by the Dps dodecamer. In these positions hydrophilic pores were formed that connect the inner cavity of Dps protein to the exterior. In total Dps has four hydrophilic pores, but only in three of them metals ions were assigned. These pores were previously observed in other Dps structures and as they are mainly negatively charged, they can attract metals ions and an electrostatic gradient can be formed through these pores that can guide the metals toward the FOC located between symmetry-related monomers. Therefore, these hydrophilic pores are potential entry routes for iron and copper atoms. [29,106]

The crystal structure of Apo-Dps protein was also obtained and no iron atoms were found within this structure. However, different geometries were observed for the FOCs when (Figure 4.25) compared to the crystal structures of Dps incubated with iron and copper atoms. These consisted in the presence of a Ca(II) atom bound to one of the FOCs with a coordination number of seven and FOCs without metals bound, where the side-chain of the residue Asp65 can adopt different conformations. In one conformation, Aps65 favors the binding of iron, resembling the geometry of the FOC with metal bound, whereas the other could form a salt bridge with Arg35 from the symmetry-related monomer. A similar observation was described for Dps from *A. tumefaciens*, even though the salt bridge was formed with a lysine residue. [40]

The alternative conformation of Aps65 residue demonstrates some degree of flexibility for the FOC, which was also observed for Dps-like proteins, such as Dpr from *S. suis* and Dps from *A. tumefaciens*. [40,92] This might be important for the binding of the metal to the FOC, since when the Asp65 is forming a salt bridge with Arg35, there is structurally more space for that.

After the metal is placed in the FOC, Asp65 could change its conformation to coordinate the metal, which is electrostatically more favorable.

These studies performed with different metals allow us to conclude that Dps from *P. nautica* is able to bind divalent metals in a similar fashion as iron, which was also observed for the Dpr protein from *S. suis* through X-ray crystallography and Isothermal Titration Calorimetry (ITC). [103] Nevertheless, a higher affinity of the FOC was observed for iron and copper, since even in the presence of a high concentration of calcium atoms in the reservoir solution, only one Ca(II) was bound to the FOC of the Apo-Dps structure.

The ability that Dps can bind different divalent metals can be used for the production of metallic NPs with controlled dimensions and narrow size distribution. This is complementary to previous work performed in our group, where has been shown the capacity of this protein to form heterometallic cores. This metal-binding site could also be used to remove metal ions from the environment and to perform cellular detoxification. [49,53,92]

An additional function observed only for Dps protein family is its ability to bind and protect DNA molecules from oxidative damage. Only some Dps proteins have this DNA binding property and until now no X-ray crystallographic structure of Dps protein with DNA was published. So far, the N-terminal region with positive charged residues has been suggested to be involved in the binding of DNA as well as DNA binding models were proposed, but the DNA binding mechanism is still not completely understood. [31,47]

Previous EMSA experiments performed in our group showed that Dps WT from *P. nautica* has the ability to bind supercoiled plasmid DNA, as can be seen by the shifted band that correspond to the complex Dps-DNA formation (Figure 4.14). As the N-terminus has been suggested for DNA binding, the Dps variant Q14E was used to perform EMSA experiments in order to characterize this binding. The results obtained (Figure 4.15 and Figure 4.16) showed that the binding affinity of DNA significantly decreases for Dps Q14E in comparison to Dps WT, evidencing the influence of the charge of the residues from N-terminus in the DNA binding.

Therefore, in order to further investigate the DNA binding, namely Dps D9K, D11K, D9K/D11K and Q14K, were successfully produced through site-directed mutagenesis (Figure 4.17). As in these mutants the residues from the N-terminus with neutral or negative charges were replaced by positively charged residues, they might be able to increase the affinity of DNA binding, which could be helpful for co-crystallization experiments of Dps with DNA molecules.

As the proposed DNA binding models suggest, DNA molecules could be located in the spaces formed between crystallized Dps molecules. [31,47] Crystals obtained with the reservoir solution 10 % PEG 4000, 20 % glycerol, 0.03 M halogens and 0.1 M MES/Imidazole pH 6.5 showed a better crystal shape (Figure 4.19), but their diffraction was limited to 3 Å. An anisotropic effect was observed in the X-ray diffraction pattern of these crystals (Figure 4.21) in space group P6, which is caused by the crystal packing observed along the axes of the unit cell. In these crystals a multi-layered packed structure is also observed, but in the a and b directions more crystal contacts are performed and crystal packing is more tight than in the c direction, where Dps molecules are superimposed (Figure 4.36). For each Dps dodecamer five neighbors

establishing crystal contacts were identified (Figure 4.37). Thus, co-crystallization trials with DNA could be performed with this crystallization condition Despite these crystals diffracted to lower resolution than crystals in space group $P22_12_1$, the Dps molecules are that not tightly packed, leaving more space where DNA molecules could be accommodated without disturbing the crystal packing. Obtaining an X-ray crystallographic structure of Dps protein with DNA would allow a structural characterization of this interaction and could help to clarify the DNA binding mechanism.

6 Outlook

Dps protein from *P. nautica* was explored in this thesis by studying its functional and structural features, in order to better understand and characterize this family of proteins functionally similar to maxi-ferritins.

Dps family of proteins showed a low sequence identity but a highly similar tridimensional structure, with the exception of the N- and C-terminal regions that are flexible and with variable lengths. The functional advantage of these regions is still not clear, despite its putative relation of the N-terminus in the DNA binding.

High resolution crystal structures were obtained and it was possible to observe the binding of the Fe(II) and Cu(II) atoms with different coordination geometry to the twelve FOCs present between symmetry-related molecules. Both proteins, 12Fe-Dps and 12Cu-Dps, showed a mononuclear metal-binding site coordinated by the same protein residues. Geometrically different FOCs were also observed in the Apo-Dps and the presence of a residue that can adopt double conformation showed some degree of flexibility that might be important to create space for the binding of the metal ions to the FOC.

The binding of different divalent metals is an advantage, since organisms that express this protein are more resistant to higher concentrations of iron as well as other metals and can survive longer during severe stress conditions.

This Dps protein is functionally active and capable of accommodate iron atoms in its inner cavity as well as Dps F46G. However, in contrast to the described for other Dps proteins, these ones showed the ability to storage about 1000 Fe(II)/Dps, which could be explained by chemical composition of the iron core or due to differences in the size of the protein.

So far the iron incorporation mechanism is still not completely understood, but it has been observed the influence of Phe46, structurally located close to the FOC, in this process when O_2 was used as a co-substrate for the iron oxidation. However, with the obtained results was not possible to define which is the exact role of this residue in the iron core formation.

To clarify the iron core formation mechanism as well as the amount of iron atoms that can be stored in the inner cavity, Extended X-ray Absorption Fine Structure (EXAF) could be used. This would allow to study intermediates in the iron core formation and factors that may alter the core structure. Also for this propose and to verify if Phe46 is important for the electron transfer process in the iron oxidation, fast kinetic assays such as Rapid-Freeze Quench (RFQ) and Stopped-Flow (SF) could be performed.

As Cu(II) binding to the FOCs of Dps is similar to the binding of Fe(II), this metal could be used as a structural probe for the ion incorporation mechanism that could be followed by Electron Paramagnetic Resonance (EPR) due the paramagnetic properties of Cu(II).

Potential entry routes for the metal ions into Dps protein were observed at the junction of three symmetry-related monomers, where hydrophilic pores are created connecting the inner cavity to the exterior. Thus, the residues coordinating the metals in these pores are potential targets for site-directed mutagenesis.

Finally, crystals obtained with different crystallization conditions showed a different space group as well as a different crystal packing. As Dps molecules in the crystal with the space group P6 are not so tightly packed, this condition could be used for crystallization trials of Dps with DNA in order to obtain the X-ray crystallographic structure. This would allow a structural characterization of this binding and it would clarify the role of the N-terminus in this interaction. Also to facilitate this co-crystallization process, the produced mutants of Dps could be used in case they increase the affinity for DNA binding, which could be primarily confirmed by EMSAs.

7 References

1. Proulx-curry, P. M. & Chasteen, N. D. Molecular aspects of iron uptake and storage in ferritin. *Coord. Chem. Rev.* **144,** 347–368 (1995).

2. Briat, J.-F. Iron assimilation and storage in prokaryotes. *J. Gen. Microbiol.* **138,** 2475–2483 (1992).

3. Bou-Abdallah, F. The iron redox and hydrolysis chemistry of the ferritins. *Biochim. Biophys. Acta* **1800,** 719–731 (2010).

4. Andrews, S. C., Robinson, A. K. & Rodríguez-Quiñones, F. Bacterial iron homeostasis. *FEMS Microbiol. Rev.* **27,** 215–237 (2003).

5. Chiancone, E., Ceci, P., Ilari, A., Ribacchi, F. & Stefanini, S. Iron and proteins for iron storage and detoxification. *Biometals* **17,** 197–202 (2004).

6. Timóteo, C. G. *et al.* Desulfovibrio vulgaris bacterioferritin uses H(2)O(2) as a co-substrate for iron oxidation and reveals DPS-like DNA protection and binding activities. *Biochem. J.* **446,** 125–133 (2012).

7. Lewin, A., Moore, G. R. & Le Brun, N. E. Formation of protein-coated iron minerals. *Dalton Trans.* 3597–610 (2005).

8. Aisen, P., Enns, C. & Wessling-Resnick, M. Chemistry and biology of eukaryotic iron metabolism. *Int. J. Biochem. Cell Biol.* **33,** 940–959 (2001).

9. Pesek, J., Büchler, R., Albrecht, R., Boland, W. & Zeth, K. Structure and mechanism of iron translocation by a Dps protein from Microbacterium arborescens. *J. Biol. Chem.* **286,** 34872–34882 (2011).

10. Bradley, J. M., Moore, G. R. & Le Brun, N. E. Mechanisms of iron mineralization in ferritins: one size does not fit all. *J. Biol. Inorg. Chem.* **19,** 775–785 (2014).

11. Le Brun, N. E., Crow, A., Murphy, M. E. P., Mauk, A. G. & Moore, G. R. Iron core mineralisation in prokaryotic ferritins. *Biochim. Biophys. Acta* **1800,** 732–744 (2010).

12. Theil, E. C. Ferritin protein nanocages - the story. *Nanotechnol. Perceptions* **8,** 7–16 (2013).

13. Andrews, S. C. The Ferritin-like superfamily: Evolution of the biological iron storeman from a rubrerythrin-like ancestor. *Biochim. Biophys. Acta* **1800,** 691–705 (2010).

14. Zhang, Y. & Orner, B. P. Self-assembly in the ferritin nano-cage protein superfamily. *Int. J. Mol. Sci.* **12,** 5406–5421 (2011).

15. Arosio, P., Ingrassia, R. & Cavadini, P. Ferritins: a family of molecules for iron storage, antioxidation and more. *Biochim. Biophys. Acta* **1790,** 589–599 (2009).

16. Crichton, R. R. & Declercq, J.-P. X-ray structures of ferritins and related proteins. *Biochim. Biophys. Acta* **1800,** 706–718 (2010).

17. Theil, E. C., Behera, R. K. & Tosha, T. Ferritins for Chemistry and for Life. *Coord. Chem. Rev.* **257,** 579–586 (2013).

18. Harrison, P. M., Arosio, P. The ferritins: molecular properties, iron storage function and cellular regulation. *Biochim. Biophys. Acta* **1275,** 161–203 (1996).

19. Uchida, M., Kang, S., Reichhardt, C., Harlen, K. & Douglas, T. The ferritin superfamily: Supramolecular templates for materials synthesis. *Biochim. Biophys. Acta* **1800,** 834–845 (2010).

20. Tosha, T. *et al.* Ferritin protein nanocage ion channels: gating by N-terminal extensions. *J. Biol. Chem.* **287,** 13016–13025 (2012).

21. Rivera, M. Binding of Pseudomonas aeruginosa Apo-Bacterioferritin Associated Ferredoxin to Bacterioferritin B Promotes Heme Mediation of Electron Delivery and Mobilization of Core Mineral Iron. *Biochemistry* **48,** 7420–7431 (2010).

22. Velayudhan, J., Castor, M., Richardson, A., Main-Hester, K. L. & Fang, F. C. The role of ferritins in the physiology of Salmonella enterica sv. Typhimurium: a unique role for ferritin B in iron-sulphur cluster repair and virulence. *Mol. Microbiol.* **63,** 1495–1507 (2007).

23. Calhoun, L. N. & Kwon, Y. M. Structure, function and regulation of the DNA-binding protein Dps and its role in acid and oxidative stress resistance in Escherichia coli: a review. *J. Appl. Microbiol.* **110,** 375–386 (2010).

24. Haikarainen, T. & Papageorgiou, A. C. Dps-like proteins: structural and functional insights into a versatile protein family. *Cell. Mol. Life Sci.* **67,** 341–351 (2010).

25. Chiancone, E. & Ceci, P. The multifaceted capacity of Dps proteins to combat bacterial stress conditions: Detoxification of iron and hydrogen peroxide and DNA binding. *Biochim. Biophys. Acta* **1800,** 798–805 (2010).

26. Papinutto, E. *et al.* Structure of two iron-binding proteins from Bacillus anthracis. *J. Biol. Chem.* **277,** 15093–15098 (2002).

27. Almirón, M., Link, a J., Furlong, D. & Kolter, R. A novel DNA-binding protein with regulatory and protective roles in starved Escherichia coli. *Genes Dev.* **6,** 2646–54 (1992).

28. Nair, S. & Finkel, S. E. Dps Protects Cells against Multiple Stresses during Stationary Phase Dps Protects Cells against Multiple Stresses during Stationary Phase. *J. Bacteriol.* **186,** 4192–4198 (2004).

29. Ilari, a, Stefanini, S., Chiancone, E. & Tsernoglou, D. The dodecameric ferritin from Listeria innocua contains a novel intersubunit iron-binding site. *Nat. Struct. Biol.* **7,** 38–43 (2000).

30. Ali Azam, T., Iwata, a, Nishimura, a, Ueda, S. & Ishihama, a. Growth phase-dependent variation in protein composition of the Escherichia coli nucleoid. *J. Bacteriol.* **181,** 6361–70 (1999).

31. Grant R. A., Filman D. J., Finkel S. E., Kolter R., H. J. M. The crystal structure of Dps, a ferritin homolog that binds and protects DNA. *Nat. Struct. Biol.* **5,** 294–303 (1998).

32. Roy, S. *et al.* X-ray analysis of Mycobacterium smegmatis Dps and a comparative study involving other Dps and Dps-like molecules. *J. Mol. Biol.* **339,** 1103–1113 (2004).

33. Stillman, T. J. *et al.* The crystal structures of Lactococcus lactis MG1363 Dps proteins reveal the presence of an N-terminal helix that is required for DNA binding. **57,** 1101–1112 (2005).

34. Zanotti, G. *et al.* Structure of the Neutrophil-activating Protein from Helicobacter pylori. *J. Mol. Biol.* **323,** 125–130 (2002).

35. Romão, C. V, Mitchell, E. P. & McSweeney, S. The crystal structure of Deinococcus radiodurans Dps protein (DR2263) reveals the presence of a novel metal centre in the N terminus. *J. Biol. Inorg. Chem.* **11,** 891–902 (2006).

36. Zhao, G. *et al.* Iron and hydrogen peroxide detoxification properties of DNA-binding protein from starved cells. A ferritin-like DNA-binding protein of Escherichia coli. *J. Biol. Chem.* **277,** 27689–96 (2002).

37. Ilari, A., Ceci, P., Ferrari, D., Rossi, G. L. & Chiancone, E. Iron incorporation into Escherichia coli Dps gives rise to a ferritin-like microcrystalline core. *J. Biol. Chem.* **277,** 37619–37623 (2002).

38. Kauko, A. *et al.* Iron incorporation in Streptococcus suis Dps-like peroxide resistance protein Dpr requires mobility in the ferroxidase center and leads to the formation of a ferrihydrite-like core. *J. Mol. Biol.* **364,** 97–109 (2006).

39. Lawson, D. M. *et al.* Identification of the ferroxidase centre in ferritin. *FEBS Lett.* **254,** 207–10 (1989).

40. Ceci, P., Ilari, A., Falvo, E. & Chiancone, E. The Dps protein of Agrobacterium tumefaciens does not bind to DNA but protects it toward oxidative cleavage: X-ray crystal structure, iron binding, and hydroxyl-radical scavenging properties. *J. Biol. Chem.* **278,** 20319–20326 (2003).

41. Zhao, G. *et al.* Multiple pathways for mineral core formation in mammalian apoferritin. The role of hydrogen peroxide. *Biochemistry* **42,** 3142–3150 (2003).

42. Su, M. *et al.* The So-Called Listeria innocua Ferritin Is a Dps Protein. Iron Incorporation , Detoxification , and DNA Protection Properties. *Biochemistry* **44,** 5572–5578 (2005).

43. Castruita, M., Elmegreen, L. a, Shaked, Y., Stiefel, E. I. & Morel, F. M. M. Comparison of the kinetics of iron release from a marine (Trichodesmium erythraeum) Dps protein and mammalian ferritin in the presence and absence of ligands. *J. Inorg. Biochem.* **101,** 1686–1691 (2007).

44. Schmid, M. B. More Than Just “Histone-like” Proteins. *Cell Press* **63,** 451–453 (1990).

45. Frenkiel-Krispin, D. *et al.* Regulated phase transitions of bacterial chromatin: a non-enzymatic pathway for generic DNA protection. *EMBO J.* **20,** 1184–1191 (2001).

46. Wolf, S. G. *et al.* DNA protection by biocrystallization. *Nature* **400,** 83–85 (1999).

47. Ren, B., Tibbelin, G., Kajino, T., Asami, O. & Ladenstein, R. The Multi-layered Structure of Dps with a Novel Di-nuclear Ferroxidase Center. *J. Mol. Biol.* **329,** 467–477 (2003).

48. Minsky, A., Shimoni, E. & Frenkiel-Krispin, D. Stress, order and survival. *Nat. Rev. Mol. Cell Biol.* **3,** 50–60 (2002).

49. Allen, B. M., Willits, D., Mosolf, J., Young, M. & Douglas, T. Protein Cage Constrained Synthesis of Ferrimagnetic Iron Oxide Nanoparticles. *Adv. Mater.* **21,** 2000–2003 (2002).

50. Allen, M., Willits, D., Young, M. & Douglas, T. Constrained synthesis of cobalt oxide nanomaterials in the 12-subunit protein cage from Listeria innocua. *Inorg. Chem.* **42,** 6300–6305 (2003).

51. Kim, H.-J., Oh, E., Lee, J., Shim, D.-S. & Lee, K.-H. Synthesis of carbon nanotubes with catalytic iron-containing proteins. *Carbon N. Y.* **49,** 3717–3722 (2011).

52. Kramer, R. M., Sowards, L. a, Pender, M. J., Stone, M. O. & Naik, R. R. Constrained iron catalysts for single-walled carbon nanotube growth. *Langmuir* **21,** 8466–8470 (2005).

53. Yoshimura, H. Protein-assisted nanoparticle synthesis. *Colloids Surfaces A Physicochem. Eng. Asp.* **282-283,** 464–470 (2006).

54. Ceci, P. *et al.* Synthesis of iron oxide nanoparticles in Listeria innocua Dps (DNA-binding protein from starved cells): a study with the wild-type protein and a catalytic centre mutant. *Chem. A Eur. J.* **16,** 709–717 (2010).

55. Guilherme, M. Estudos Mecanísticos e Estruturais da Oxidação e Armazenamento de Ferro por Ferritinas Rápidas. (2009).

56. Novagen. pET-21a-d(+) Vectors. (2003).

57. NZYTech. *Low Molecular Weight (LMW) Protein Marker*. (2012).

58. NZYTech. *NZYDNA Ladder II*. (2012).

59. NZYTech. *NZYDNA Ladder III*. (2012).

60. Laemmli, U. L. Cleavage of Structural Proteins during the Assembly of the Head of Bacteriophase T4. *Nature* **227,** 680–685 (1970).

61. Iron by 1,10-phenanthroline assay. *Adv. Chem. Sci.*

62. Rajbhandari, A., Aryal, A. & Rajbhandari, S. Das. Determination of Iron in Iron Tablets by Spectrophotometry and Atomic Absorption Spectroscopy. *Int. J. Pharm. Biol. Arch.* **4,** 435–438 (2013).

63. Maloney, K. M., Quiazon, E. M. & Indralingam, R. Measurement of Iron in Egg Yolk: An Instrumental Analysis Experiment Using Biochemical Principles. *J. Chem. Educ.* **85,** 399–400 (2008).

64. Hellman, L. M. & Fried, M. G. Electrophoretic mobility shift sssay (EMSA) for detecting protein-nucleic acids interactions. *Nat. Protoc.* **2,** 1849–1861 (2009).

65. Molloy, P. L. Electrophoretic mobility shift assays. *Methods Mol. Biol.* **130,** 235–246 (2000).

66. Abràmoff, M. D., Magalhães, P. J. & Ram, S. J. Image Processing with ImageJ. *Biophotonics Int.* **11,** 36–42 (2004).

67. Carter, P. Site-directed mutagenesis. *Biochem. J.* **237,** 1–7 (1986).

68. NZYTech. *NZYMutagenesis kit*. (2013).

69. http://www.ncbi.nlm.nih.gov/projects/genome/probe/doc/TechPCR.shtml (19.07.2014).

70. Pusey, M. L. *et al.* Life in the fast lane for protein crystallization and X-ray crystallography. *Prog. Biophys. Mol. Biol.* **88,** 359–386 (2005).

71. Murray, J. W., Garman, E. F. & Ravelli, R. B. G. X-ray absorption by macromolecular crystals: the effects of wavelength and crystal composition on absorbed dose. *J. Appl. Crystallogr.* **37,** 513–522 (2004).

72. Gale, R. *Crystallography Made Crystal Clear*. 49–133 (Academic Press, 2006).

73. Holbrook, E. L. & Berkeley, L. Crystallisation of Nucleic Acids. *Encycl. Life Sci.* 1–6 (2010).

74. Asherie, N. Protein crystallization and phase diagrams. *Methods* **34,** 266–272 (2004).

75. Carvalho, A. L., Trincão, J., Romão, M. J. in *Ligand-Macromolecular Interact. Drug Discov. Methods Protoc.* (Roque, A. C. A.) **572,** (Humana Press, 2010).

76. Wlodawer, A., Minor, W., Dauter, Z., Jaskolski, M. Protein crystallography for non - crystallographers, or how to get the best (but not more) from published macromolecular structures. *FEBS J.* **275(1),** 1–21 (2008).

77. Taylor, G. L. Introduction to phasing. *Acta Crystallogr. D. Biol. Crystallogr.* **66,** 325–338 (2010).

78. Blasie, J. K. RESONANCE X-RAY SCATTERING : Its use in determining spatial relationships among metal atoms within macromolecules in a non-crystalline state. *Annu. Rev. Biophys. Bioeng.* **10,** 451–458 (1981).

79. Hendrickson, W. A. Determination of macromolecular structures from anomalous diffraction of synchrotron radiation. *Science* **254,** 51–58 (1991).

80. Einsle, O., Andrade, S. L. A., Dobbek, H., Meyer, J. & Douglas, C. Assignment of Individual Metal Redox States in a Metalloprotein by Crystallographic Refinement at Multiple X-ray Wavelengths. *J. Am. Chem. Soc.* **129,** 2210–2211 (2008).

81. Helliwell, M. Anomalous scattering for small-molecule crystallography. *J. Synchrotron Radiat.* **7,** 139–147 (2000).

82. http://skuld.bmsc.washington.edu/cgi-bin/edgeplots (18.06.2014).

83. Kabsch, W. XDS. *Acta Crystallogr. D. Biol. Crystallogr.* **66,** 125–132 (2010).

84. Winn, M. D. *et al.* Overview of the CCP4 suite and current developments. *Acta Crystallogr. D. Biol. Crystallogr.* **67,** 235–242 (2011).

85. Evans, P. R. & Murshudov, G. N. How good are my data and what is the resolution? *Acta Crystallogr. D. Biol. Crystallogr.* **69,** 1204–1214 (2013).

86. Adams, P. D. *et al.* PHENIX: a comprehensive Python-based system for macromolecular structure solution. *Acta Crystallogr. D. Biol. Crystallogr.* **66,** 213–221 (2010).

87. Emsley, P., Lohkamp, B., Scott, W. G. & Cowtan, K. Features and development of Coot. *Acta Crystallogr. D. Biol. Crystallogr.* **66,** 486–501 (2010).

88. Chen, V. B. *et al.* MolProbity: all-atom structure validation for macromolecular crystallography. *Acta Crystallogr. D. Biol. Crystallogr.* **66,** 12–21 (2010).

89. The PyMOL Molecular Graphics System 1.5.0.4 Schrödinger, LLC.

90. Desbois, S., Seabrook, S. a & Newman, J. Some practical guidelines for UV imaging in the protein crystallization laboratory. *Acta Crystallogr. Sect. F. Struct. Biol. Cryst. Commun.* **69,** 201–208 (2013).

91. Kantardjieff, K. A. Matthews coefficient probabilities : Improved estimates for unit cell contents of proteins , DNA , and protein – nucleic acid complex crystals. *Protein Sci.* **12,** 1865–1871 (2003).

92. Kauko, A., Haataja, S., Pulliainen, A. T., Finne, J. & Papageorgiou, A. C. Crystal structure of Streptococcus suis Dps-like peroxide resistance protein Dpr: implications for iron incorporation. *J. Mol. Biol.* **338,** 547–558 (2004).

93. Geneious version 4.8 created by Biomatters.

94. Reva, B. a, Finkelstein, a V & Skolnick, J. What is the probability of a chance prediction of a protein structure with an rmsd of 6 A? *Fold. Des.* **3,** 141–147 (1998).

95. Katz, A. K., Glusker, J. P., Beebe, S. a. & Bock, C. W. Calcium Ion Coordination: A Comparison with That of Beryllium, Magnesium, and Zinc. *J. Am. Chem. Soc.* **118,** 5752–5763 (1996).

96. Holm, R. H., Kennepohl, P. & Solomon, E. I. Structural and Functional Aspects of Metal Sites in Biology. *Chem. Rev.* **96,** 2239–2314 (1996).

97. Harding, M. M. Geometry of metal-ligand interactions in proteins. *Acta Crystallogr.* **D57,** 401–411 (2001).

98. Rulísek, L., Vondrásek, J. Coordination geometries of selected transition metal ions (Co2+, Ni2+, Cu2+, Zn2+, Cd2+, and Hg2+) in metalloproteins. *J. Inorg. Biochem.* **71,** 115–127 (1998).

99. Ceci, P. *et al.* DNA condensation and self-aggregation of Escherichia coli Dps are coupled phenomena related to the properties of the N-terminus. *Nucleic Acids Res.* **32,** 5935–5944 (2004).

100. Roy, S. *et al.* Role of N and C-terminal tails in DNA binding and assembly in Dps: structural studies of Mycobacterium smegmatis Dps deletion mutants. *J. Mol. Biol.* **370,** 752–767 (2007).

101. Cuypers, M. G., Mitchell, E. P., Romão, C. V & McSweeney, S. M. The crystal structure of the Dps2 from Deinococcus radiodurans reveals an unusual pore profile with a non-specific metal binding site. *J. Mol. Biol.* **371,** 787–799 (2007).

102. Zeth, K. Dps biomineralizing proteins: multifunctional architects of nature. *Biochem. J.* **445,** 297–311 (2012).

103. Haikarainen, T. *et al.* Structural and thermodynamic characterization of metal ion binding in Streptococcus suis Dpr. *J. Mol. Biol.* **405,** 448–460 (2011).

104. Rigo, A. *et al.* Interaction of copper with cysteine: stability of cuprous complexes and catalytic role of cupric ions in anaerobic thiol oxidation. *J. Inorg. Biochem.* **98,** 1495–1501 (2004).

105. Thieme, D. & Grass, G. The Dps protein of Escherichia coli is involved in copper homeostasis. *Microbiol. Res.* **165,** 108–115 (2010).

106. Pulliainen, A. T., Kauko, A., Haataja, S., Papageorgiou, A. C. & Finne, J. Dps/Dpr ferritin-like protein: insights into the mechanism of iron incorporation and evidence for a central role in cellular iron homeostasis in Streptococcus suis. *Mol. Microbiol.* **57,** 1086–1100 (2005).

8 Appendices

8.1 General instrumentation

Sterilization

Sterilization of culture media and current laboratory materials was performed in an autoclave using cycles of 20 in at 121ºC (Labo Autoclave, Sanyo).

Buffer filtration

Filtration of buffers was carried out with a 0.45 µM pore filter (Celulose Acetate, GVS) and a 47 mm magnetic filter funnel (Pall). A vaccum gas pump (VWR) was also used for buffers filtration.

Camera and Transilluminators

Gels were photographed with a Gel Logic 100 Imaging System (Kodak).

Centrifugation

Low-speed centrifugations were carried out with a microcentrifuge (Sigma 1-14, Sartorius).

Dialysis

Dialyses were performed in 12-14 kDa MWCO dialyses membranes (Medicell International Ltd).

Incubation

Incubations at 37 °C were performed in an incubator (BINDER).

Heat-shock

Heat-shock was performed in a heating block (Grant).

pH measurement

The pH was measured using two pH meters (WTW series, inolab or pH Meter Basic 20, Crison).

Protein concentration

Protein concentration was done using a Vivacell 70 with 30 000 MWCO (Sartorius).

Simultaneous stirring and incubation

For all incubation steps during protein expression a digital orbital shaker was used (Ovan, Alfagene).

UV-Vis spectroscopy

UV-visible measurements were performed in an UV-Vis Evolution 300 spectrophotometer (Thermo Scientific).

Weighting

Two digital scales were used for weighting (Acculab Vicon, Sartorius or CP224 S, Sartorius).

8.2 SDS-PAGE

Table 8.1 - Composition used for a 12.5 % acrylamide SGS-PAGE.

Solution	Stacking gel (5 % of acrylamide)	Running gel (12.5 % of acrylamide)
Solution I	-	0.75 mL
Solution II	0.45 mL	-
Solution III	0.3 mL	2.08 mL
10 % (w/v) SDS	0.018 mL	0.05 mL
dH_2O	0.94 mL	2.1 mL
10 % (w/v) APS	13.5 µL	38 µL
TEMED	2 µL	2.5 µL

Table 8.2 - Stock solutions used for SDS-PAGE.[1]

Solution	Reagents	Amount	Observations
Running gel buffer (Solution I)	2.5 M Tris Base HCl concentrated H_2O	30.3 g until pH 8.8 up to 100 mL	pH 8.8-9.0 Dilute 1:2 prior to use
Stacking gel buffer (Solution II)	0.5 M Tris Base HCl concentrated H_2O	6.06 g until pH 6.8 up to 100 mL	pH 6.6-6.8
Acrylamide/Bisacrylamide (37.5:1) (Solution III)	Acrylamide Bisacrylamide H_2O	-	Already prepared
10 % (w/v) SDS	SDS H_2O	10 g up to 100 mL	-
10 % APS	Ammonium persulfate H_2O	0.02 g 200 µL	Prepare prior to use
Tris-Glycine buffer	0.25 M Tris Base 1.92 M Glycine 0.1 % SDS H_2O	30.3 g 144.1 g 10 g up to 1000 mL	pH 8.3 Dilute 1:10 prior to use
Sample buffer	Solution II 10 % (w/v) SDS β-mercaptoethanol Glycerol Bromophenol blue H_2O	5 mL 8 mL 1 mL 2 mL 4 mg up to 20 mL	Add 1:1 to the sample
Coomassie Brilliant Blue R-250 Staining	Coomassie Blue R-250 Glacial acetic acid Methanol H_2O	1 g 15 mL 90 mL up to 200 mL	-
Bleach solution	Glacial acetic acid Methanol H_2O	75 mL 450 mL up to 1000 mL	-

8.3 Oligonucleotide primers data sheets

The oligonucleotide primers used to make the Dps variants D9K, D11K, Q14K and D9K/D11K were designed according with the specifications indicated in the protocol from the NZYMutagenesis kit. The company STABvida performed the synthesis and the purification of the primers and the oligonucleotide data sheets are presented below (Figures 1,2, 3 and 4).

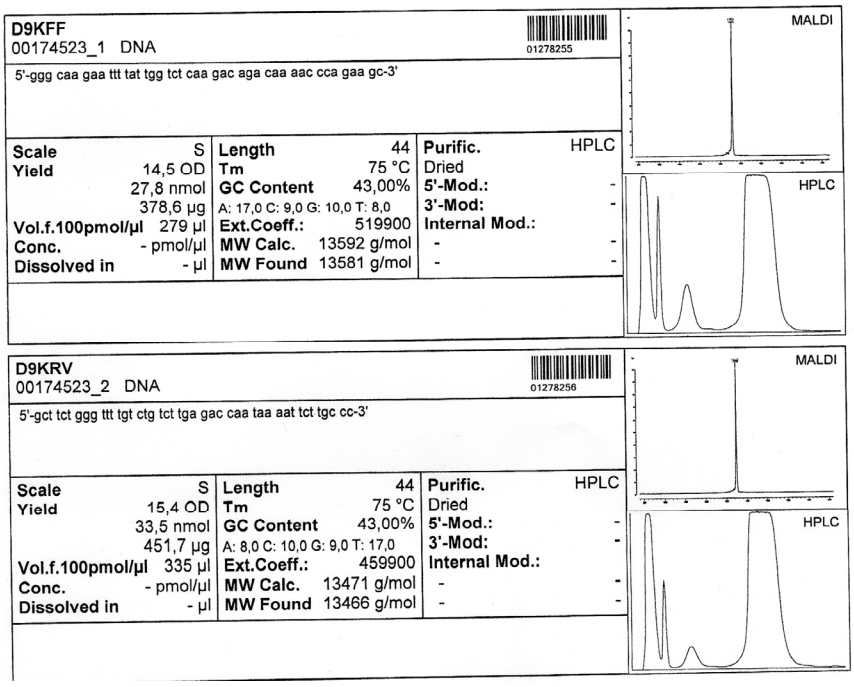

Figure 8.1 - Data sheet provided by STABvida of the primers containing the point mutation to produce the Dps D9K.

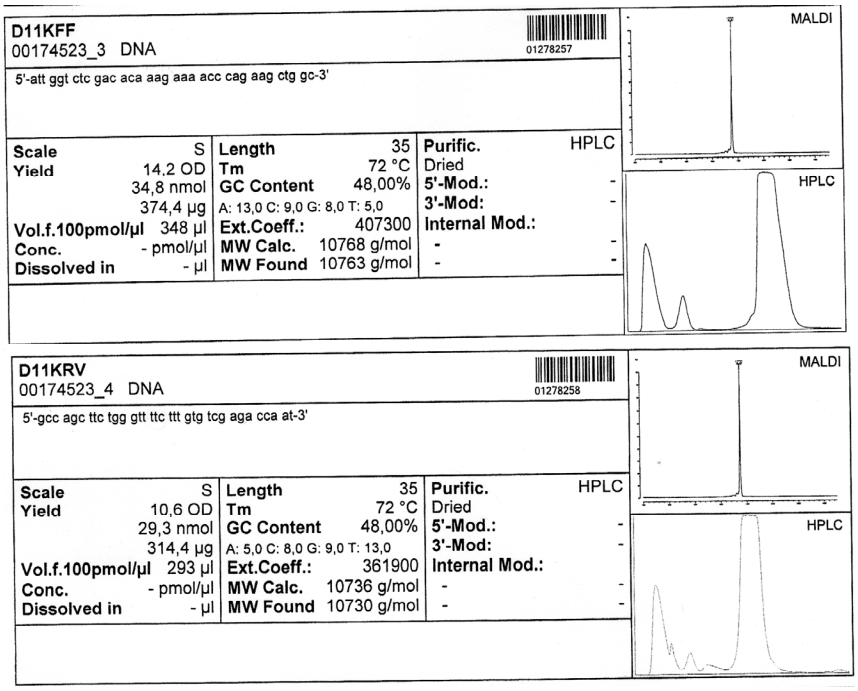

Figure 8.2 - Data sheet provided by STABvida of the primers containing the point mutation to produce the Dps D11K.

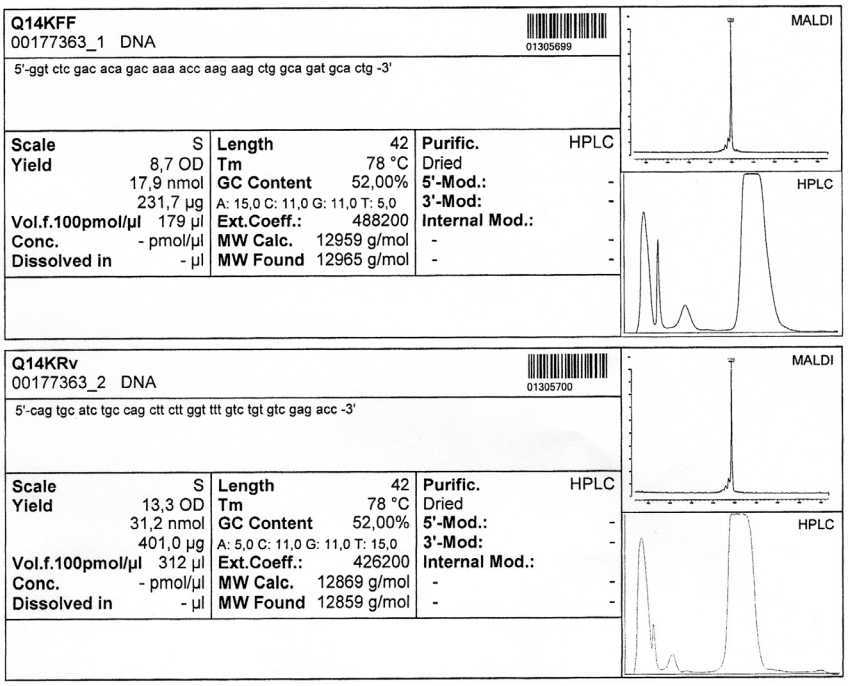

Figure 8.3 - Data sheet provided by STABvida of the primers containing the point mutation to produce the Dps Q14K.

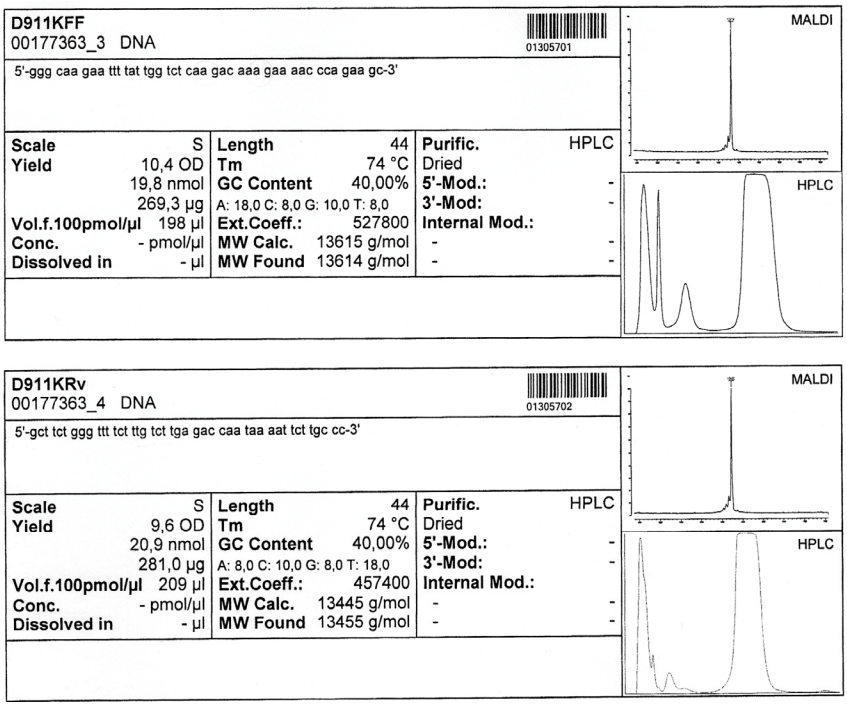

Figure 8.4 - Data sheet provided by STABvida of the primers containing the point mutation to produce the Dps D9K/D11K.

8.4 Crystal systems

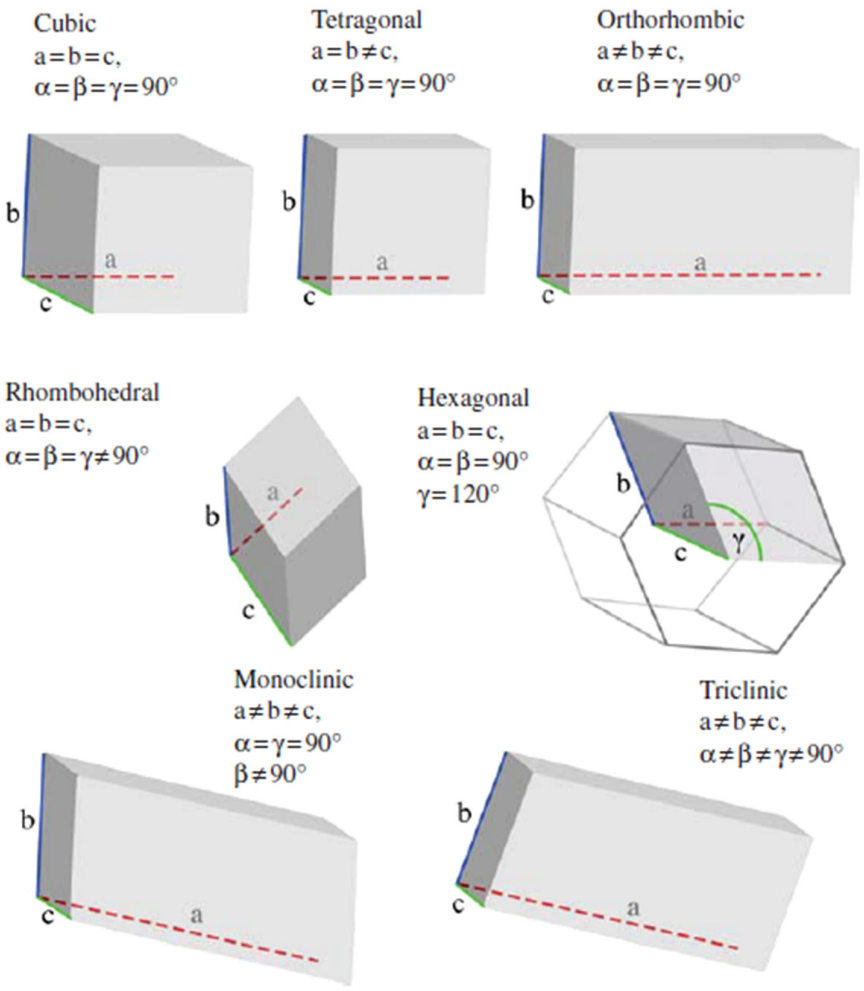

Figure 8.5 - Schematic representation of the seven crystal systems.[2]

8.5 References

1. Laemmli, U. L. Cleavage of Structural Proteins during the Assembly of the Head of Bacteriophase T4. *Nature* **227,** 680–685 (1970).

2. Gale, R. *Crystallography Made Crystal Clear*. 49–133 (Academic Press, 2006).